

# Computer Models to Simulate Ion Flow in Neurons



The University of  
**Nottingham**

Robert Christopher Clay, MSci

Thesis submitted to the University of Nottingham  
for the degree of Doctor of Philosophy

September 2016

## Abstract

In this thesis the Drift Diffusion enhanced Hodgkin Huxley model is developed. This model uses the Drift Diffusion equations to model the bulk solutions both within a neuron and in the surrounding extracellular media. The Hodgkin Huxley ion channel behaviour is incorporated into the membrane regions through the use of an altered diffusion coefficient.

Firstly the model is applied to the case of intracellular and extracellular media separated by a single membrane.

Secondly the model is applied to a cell within a restricted extracellular space. This takes a slice through a cell and is therefore termed a double membrane model, since there are two membrane layers.

Finally the model is used to determine whether there is any charge and field buildup on a gold surface located 100nm from the cell. The results from this could then be used in future to model Surface Plasmon Resonance experiments which may form the basis of novel neuronal activity detectors.

## Acknowledgements

Firstly I would like to thank Mark Fromhold, my supervisor, who has been very supportive and encouraging throughout the duration of my PhD. I would also like to thank Noah Russell for his help and guidance, particularly in matters relating to the biological aspects of the work.

It was a pleasure to have the company of all the people in C19 over the years who have provided support and friendship throughout my time at Nottingham.

I was also privileged to meet and work with many people in Noah's interdisciplinary NPL group.

Many thanks must also go to my family and friends, without whom none of this would have been possible.

# Contents

<b>1</b>	<b>Introduction</b>	<b>1</b>
1.1	Neurons and networks . . . . .	1
1.2	Current detection methods . . . . .	4
1.2.1	Electrical Methods . . . . .	5
1.2.2	Optical Methods . . . . .	7
1.3	The Need for Models . . . . .	10
1.4	Surface Plasmon Resonance . . . . .	10
1.4.1	Optical response and the Drude model . . . . .	10
1.5	Outline . . . . .	11
1.6	Possible Extensions . . . . .	13
<b>2</b>	<b>Background</b>	<b>15</b>
2.1	Neurons and Networks . . . . .	15
2.2	The Hodgkin Huxley Model . . . . .	15
2.2.1	Voltage Clamp Experiments . . . . .	16
2.2.2	The Model . . . . .	17
2.3	Results and features of the Hodgkin Huxley model . . . . .	20
2.4	Simple Neuron Models . . . . .	27
<b>3</b>	<b>Methods</b>	<b>31</b>
3.1	The Drift-Diffusion and Poisson Equations . . . . .	31
3.2	The Membrane . . . . .	34
3.3	Smoothing with tanh Functions . . . . .	35
3.4	Discretisation Schemes and the Non Uniform Grid . . . . .	37
3.4.1	Numerical Errors and computational performance . . . . .	41
3.5	The Newton Raphson Method . . . . .	42
3.6	Validation . . . . .	45

---

<b>4</b>	<b>Single Membrane</b>	<b>46</b>
4.1	Outline of the Single Membrane Model . . . . .	46
4.2	Single Membrane Results . . . . .	49
4.3	Validation of Single Membrane Results . . . . .	70
4.4	Single Membrane Conclusions . . . . .	73
<b>5</b>	<b>Double Membrane</b>	<b>74</b>
5.1	Outline . . . . .	74
5.2	Results . . . . .	79
<b>6</b>	<b>Detectors</b>	<b>90</b>
6.1	Gold . . . . .	90
6.2	Results . . . . .	93
<b>7</b>	<b>Conclusions</b>	<b>105</b>
7.1	Suggestions for further work . . . . .	108
	<b>References</b>	<b>118</b>

# Chapter 1

## Introduction

### 1.1 Neurons and networks

Neurons are the signalling cells which make up the nervous system [1; 2]. The cell consists of three main structural features, which we now describe and can be seen in Figure 1.1 .

The first is a dendritic tree. This consists of a set of dendrites which are filament like structures that extend from the main cell body (soma). The purpose of the dendrites is to allow the electrochemical signals from other neurons to propagate to the main cell body.

This cell body is the second key feature and is often referred to as the soma. The nucleus and many other important organelles are contained within the soma. The neurotransmitters are produced in the soma. Connecting the soma to the axon is the axon hillock. It is this region which integrates the various inputs to the neuron and triggers an action potential if the combined stimulus is sufficient.

The axon is the third key structural feature. This is a long fibre down which the nerve impulses can travel to the synaptic sites of other neurons, or, in the case of motor neurons, muscles.

When given a sufficient stimulus, typically an increase in membrane potential of 10-15 mV, an electronic signal is generated in the cell membrane. The signal is a rapid change in the membrane potential from its negative resting value to a positive peak. The signal arises because voltage sensitive ion channels through the membrane open allowing different ion species to cross the membrane and thereby changing the potential difference across it. After the impulse has passed the membrane potential returns to rest. This

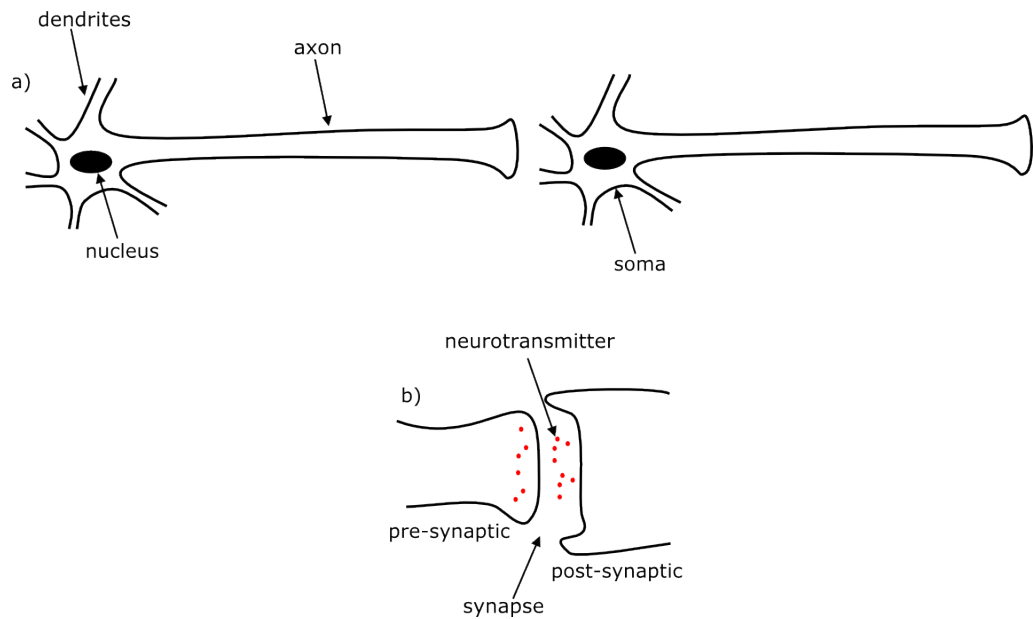


Figure 1.1: a) A simplified diagram showing a pair of neurons after the release of neurotransmitter chemicals, (red dots in figure). Key indicated features are the soma, which is the main cell body and includes the nucleus. The genetic material for the cell is located within the nucleus. Dendrites, which branch off the soma and allow electrochemical signals to be received from other neurons. The axon is a long protuberance which carries signals to other neurons. b) At the end of the axon is a synapse, which consists of a presynaptic ending, a synaptic cleft and a postsynaptic ending. When an impulse reaches the presynaptic ending, neurotransmitters are released into the synaptic cleft. These then diffuse to the postsynaptic ending and can trigger further impulses.

signal propagates along the axon until it reaches a synapse. At this point neurotransmitters are released into the synaptic cleft. These are chemicals which are capable of triggering a signal in neighbouring neurons [3].

Figure 1.1 shows a simple diagram of two neurons. The key structural features are highlighted by arrows in the figure. The red dots indicate neurotransmitter chemicals released from the presynaptic terminal. The use of neurotransmitters and synapses enables neurons to interact with one another and so form large complex structures known as networks.

Some neurons also have a myelin sheath which is a fatty substance surrounding the axon. There are gaps in this sheath known as Nodes of Ranvier. It is at these nodes where the ion channels are located. A nerve impulse jumps from node to node in a myelinated fibre.

The unmyelinated fibres have ion channels down the whole length of the axon and so the impulse travels as a wave. Only unmyelinated fibres will be considered in this work.

It is easy to determine the physical structure of a neural network using scanning electron microscopy. A more difficult problem is identifying the functional structure of the networks. This involves determining the causal relationships between neurons, or groups of neurons within the network. This is one of the key outstanding challenges in neuroscience as it enables some understanding of how behaviours develop.

To investigate the functional connections between neurons, it is necessary to be able to reliably detect neural activity, specifically which neurons are firing and when. Without good spatial and temporal resolution it becomes difficult or impossible to figure out the causal links between neurons and the order in which they have a tendency to fire. Understanding these connections between neurons will enable a better understanding of how collective behaviour and neural signalling arises in living organisms.

When looking to detect cell activity it is best to try to monitor the behaviour of the main cell body, rather than the axons. This is because the axons spread out and can form quite a complex structure, so it is not always easy to distinguish to which cell a given axon belongs [4]. The cell bodies are quite easily located using a camera and microscope so positioning potential detectors is made somewhat simpler. Building a detector system that can reliably detect firing events, specifically which neurons fire and when would help to identify the causal relationships between neurons, or

groups of neurons. This would then provide a much deeper insight into the functional (as opposed to the physical) structure of the network.

Various models have been made to describe aspects of neuronal behaviour and enable simulations to be carried out [5; 6; 7]. These vary from models of single neurons, to more complex neural networks consisting of large numbers of cells. The detail used depends on the situation being simulated. In a large network simulation, often a simpler model of the individual neurons will be used as more detailed models are computationally more demanding [8]. These models can be used to understand patterns, learning and plasticity. By using and adapting the Hodgkin Huxley model it is possible to consider better ways of detecting the action potentials. Using drift diffusion equations alongside the Hodgkin Huxley model allows the ion concentration changes and electric field profiles to be simulated. Since it is likely that either the electric or related magnetic fields might be detectable, having a way of accurately calculating these fields allows for a detector's feasibility to be tested.

Models of neurons can then be used in simulations to ascertain whether a proposed detector system is potentially viable. It might be prohibitively expensive or time consuming to build and run the physical experiment, so some idea of feasibility is useful.

## 1.2 Current detection methods

Current methods of detecting action potentials can be broadly divided into two categories, electrical and optical. Within these two categories there are numerous methods or technologies which have been developed and used to varying extents.

When considering the effectiveness of detection schemes, it is important to consider both the resolution and the spatial extent which can be achieved. Some methods provide a very detailed view of the activity, but for only a small portion of a network (or even just a single neuron), such as patch clamping. At the other end of the scale, electroencephalograms provide a broad picture of brain activity indicating active areas of the brain, but provide no detail as to which individual neurons are firing. This would be considered a large spatial extent, low spatial resolution technique.

The same considerations apply on a temporal basis too.

### 1.2.1 Electrical Methods

Electrical methods for detecting neuronal activity can be further divided into intracellular and extracellular methods.

It is not possible to use a simple device such as an Ohmmeter on the neurons because the conductance of the membrane is a function of the voltage across the cell membrane. As a result of this, more sophisticated techniques such as patch clamping were developed.

Intracellular methods are, by their nature, invasive and involve probing the cell with electrodes. An example of an intracellular electrical recording technique is patch clamping.

Patch clamping is an older technique originally applied to detect ion channel currents in frog skeletal muscle [9], but later adapted to probe the behaviour of neurons [10].

To perform a patch clamp experiment a metal electrode is inserted into a cell as shown in 1.2. A second reference electrode is used as a ground. The signal is then sent to an amplifier and analysed.

Using this technique it is possible to record the resting potential of a cell and also stimulate it to study the response. This is done by injecting current using the electrode. Unfortunately, patch clamping damages and eventually kills the cell, so experiments lasting longer than a few hours cannot be carried out. This means that patch clamping as a technique has a high temporal resolution, but relatively low temporal extent.

Since only individual neurons can be monitored in this way, patch clamping also has a limited spatial extent.

A schematic diagram showing the setup for a patch clamp experiment is shown in Figure 1.2.

There are also electrical methods which work on an extracellular level. A widely used example being multi electrode arrays (MEAs). Multi electrode arrays are devices with many electrode contacts which can be used as either stimulating or recording electrodes [11; 12]. This gives them an advantage over patch clamping in that multiple cells can be analysed over a larger area of the network. The ability to stimulate in different ways allows the responses of the network to be examined more clearly using different stimulation patterns.

Unfortunately, due to the way in which neural networks develop, it is quite likely that the axons of multiple neurons will connect to an individual

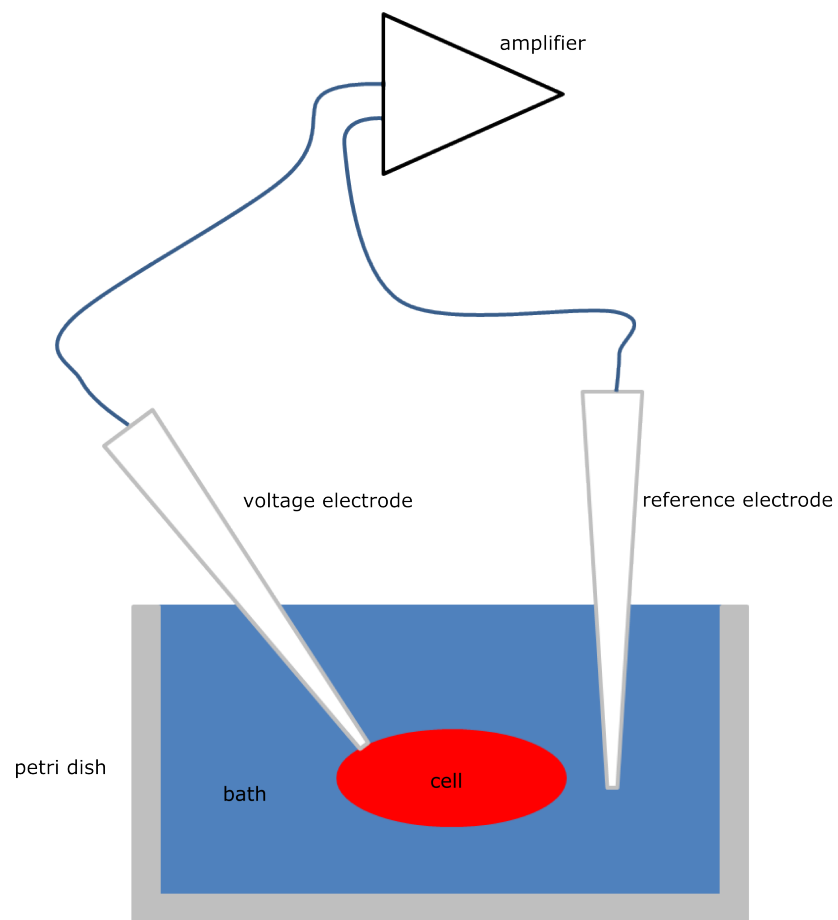


Figure 1.2: Schematic diagram showing the setup for a patch clamp experiment. A voltage measuring electrode is inserted into the cell. A reference electrode is used as a ground and the signals are amplified. The bath contains suitable nutrient rich media.

electrode site. This limits to some degree the spatial resolution of the MEAs as it becomes impossible to distinguish precisely which cell is firing (or when stimulating, it will only be possible to stimulate several neurons in contact with the electrode rather than, ideally, a single neuron) [4].

It is for this reason that a detector which can monitor the cell bodies (easily identifiable using a camera), and give a precise indication of which cell fires when, is desirable. This means that any proposed detection system needs to have a good spatial resolution and a large spatial extent, so that it can monitor a large area of the network and provide accurate information regarding individual cell firing events.

### 1.2.2 Optical Methods

It is also possible to use optical methods to monitor the activity within neural networks. These methods have the advantage that they do not suffer from electrical artefacts as is the case with electronic methods. Optical methods are divided into two categories, intrinsic and extrinsic.

Intrinsic methods detect neural activity through detection of changes to the system's intrinsic optical properties. These could be refractive index changes, scattering or absorption effects. It is known that during an action potential there is a small percentage change in the refractive index of the cell. This change affects the scattering of light in a measurable way [13].

Extrinsic methods involve the external application of voltage sensitive dyes. These dyes are capable of providing detailed information about activity within a neural network. They are capable of achieving 20-50  $\mu\text{m}$  spatial resolution and millisecond temporal resolution [14].

When applied to a neural population, the dyes bind to sites within the cell membranes in such a manner as to not interfere with their function. The dyes are then excited using light, at which point they fluoresce. How much fluorescence occurs is dependent on the behaviour of the membrane. This therefore enables accurate high temporal resolution monitoring of neural activity.

Unfortunately, the voltage sensitive dyes are affected by photo bleaching and are also toxic, so the experiments can only run for a few hours. This is a much too limited temporal extent.

It is widely reported that calcium plays a key role in neuronal activity. It is therefore possible to monitor the levels of calcium and use this information

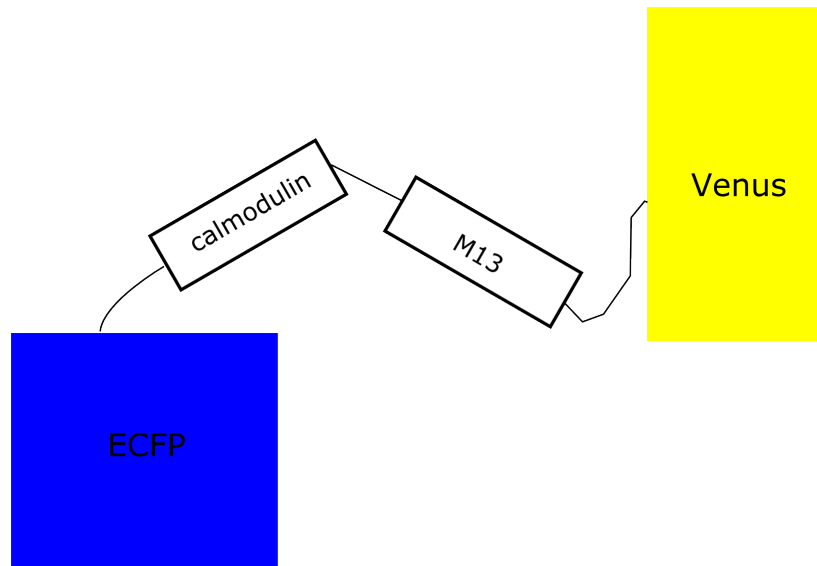


Figure 1.3: Schematic diagram showing an example of a genetically encoded calcium indicator of the Förster resonance energy transfer type. Two fluorescent proteins, ECFP and Venus, are connected by calmodulin and M13 linkages. When calcium binds to the calmodulin, the distance between the fluorescent proteins decreases causing the blue emission from the ECFP to decrease and the yellow emission from Venus to increase.

to detect activity. This can be achieved by using dyes, or by genetically encoding calcium indicators (GECI) [15].

There are two basic types of GECI, Förster resonance energy transfer (FRET) types or single fluorophore types. An example of the FRET type is Yellow Cameleon 3.60 (YC 3.60) [16].

The structure of YC 3.60 consists of two fluorescent proteins joined by a linker sequence. The two proteins are the enhanced cyan fluorescent protein (ECFP) and a circularly permuted Venus protein. These two fluorescent proteins are linked by calmodulin, which is a calcium binding protein and M13, which is a calmodulin binding peptide [15; 16]. This structure is shown schematically in figure 1.3

FRET imaging involves a nonradiative energy transfer from a donor fluorophore in an excited state, to an acceptor [17]. The acceptor does not necessarily have to be fluorescent, although in the case of YC 3.60 it is.

Prior to calcium binding, ECFP dominates the fluorescence with its emissions in the blue (480 nm) part of the spectrum. In the presence of calcium ions, binding occurs which leads to a reduction in the distance be-

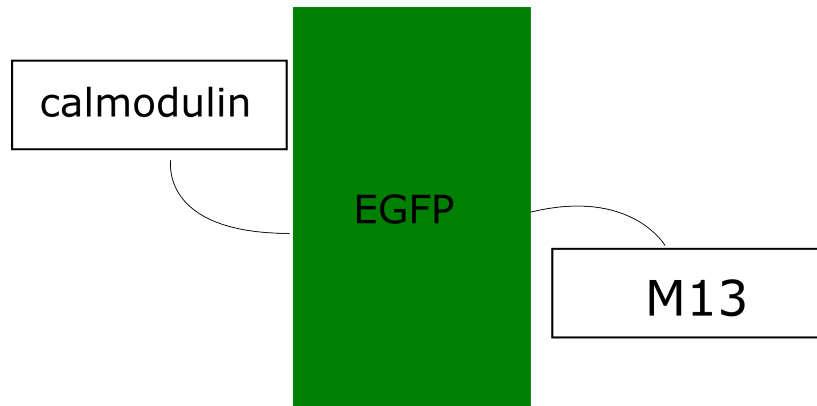


Figure 1.4: Schematic showing an example of a genetically encoded calcium indicator of the single fluorophore type. This whole structure is called GCaMP which consists of a single circularly permuted enhanced green fluorescent protein (EGFP) attached to calmodulin and M13.

tween the two fluorescent proteins. This leads to the Venus protein entering an excited state and emitting in the yellow part (530 nm) of the spectrum. This then makes it possible to detect the levels of calcium by monitoring the ratio between blue and yellow emission [15; 16].

The GCaMP family of proteins are good representatives of the single fluorophore GECIs [15; 18]. These have a very different structure to the FRET GECIs discussed earlier.

GCaMPs consist of a single circularly permuted enhanced green fluorescent protein (EGFP). This is attached to calmodulin on one side and M13 on the other [19].

In the case of GCaMPs, it is the interactions between calmodulin and M13 in the presence of calcium that causes a change in the fluorescence of the fluorophore EGFP.

Both types of GECI provide a long lasting way of monitoring neural activity as they are less prone to damaging or killing the cells. This gives them a good temporal extent.

There are many ways of introducing the GECIs into the cell lines, but the most commonly used methods are viral transduction methods, particularly involving the use of Lentivirus (LV) as a vector [20].

Other viral vectors can be used and this affects the size of the genome which can be introduced into the cells.

Because both electric and optical methods have a range of drawbacks, it

is desirable to develop a new detection system which has good spatial and temporal resolution. Good spatial and temporal extent are also required to allow activity across the network to be monitored for a long time.

### 1.3 The Need for Models

A system is needed which can detect neural activity without invasive penetration of cells or potentially toxic chemicals. To do this it is necessary to develop a model that is able to keep track of the concentration changes that occur inside and outside the cell, particularly when considering a restricted extracellular space. This enables the electric potential and fields to be calculated, which is useful as these parameters are often measurable by different detector technologies, such as BEC microscopes discussed in 1.6 or diamond N-V centres discussed in Chapter 7. [21; 22]. It is the development of these models which is the main focus of this thesis.

### 1.4 Surface Plasmon Resonance

One possible detection system utilises surface plasmon resonance (SPR) techniques. SPR has found a variety of uses within the biosciences, often being used to detect biomolecules binding to surfaces and determining various binding rates. More recently the technology has been used to image cells [23] and detect neural activity [24]. One of the more common experimental setups is known as the Kretschmann attenuated total internal reflection configuration [25]. This offers a good large field of view (high spatial extent) but its resolution is limited due to the use of a prism which limits the numerical aperture and magnification.

Surface plasmons are collective electron oscillations that occur along the interface between a metal and dielectric [26]. Plasmons can be excited in many metals such as copper, silver and gold [27].

#### 1.4.1 Optical response and the Drude model

A simple model can be used to describe how conduction electrons respond to optical excitation. This model was proposed by Paul Drude in 1900 and is therefore referred to as the Drude model [28].

The dielectric function,  $\epsilon(\omega)$ , described by the Drude model takes the following form [29]:

$$\epsilon(\omega) = \epsilon_{\infty} \left( 1 - \frac{\omega_p^2}{\omega^2 + i\gamma_0\omega} \right). \quad (1.1)$$

Here,  $\epsilon_{\infty}$  is a background real dielectric function which is constant and  $\gamma_0$  is a damping term. The damping effects arise due to collisions between electrons and/or crystal impurities.  $\omega_p$ , the plasmon frequency, represents the natural oscillation frequency of the electrons in the free electron plasma [29]. This is given by

$$\omega_p = \sqrt{\frac{ne^2}{m\epsilon_0\epsilon_{\infty}}} \quad (1.2)$$

where  $n$  is the number density of free electrons with a mass  $m$ ,  $e$  the electron charge and  $\epsilon_0$  is the permittivity of free space.

The conditions for surface plasmon resonance are related to the real and imaginary parts of the dielectric function Eq.(1.1).

The real part is given by

$$Re(\epsilon(\omega)) = \epsilon_{\infty} \left( 1 - \frac{\omega_p^2}{\omega^2 + \gamma_0^2} \right) \quad (1.3)$$

and the imaginary part by

$$Im(\epsilon(\omega)) = \frac{\epsilon_{\infty}\omega_p^2\gamma_0}{\omega(\omega^2 + \gamma_0^2)} \quad (1.4)$$

For surface plasmon resonance the real part of the dielectric constant is negative and the imaginary part is small. If the concentration of conduction electrons is effected by the action potential, there is the possibility that the resonance frequency will be altered. An estimate of this is included in the conclusion.

For biological purposes gold is a particularly good substrate as it is inert and, unlike silver, it is not cytotoxic so cells can be grown on it easily.

## 1.5 Outline

An outline of the rest of the thesis is as follows.

Chapter 2 details the physical phenomena that occur during an action potential and also gives more background on existing neuronal models. The

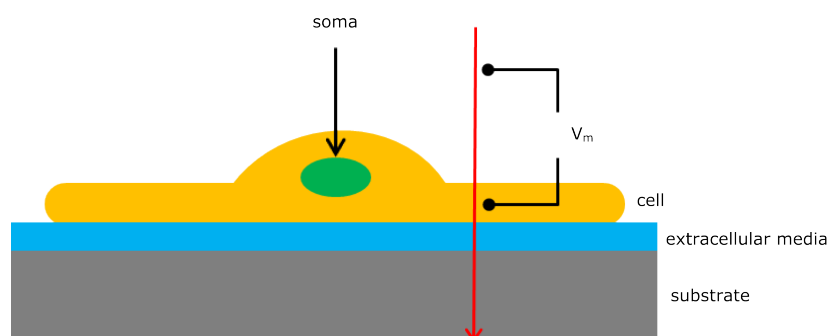


Figure 1.5: Simple schematic of a cell growing on a substrate. The red arrow indicates the one-dimensional cross section simulated in the model described in chapters 4 - 6. The blue extracellular media surrounds the cell, but only the layer between the cell and substrate is shown for clarity. Also indicated is the potential difference,  $V_m$ , between the inside and outside of the cell.

Hodgkin Huxley (HH) model is given particular attention as the model is suited to the development of a scheme capable of calculating ion concentrations and spatio-temporal electric fields in and around neurons. This is because the HH model describes explicitly the flow of ions through the membrane. These ion flows can then be used to calculate the corresponding changes in ion concentration both inside and outside the cell.

The extension of the Hodgkin Huxley model and the numerical methods involved in simulating it are discussed in Chapter 3 along with the drift diffusion and Poisson equations which govern the flow of ions in the intra/extracellular solutions.

These numerical methods are then used, as discussed in Chapter 4, to simulate a simple model of a single membrane separating intracellular and extracellular solutions. In this case, Hodgkin Huxley dynamics control ion flow through the membrane. The HH dynamics are combined with the drift diffusion ion transport and Poisson equations modelling the ion flow within both the intracellular and extracellular media. This gives the Drift Diffusion enhanced Hodgkin Huxley model (DDHH). Although this model is still very simplistic, it allows the idea of incorporating the Hodgkin Huxley model into a drift diffusion framework to be tested. A more realistic and advanced scenario that extends the single membrane model to a one dimensional slice through a neuron is discussed in Chapter 5. This means that there are two membrane layers modelled in the system, which comprises a full slice

through the cell. Also included is a restrictive boundary representing the glass cover slip on which cells are sometimes grown. This is important as it demonstrates the ability to model a restricted extracellular space. Figure 1.5 shows a schematic of the neuron growing on a substrate and the one dimensional cross section which is used in the models presented in this thesis.

A further extension is developed in Chapter 6 which adds an extra layer to the model representing a gold film. The gold film is included because there have been attempts to use surface plasmon resonance to detect neural activity [30; 31]. In these experiments, cells are grown on a gold film which can sustain the surface plasmons. When stimulated by light, in most cases a laser, resonant oscillations of the conduction electrons can occur along the boundary between the gold film and the extracellular media.

The model presented in this thesis could be extended to gain a better understanding of the SPR experiments. These ideas are discussed in the concluding chapter.

## 1.6 Possible Extensions

Other ideas for extensions to the model are also considered in Chapter 7. For example it should be possible to increase the usability of the model by using the cable equation to model the 2D propagation of nerve impulses down an axon (again tracking the intra and extracellular concentration changes). This 2D information could then be used to calculate the magnetic fields. If sufficient changes in the magnetic field occur during an action potential then a range of high resolution magnetic field sensors, (e.g. BEC microscopes, SQUIDS or diamond N-V centres) could be used as detectors of nerve activity.

A Bose Einstein Condensate (or BEC) microscope [21; 32; 33] could have the potential to be used as a field sensor with sufficient spatial and temporal resolution to resolve magnetic field changes associated with neural activity [34]. A simple schematic of this setup is shown in Figure 1.6. A condensate is trapped above a current source and used to image the magnetic field generated by electric currents associated with neuron activity. This is possible because the condensate is trapped using magnetic fields, so any variation of these fields can cause a change in the density profile of the

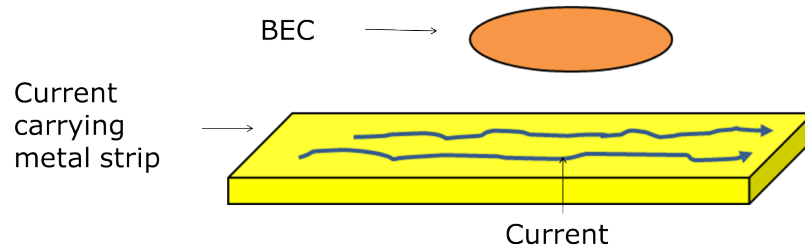


Figure 1.6: A simple schematic of a typical BEC microscopy setup [21]. The Bose-Einstein condensate is trapped above a current source. Since the condensate is trapped magnetically, any changes in the magnetic field resulting from the current flow alter the atom density profile of the cloud. This profile can be imaged using a camera and used to reconstruct the current flows.

cloud. The density profile can be imaged using a camera and so the changes can be used to reconstruct the current flows.

There would be a few practical issues to overcome before such experiments could take place. These include placing the BEC in a vacuum, within  $1\mu\text{m}$  from the cell to be within effective operational range.

Other possibilities for detecting the magnetic fields produced by ion transport in neurons and neural networks include superconducting quantum interference devices (SQUIDs) or diamond N-V centres, which are also capable of detecting magnetic fields with a high sensitivity and spatial resolution.

# Chapter 2

## Background

### 2.1 Neurons and Networks

This chapter discusses some of the theoretical tools used in the simulations presented in chapters 4, 5 and 6. Some background relating to neuronal modelling is also discussed, with a particular emphasis on the Hodgkin Huxley model.

In order to understand the behaviour of neurons, a large variety of models have been developed over the years. These can be classified into two types: those which try to model the complexities of an individual neuron accurately, and those which simplify the treatment of individual neurons in order to make it easier to model large numbers of neurons in neural networks.

These models will be discussed in the rest of this chapter. Some of the models discussed will not be suitable for the purposes we require, but provide good examples of the kind of modelling that is done elsewhere.

### 2.2 The Hodgkin Huxley Model

One of the most significant models of a neuron is the Hodgkin Huxley Model [35; 36; 37; 38; 39]. It is still widely regarded as the gold standard to which other neuron models are compared. Since the publication of the original papers, many different ion channel types have been discovered, which can be modelled in a similar way to the channels of the Hodgkin Huxley model [40]. In the model there is a set of three conductances which allow current to flow through the membrane. It is then possible to express the total current

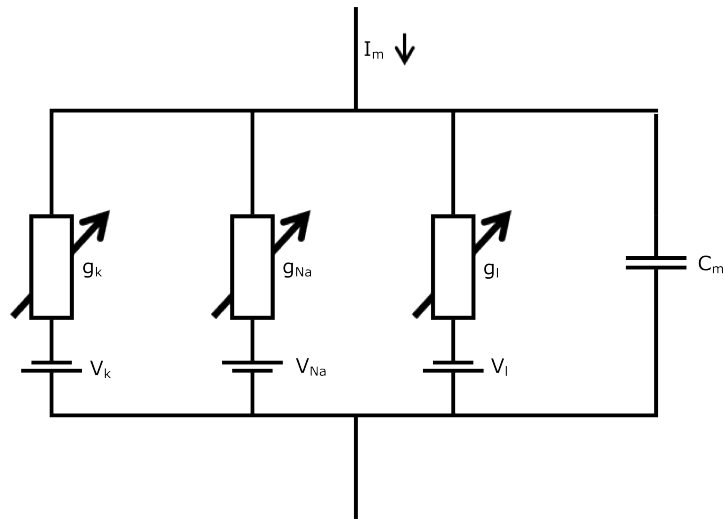


Figure 2.1: Equivalent circuit for the Hodgkin Huxley model. The membrane is modelled as a leaky capacitor. The three membrane currents (potassium, sodium and leakage) are controlled by three variable resistors  $g_K$ ,  $g_{Na}$  and  $g_l$ . The difference between the membrane potential  $V_m$  and the Nernst potential for each ion ( $V_K$ ,  $V_{Na}$  and  $V_l$ ) determines the driving force of the battery. The membrane current is  $I_m$  and the membrane capacitance is  $c_m$

across the membrane in terms of a sum of the different ionic currents, the sodium, potassium and leak currents.

The Hodgkin and Huxley model is often considered in terms of its circuit equivalent, as shown in figure 2.1. The membrane is modelled as a leaky capacitor. Voltage dependent currents (modelled as resistors) allow the membrane potential difference to change.

In a series of experiments Hodgkin and Huxley were able to establish that the ionic currents depend on the voltage across the membrane. By taking a series of measurements they were able to calculate the voltage dependence of the conductances for the three different currents.

### 2.2.1 Voltage Clamp Experiments

Hodgkin and Huxley performed many experiments using the voltage clamp technique on the giant axon of a squid [41]. Two electrodes were inserted into the giant axon. One of which was used in conjunction with another electrode in the surrounding medium to measure the voltage across the cell membrane. The other electrode was used to maintain the difference in

potential across the membrane at a constant level. To do this, current would have to be injected into or removed from the membrane. By measuring the current it is possible to calculate the conductance of the membrane.

### 2.2.2 The Model

The equation that relates the change in potential difference across the membrane to the current through the membrane is as follows:

$$C_m \frac{\partial V_m}{\partial t} = -(j_{Na} + j_K + j_l) + \frac{I_{ext}}{a_m}. \quad (2.1)$$

where  $C_m$  is the capacitance per unit area of the membrane and  $V_m$  is the potential difference across the membrane. The current through the membrane is split into three terms,  $j_{Na}$  which is the sodium current density,  $j_K$  which is the potassium current density and  $j_l$  which is the leakage current density. An additional term  $I_{ext}$  represents the externally applied current, with the constant  $a_m$  being defined as the cross sectional area of the axon. When  $I_{ext} = 0$  the system is unstimulated.

Each current can be expressed in terms of Ohm's law using a conductance and potential difference as a driving force.

The sodium current is given by

$$j_{Na} = g_{Na} (V_m - V_{Na}) \quad (2.2)$$

where  $g_{Na}$  is a conductance and  $V_{Na}$  is the Nernst potential for sodium. In general terms the Nernst potential is the potential at which a given ion species is in equilibrium. At this potential there would be no current flow for that particular ion.

In a simple system containing only one ion species the Nernst potential would be the equilibrium value of the whole system. In a system consisting of multiple ionic species, the equilibrium value of the system, known as the resting potential, is a weighted average of the different ionic Nernst Potentials.

The Nernst potential representing the equilibrium value that the potential difference would reach if two different concentrations of sodium were separated by a membrane can be calculated as follows:

$$V_{Na} = \frac{k_b T}{e} \ln \left( \frac{c_{Na,out}}{c_{Na,in}} \right). \quad (2.3)$$

In equation (2.3)  $c_{Na,out}$  is the concentration of sodium ions outside the cell and  $c_{Na,in}$  is the concentration of sodium ions inside the cell.

Similar equations can be used to calculate the Nernst potential for the other ionic species. By fitting experimental data from their voltage clamp experiments, Hodgkin and Huxley were able to deduce the form of the conductance for sodium. This is described as

$$g_{Na} = g_{\bar{Na}} m^3 h \quad (2.4)$$

where  $g_{\bar{Na}}$  is the maximum value for the sodium conductance,  $m$  and  $h$  are gating variables which determine what proportion of ion channels are open at any given time.  $h$ ,  $m$  and  $n$  take values between 0 and 1, so can be interpreted as the probability of the gate in question being open. These gating variables change over time according to a set of gating equations.

$$\frac{dm}{dt} = \alpha_m (1 - m) - \beta_m m \quad (2.5)$$

$$\frac{dh}{dt} = \alpha_h (1 - h) - \beta_h h \quad (2.6)$$

where the  $\alpha$  and  $\beta$  parameters are defined below. The potassium current can be described in a similar way.

$$j_K = g_K (V_m - V_K). \quad (2.7)$$

with the Nernst potential  $V_K$  given by

$$V_K = \frac{k_b T}{e} \ln \left( \frac{c_{K,out}}{c_{K,in}} \right) \quad (2.8)$$

where  $c_{K,out}$  is the external potassium concentration and  $c_{K,in}$  is the internal potassium concentration. For potassium the conductance depends on only one gating variable  $n$

$$g_K = g_{\bar{K}} n^4 \quad (2.9)$$

This variable also obeys a gating equation similar to  $m$  and  $h$ .

$$\frac{dn}{dt} = \alpha_n (1 - n) - \beta_n n \quad (2.10)$$

The various  $\alpha$  and  $\beta$  parameters are functions of the voltage difference across the membrane.

$$\alpha_m = \frac{(100(-1000(V_m - V_{rest}) + 25))}{\left( \exp \left( \frac{(-1000(V_m - V_{rest}) + 25)}{10} \right) - 1 \right)}; \quad (2.11)$$

$$\beta_m = 4000 \exp\left(\frac{-1000(V_m - V_{rest})}{18}\right) \quad (2.12)$$

$$\alpha_h = 70 \exp\left(\frac{-1000(V_m - V_{rest})}{20}\right) \quad (2.13)$$

$$\beta_h = \frac{1000}{\exp\left(\frac{-1000(V_m - V_{rest}) + 30}{10}\right) + 1} \quad (2.14)$$

$$\alpha_n = \frac{10(-1000(V_m - V_{rest}) + 10)}{\exp\left(\frac{-1000(V_m - V_{rest}) + 10}{10}\right) - 1} \quad (2.15)$$

$$\beta_n = 125 \exp\left(\frac{-1000(V_m - V_{rest})}{80}\right) \quad (2.16)$$

These  $\alpha$  and  $\beta$  parameters were calculated by Hodgkin and Huxley numerically fitting experimental data obtained from the squid giant axon. These parameters control the rates at which the gating variables can change and are dependent on the membrane potential.

There is also a leakage current in the Hodgkin Huxley model, which combines the contributions from various ion species. The leakage current is

$$j_l = g_l (V_m - V_l). \quad (2.17)$$

The leakage current has a different character to the sodium and potassium currents due to it having a fixed conductance that does not depend on gating variables.

The quantity  $V_{rest}$  in equations (2.11)-(2.16) is the potential difference across the membrane in its resting state. This can be calculated using the Nernst potentials for the different currents, weighted by the conductances, as follows

$$V_{rest} = \frac{g_{Na,rest}}{g_{tot}} V_{Na} + \frac{g_{K,rest}}{g_{tot}} V_K + \frac{g_{l,rest}}{g_{tot}} V_l. \quad (2.18)$$

The variable  $g_{tot} = g_{Na,rest} + g_{K,rest} + g_{l,rest}$  is the sum of the three resting conductances. The resting conductance values,  $g_{Na,rest}$ ,  $g_{K,rest}$  and  $g_{l,rest}$ , in Equation (2.18) are calculated by setting  $V_m = V_{rest}$  in the  $\alpha$  and  $\beta$  parameters and finding the values of  $m$ ,  $n$  and  $h$  that set equations (2.5), (2.6) and (2.10) to zero.

$$m_{rest} = \frac{\alpha_{m,rest}}{\alpha_{m,rest} + \beta_{m,rest}}. \quad (2.19)$$

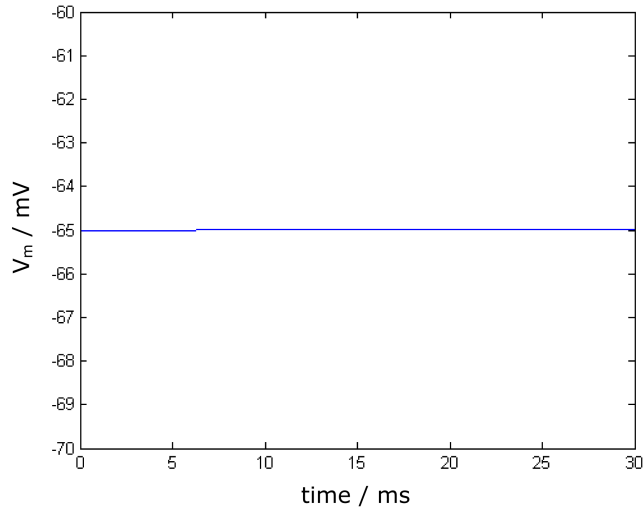


Figure 2.2: When initialised in the resting state, the neuron remains in the resting state until stimulated.

where  $\alpha_{m,rest}$  and  $\beta_{m,rest}$  are the values of the  $\alpha_m$  and  $\beta_m$  when  $V_m$  is equal to  $V_{rest}$ . Similar formulae give the resting values for the other gating variables.

These resting gate values are used along with the relevant conductance equations(2.4) and (2.9) for sodium and potassium respectively. Since the leak conductance is constant  $g_{l,rest} = g_l$ .

## 2.3 Results and features of the Hodgkin Huxley model

The nonlinearity present in the defining equations for the Hodgkin Huxley model allows a rich variety of neuronal behaviours. The behaviour observed depends on the stimulation used. If no stimulation is used and the membrane is initialised in the resting state  $V_m = V_{rest}$  then the membrane potential will remain at its resting value. This is shown in Figure 2.2. If the system is set up so that the membrane is initially in a non resting state, the potential will evolve to the resting state and then settle down. This is seen in Figure 2.3

More interesting behaviour occurs if a stimulating current is applied. A stimulating current depolarises the membrane. If this depolarization is above a threshold a positive feedback occurs leading to an action potential [42]. This behaviour is illustrated in Figure 2.4. If the stimulus is below

## 2.3 Results and features of the Hodgkin Huxley model

---

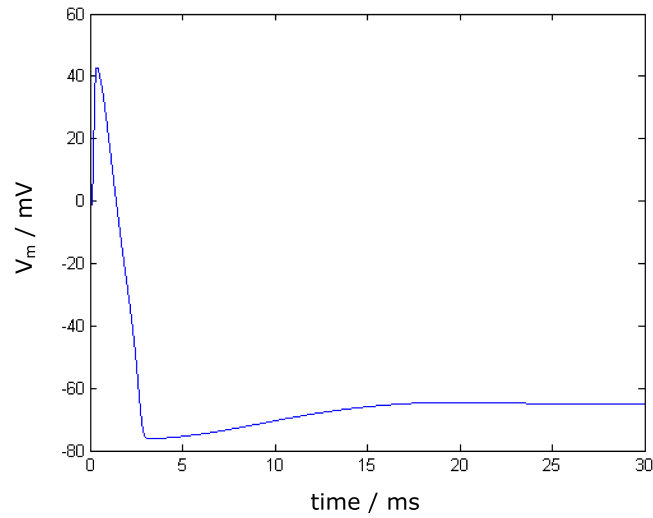


Figure 2.3: When initialised in a non resting state, the Hodgkin Huxley system evolves according to the gating equations until the resting potential is restored. The evolution depends on the initial conditions.

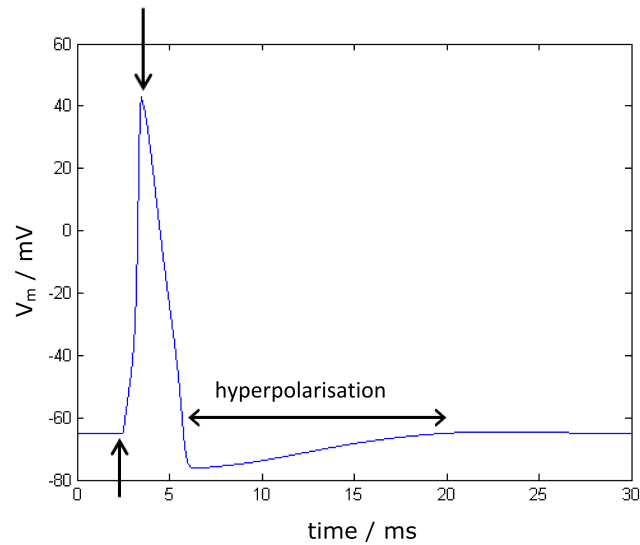


Figure 2.4: A typical Hodgkin Huxley action potential. After the stimulus is applied (left arrow), it depolarises the membrane, the sodium ion channels open allowing sodium to rush into the cell. This leads to rapid further depolarisation, which causes the potential difference across the membrane to become positive. The potassium channels then open (right arrow) allowing potassium to leave the cell. This begins to restore the cell to its resting state. However, since the potassium channels are slower, it takes longer for them to close, causing a brief period of hyperpolarisation known as the refractory period.

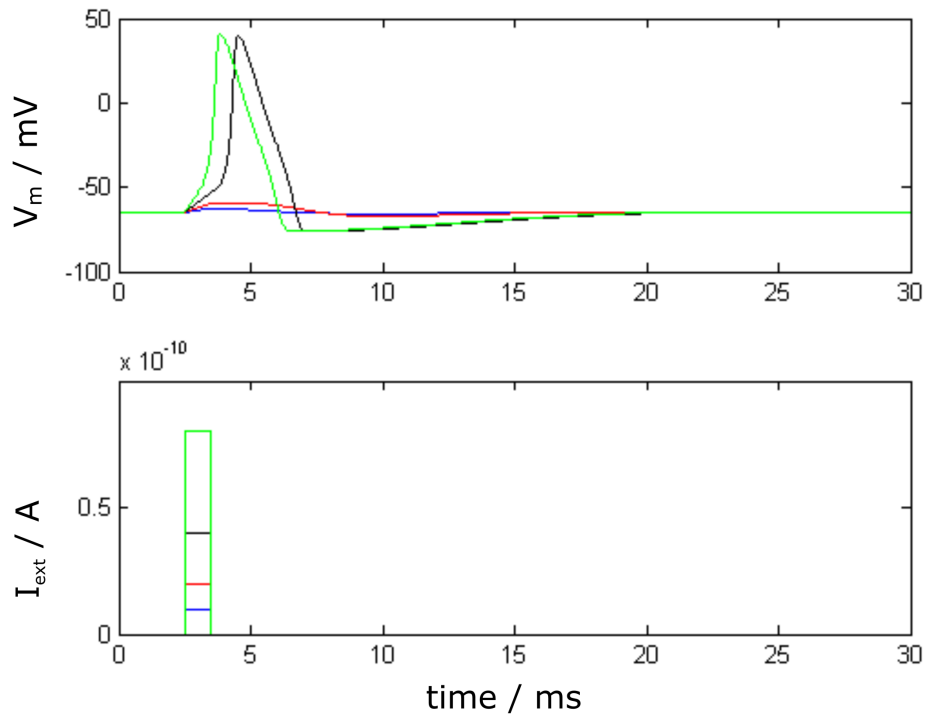


Figure 2.5: Top panel: Membrane potential in response to different current pulse stimuli. Two stimuli (blue and red lines) are subthreshold and do not trigger an action potential. Other stimuli are above threshold and therefore do trigger an action potential. (black and green lines) Bottom Panel : current pulses.

threshold, the membrane potential decays back to the resting potential. A selection of different stimuli are used to illustrate this effect in Figure 2.5. In Figure 2.5 a variety of current pulses are applied within the Hodgkin Huxley model. Two of these (the blue and red lines) are not sufficient to cause the membrane potential to rise above the threshold. This means that the potential is just slightly depolarised by the stimulus and then gradually returns to the resting state.

The stronger stimuli (black and green lines) are sufficient to trigger an action potential. Note that there is little difference between the shape of the action potentials, even though the magnitude of the largest current pulse is twice that of the other threshold stimulus. The larger stimulus does reach the threshold more quickly and so the action potential is triggered earlier.

The behaviour of the gating variables along with a membrane potential trace are shown in Figure 2.6. After the stimulus,  $m$  rises sharply allowing

## 2.3 Results and features of the Hodgkin Huxley model

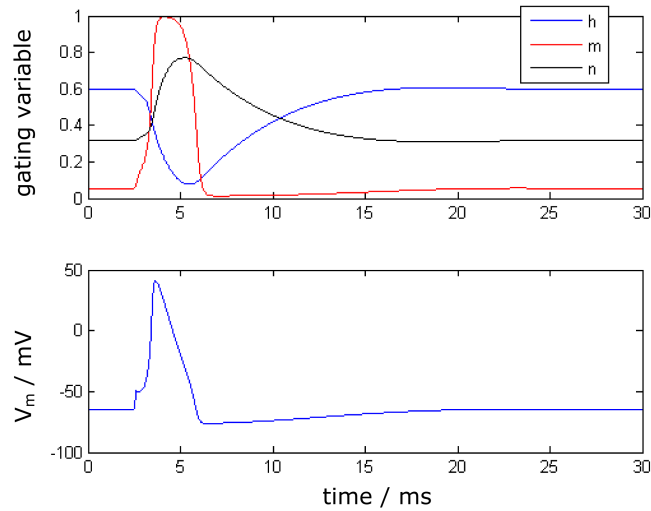


Figure 2.6: Top panel: Evolution of the Hodgkin Huxley gating variables during an action potential.  $h$  and  $m$  gates control the sodium current, the  $n$  gate controls the potassium current. Bottom Panel: Membrane potential trace allowing the behaviour of the gating variables to be considered alongside the behaviour of the membrane potential.

movement of sodium ions, even though the  $h$  value is decreased. This is because the sodium currents have a cubic dependence on  $m$  but only a linear dependence on  $h$ . The  $n$  gate which regulates the potassium current is slower to respond, but also rises following the stimulus. Due to the currents depending on different powers of the gating variables, it is useful to look at the current flows in order to get an idea of what happens during an action potential.

Figure 2.7 shows the currents in the Hodgkin Huxley model. These are, a sodium current, a potassium current and a leakage current (attributed to chloride ions).

After a time of approximately 3ms there is a noticeable drop in the magnitude of the sodium current (blue curve) which occurs because as the membrane depolarises and so the membrane potential rapidly tends towards the Nernst potential for sodium. As a result, the term  $V_m - V_{Na}$  in equation (2.2) becomes very small and reduces the current. It is also noticeable that there is a significant sodium current during the potassium current (red curve) phase of the action potential, indicating that both sodium and potassium channels are open during a significant portion of the action potential. The chloride current (black curve) is considerably smaller in magnitude as

## 2.3 Results and features of the Hodgkin Huxley model

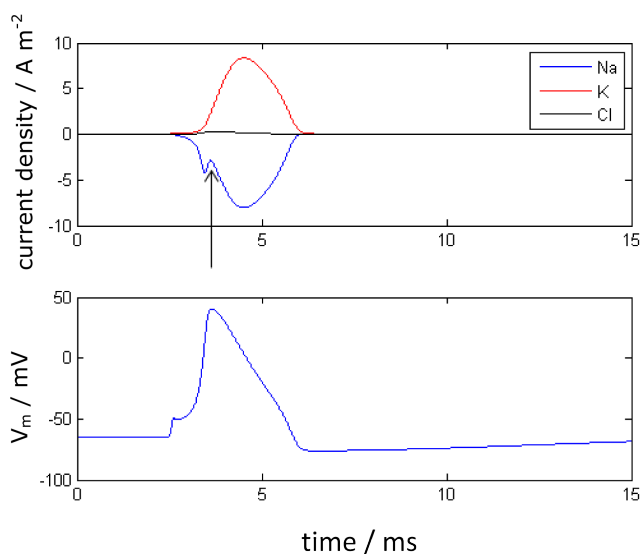


Figure 2.7: Ionic currents during a Hodgkin Huxley action potential. Notice that the sodium current (blue curve) is slightly faster than the potassium one (red curve). The leakage current is attributed to chloride ions (black curve). The feature indicated by the arrow is the region in which the membrane potential tends towards the sodium Nernst potential and so the sodium current magnitude is reduced.

it is a leakage current. It is a passive current that is not affected by ion channels, although there is a noticeable peak in the chloride current, which corresponds to the position where the membrane potential is far from the equilibrium chloride Nernst potential.

It is also interesting to look at the phase space plots of the various gating variables against voltage.

Figures 2.8, 2.9, 2.10 show phase space plots of the three gating variables against membrane potential under a constant applied current. From these it is clear that the system tends towards a stable limit cycle, which will be noticeable as repeated firings of action potentials.

One feature of the Hodgkin Huxley model is that as the stimulating current is increased, the frequency of the action potentials also increases.

This is shown in figure 2.11, in which the constant current is plotted against the frequency of the action potentials. The steep rise in frequency indicates the transition from non-spiking sub threshold behaviour to full active spiking.

Even though the Hodgkin Huxley model is quite complicated with 5

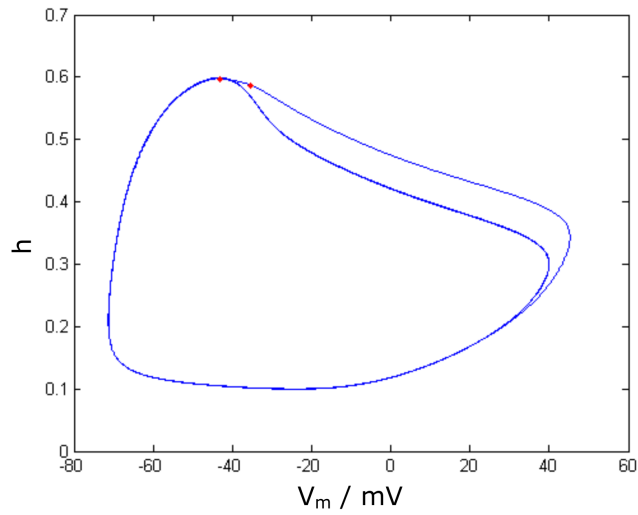


Figure 2.8: Plot of the  $h$  gate against membrane potential under constant current stimulation. Two points from the first cycle are indicated as red dots for clarity.

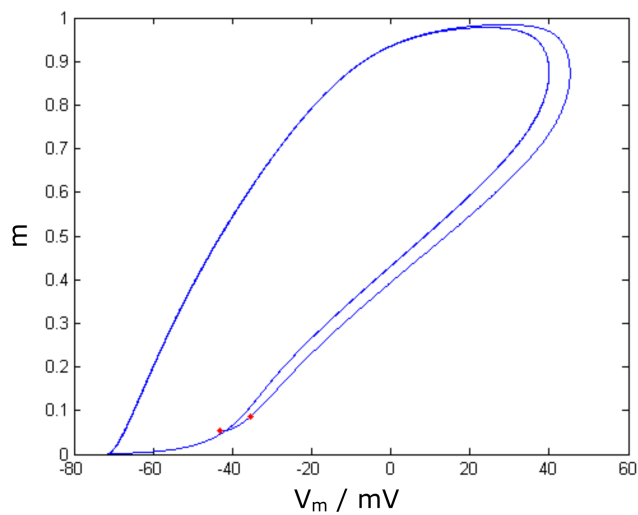


Figure 2.9: Plot of the  $m$  gate against membrane potential under constant current stimulation. Two points from the first cycle are indicated as red dots for clarity.

## 2.3 Results and features of the Hodgkin Huxley model

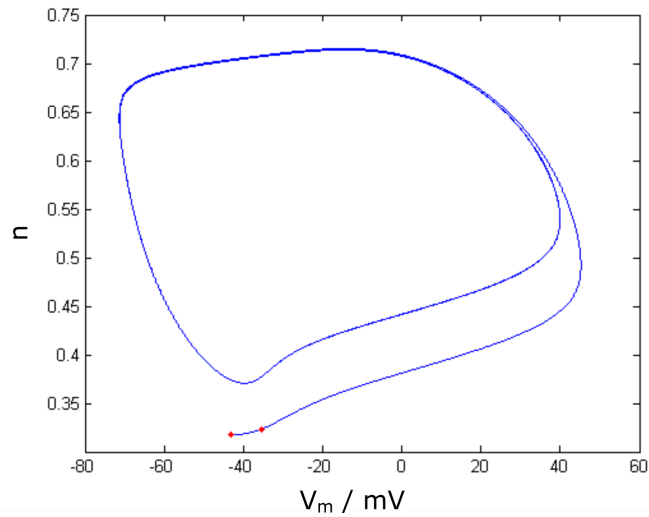


Figure 2.10: Plot of the  $n$  gate against membrane potential under constant current stimulation. Two points from the first cycle are indicated as red dots for clarity.

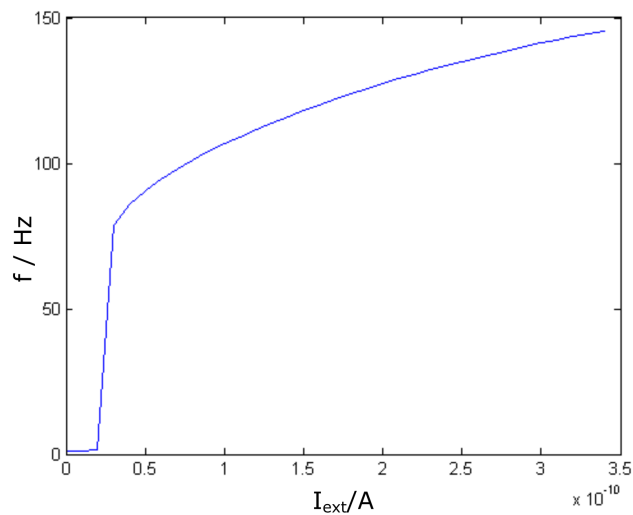


Figure 2.11: Frequency of neuron firing events calculated against current curve for continuously applied current using the Hodgkin Huxley model. To produce this, a continuous current was applied and the frequency of the resulting activity was plotted against that current value. This process was repeated for a range of different applied currents.

defining equations and numerous parameters, it is the best model to use as it allows the concentration profiles of ions inside and outside the cell to be modelled. This allows the intra and extracellular media to be modelled using drift-diffusion equations.

These equations and the computational techniques used to solve them are discussed in detail in the following chapter. The next section briefly reviews a few other simple neuron models.

## 2.4 Simple Neuron Models

There are neuronal models of varying degrees of complexity. Probably the simplest of these is the integrate and fire model.

The equation describing the change in potential difference across the membrane,  $V_m$  due to a current input  $I$  is

$$c_m \frac{dV_m}{dt} = I(t). \quad (2.20)$$

where  $c_m$  is the capacitance of the membrane. In the integrate and fire model, the potential difference across the membrane increases when current is applied. When it reaches a set threshold voltage,  $V_{th}$ , a spike is fired in the form of a delta function and the voltage is reset to its resting value.

Another simple model is the Leaky Integrate and Fire model (LiF)[43], as its name suggests this model is created by adding a leak term to the integrate-and-fire model. It is a spike producing model with a threshold, which is computationally easier than the more complex Hodgkin Huxley type models. This makes it a good model to use for networks, where it is necessary to model large numbers of neurons at any given time. The defining equation in the leaky integrate and fire model is as follows

$$\tau_m \frac{dV_m}{dt} = -V_m + RI. \quad (2.21)$$

where  $\tau_m$  is the membrane time constant,  $R$  the resistance and  $I$  the input current. Unlike the Hodgkin Huxley model, the spiking dynamics are not built into the equation. Instead, once a threshold voltage  $V_{threshold}$  is reached the membrane voltage is reset to the resting potential  $V_{rest}$ .

An example of the kind of spiking behaviour produced by the leaky integrate and fire model is shown in Figure 2.12. It is clear from comparison with Figure 2.4 that the shape of the spikes produced is very different from

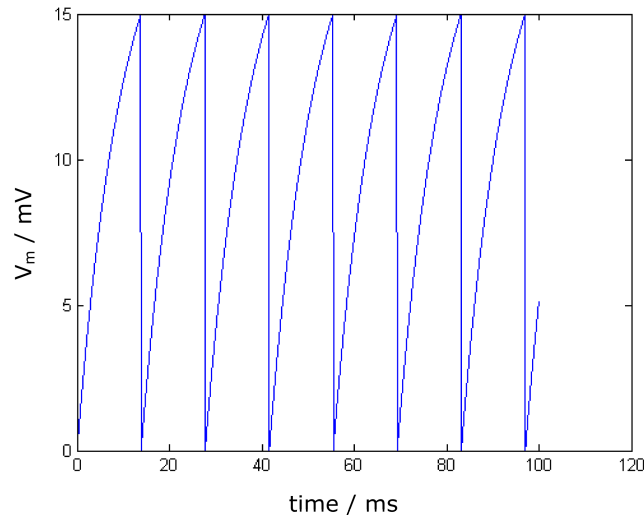


Figure 2.12: Leaky integrate and fire model under a constant current stimulus. The membrane potential,  $V_m$ , rises until it reaches a threshold of 15 mV, once this is reached the potential is reset to the resting potential. The reset is a mathematical artefact introduced to mimic the return to resting state seen in real neurons

those obtained using the Hodgkin Huxley model. The model can be made a little more complex by including a refractory period during which further stimulation is not possible. Although the leaky integrate and fire model is simple and relatively easy to compute, it doesn't accurately describe the range of dynamical behaviours found in neurons. It also has no way of distinguishing the different types of current, which are used to update the drift diffusion enhanced Hodgkin Huxley model discussed in the next chapter.

Another model which is often used is the Fitzhugh Nagumo model [44]. This uses two defining equations and is described as a simplified Hodgkin Huxley model.

$$\frac{dV_m}{dt} = V_m - \frac{V_m^3}{3} - w + I_{ext}. \quad (2.22)$$

where  $w(t)$  is a linear recovery variable which also changes in time according to:

$$\tau \frac{dw}{dt} = V_m + a - bw. \quad (2.23)$$

and  $I_{ext}$  is the externally applied current. The form of equation (2.22) and equation (2.23) is a result of reducing the four Hodgkin Huxley equations to a pair of equations. The cubic term in equation (2.22) gives rise to negative

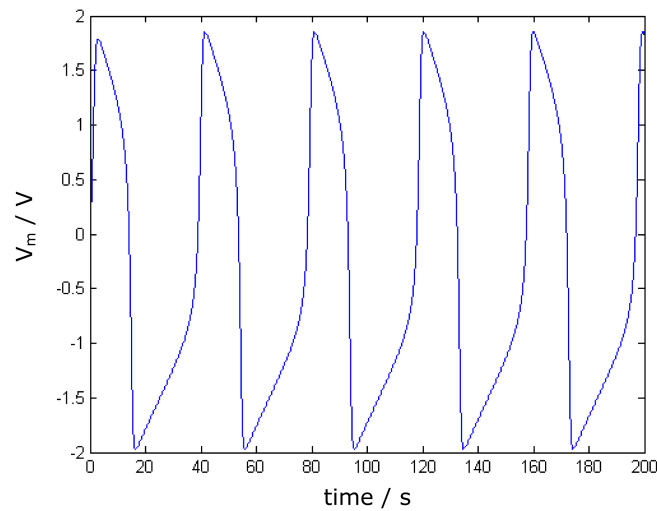


Figure 2.13: An example of the Fitzhugh Nagumo model under stimulation. These spikes look more like the action potentials produced by the Hodgkin Huxley model, see Figure 2.4. The spiking dynamics arise due to the equations 2.3 and 2.4, rather than using a logic condition as in the Leaky Integrate and fire model.

differential resistance, whereby an increase in voltage reduces the current flow. This to some extent mimics the non-linear membrane conductance in the Hodgkin Huxley model. The Fitzhugh Nagumo model produces spikes with more detail than in the Leaky Integrate and Fire model, but it still doesn't provide a link to the ionic currents and so is also not suitable for our purposes.

Figures 2.13 and 2.14 show the two variables in the Fitzhugh Nagumo model and the spikes caused by a constant current input.

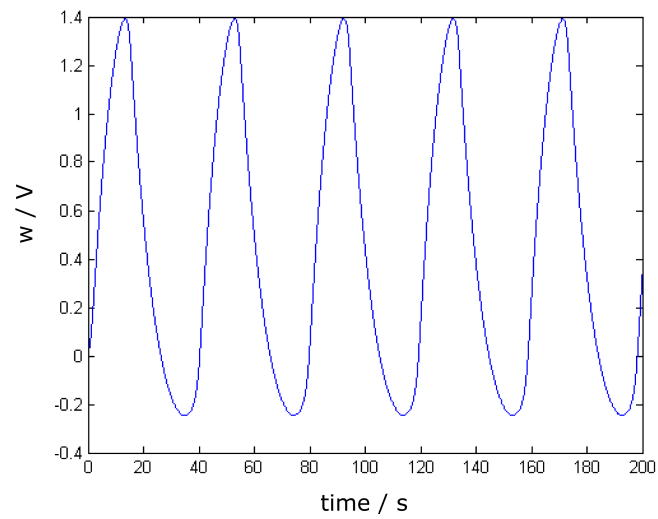


Figure 2.14: An example of the Fitzhugh Nagumo model under stimulation. This plot shows the recovery variable  $w$ .

# Chapter 3

## Methods

Although the Hodgkin Huxley model is well established, it is not on its own sufficient for our purposes. This is because it doesn't track the evolving concentration profiles inside and outside the cell. The voltage dependent membrane currents calculated by the Hodgkin Huxley model can be used to calculate the changes to concentration profiles using the drift diffusion equations.

This chapter outlines the equations and tools needed to effectively model the neuron and its extracellular environment. The model splits the computational domain into regions which feature particular ionic properties. The number of these regions depends on the complexity of the situation being simulated.

In all cases, a 1D slice through the system is taken as indicated in Figure 3.1. It is assumed that the solutions are homogeneous in all planes parallel to the membrane, which is a reasonable assumption when modelling the cell body.

### 3.1 The Drift-Diffusion and Poisson Equations

The simulations described in this thesis do not attempt to track individual ion movements, but rather deal with the changes in ion concentration and electric field over time. For each ion species,  $i$ , the flux  $J_i$  is calculated at temperature,  $T$ , as follows [45]:

$$J_i = -D_i \left( \frac{\partial c_i}{\partial x} + \frac{z_i F}{RT} c_i \frac{\partial \theta}{\partial x} \right) \quad (3.1)$$

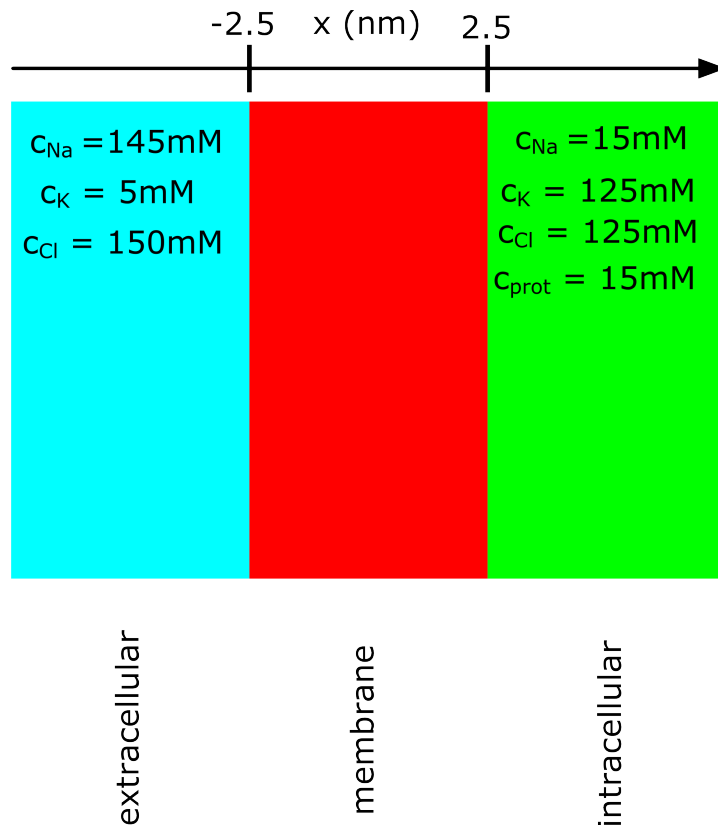


Figure 3.1: Schematic showing the model structure for the single membrane. A membrane separates regions of extracellular and intracellular space. The ionic concentrations of the two solutions are indicated. The concentrations change smoothly through the membrane according to tanh functions. The rate at which ions are able to move through the membrane depends on the current state of the gating variables according to the Hodgkin Huxley model as discussed in Chapter 2

### 3.1 The Drift-Diffusion and Poisson Equations

---

where  $D_i$ ,  $z_i$  and  $c_i$  are the diffusion coefficient, charge and concentration of the ion species  $i$  and  $\theta$  is the potential. In Equation (3.1),  $R$  is the gas constant and  $F$  is Faraday's constant. The first term on the right hand side of Equation (3.1) corresponds to the diffusion of the ions, whilst the second term describes the drift effect of the electric field  $E = -\frac{\partial\theta}{\partial x}$  on the charged ion species.

The time evolution of the concentration profiles is then found by considering the conservation of mass

$$\frac{\partial c_i}{\partial t} = -\frac{\partial J_i}{\partial x}, \quad (3.2)$$

where  $t$  is the time. The concentrations of the different ion species are coupled through the potential  $\theta(x, t)$ , which must satisfy Poisson's equation at all points in the domain, i.e.

$$\epsilon \frac{\partial^2 \theta}{\partial x^2} + \frac{\partial \epsilon}{\partial x} \frac{\partial \theta}{\partial x} + \sum_i z_i c_i = 0. \quad (3.3)$$

Equation (3.3) allows a spatially varying permittivity  $\epsilon(x)$  to be used [46]. This is necessary as each layer in the model has a different permittivity that reflects its local structure. The membrane's permittivity is very different from that of the saline solutions inside and outside the cell. The permittivity profile becomes even more complicated when considering additional layers such as glass and gold.

In the models there are three mobile ion species, sodium, potassium and chloride. For each ion, the flux (3.1) and conservation of mass (3.2) equations can be combined to give

$$\begin{aligned} \frac{\partial c_i}{\partial t} = & \frac{\partial D_i}{\partial x} \left( \frac{\partial c_i}{\partial x} + \frac{z_i F}{RT} c_i \frac{\partial \theta}{\partial x} \right) \\ & + D_i \left( \frac{\partial^2 c_i}{\partial x^2} + \frac{z_i F}{RT} \frac{\partial c_i}{\partial x} \frac{\partial \theta}{\partial x} + \frac{z_i F}{RT} c_i \left( -\frac{\rho}{\epsilon \epsilon_0} - \frac{1}{\epsilon} \frac{\partial \epsilon}{\partial x} \frac{\partial \theta}{\partial x} \right) \right), \end{aligned} \quad (3.4)$$

where Equation (3.3) has been used to eliminate the  $\frac{\partial^2 \theta}{\partial x^2}$  term and  $\rho(x, t) = \sum_i z_i c_i$  is the local charge density. The local charge density includes contributions from the mobile ion species, sodium, potassium and chloride, as well as contributions from fixed charges on the protein molecules.

## 3.2 The Membrane

Rather than using boundary conditions at the membrane, a variable diffusion coefficient is used to control the flux through the membrane. This is sensible because the diffusion coefficient determines the ability for ions to diffuse through the membrane. It is also simple to implement within the framework of the drift diffusion equations. This involves matching the flux expected from the Hodgkin Huxley model to the flux equations in the initial state, then altering the diffusion coefficient within the membrane in proportion to the Hodgkin Huxley gating variables. The following discussion outlines the situation for sodium, but a similar procedure was followed for the other ions.

The initial flux of sodium can be described as follows:

$$J_{Na} = -\frac{z_{Na}g_{Na,init}(V_m - V_{Na})}{F}, \quad (3.5)$$

where  $z_{Na}$  is the charge (in units of  $e$ ) on the sodium ions,  $g_{Na}$  is the membrane conductance for sodium,  $V_m$  is the potential difference across the membrane and  $V_{Na}$  is the Nernst potential for sodium given by Equation (2.3). This flux must also be equivalent to the flux defined by Equation (3.1). Using this equivalence, a value for the diffusion coefficient in the membrane can be found

$$D_{Na} = \frac{z_{Na}g_{Na,init}(V_m - V_{Na})}{F\left(\frac{\partial c_{Na}}{\partial x} + \frac{z_{Na}F}{RT}c_{Na}\frac{\partial \theta}{\partial x}\right)}. \quad (3.6)$$

Initially  $V_m = 0$  and  $\frac{\partial \theta}{\partial x} = 0$  and equation (3.6) simplifies to

$$D_{Na} = -\frac{z_{Na}g_{Na,init}V_{Na}}{F\frac{\partial c_{Na}}{\partial x}}. \quad (3.7)$$

This represents the baseline value for the diffusion coefficient for sodium given the initial values of the sodium activation and inactivation gates. As the state of the gates and hence the sodium conductance change, this baseline diffusion coefficient is multiplied by the multiplicative factor  $\frac{g_{Na}}{g_{Na,init}}$ . This means that as the sodium gates open the conductance increases, the membrane diffusion coefficient increases, resulting in a greater flow of sodium ions through the membrane. A similar process is used to calculate the diffusion coefficient for the remaining ion species.

The value given to the diffusion coefficient within the membrane is therefore linked to the number of ion channels open at any given time. An

idealised view of this would be a square function, in which the diffusion coefficient drops to its membrane value and remains at that value throughout the membrane.

Unfortunately this causes issues when trying to solve the equations, due to discontinuities in the derivatives. To work around this, smoothing functions are used which are continuous in the first and second derivative. These functions are discussed in the next section.

In order to stimulate the neuron, it is necessary to initiate some flux of sodium into the cell. This can be done by temporarily increasing the diffusion coefficient for sodium, thereby allowing more sodium ions into the cell. Once this happens, the positive feedback effect described in the Hodgkin Huxley model is induced and if the stimulus is sufficient an action potential is observed. During stimulation the membrane diffusion coefficient for sodium becomes

$$D_{Na,mem} = D_{Na,mem} + D_{Na,stim}, \quad (3.8)$$

where the additional term  $D_{Na,stim}$  causes the extra sodium injection which can trigger an action potential. This mimics the earliest responses to a stimulating current and provides a realistic way of inducing an action potential.

### 3.3 Smoothing with tanh Functions

When initialising the models, the ionic concentrations in the intra and extracellular media are simply the bulk concentrations taken from well known data sources [2; 41] and indicated on the schematic diagram in Figure 3.1.

Situated between the two (extracellular and intracellular) solutions is a membrane over which the concentration must change between the values on either side of the membrane. To implement this a tanh function is used to define the initial concentration profiles within the membrane region. This ensures that the derivatives are smooth and continuous across the simulation space. Other functions were tried including cubic splines and polynomial fits, but these did not produce continuous first and second derivatives which integrated well.

Suppose a function is desired that has a value  $y_L$  at  $x_L$  and a value  $y_R$  at  $x_R$ , a tanh function is used as follows

$$y = a + b \tanh\left(\frac{x - c}{d}\right), \quad (3.9)$$

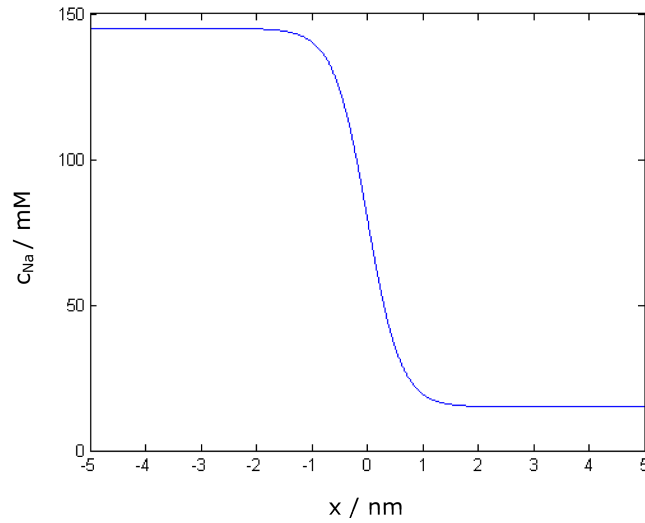


Figure 3.2: Concentration profile of sodium through the membrane. The smooth change from the extracellular values (on the left) to the intracellular values (on the right) is achieved using tanh functions of the form in Equation (3.9).

where  $a = \frac{y_L + y_R}{2}$ ,  $b = \frac{y_R - y_L}{2}$ ,  $c = \frac{x_L + x_R}{2}$  and  $d$  is a parameter which controls how quickly the function changes. When using the tanh functions to describe the transition to the membrane diffusion coefficient, the value of  $d$  controls how rapidly the diffusion coefficient decreases from that of the intra / extracellular solutions. Small values of  $d$  give rise to sharp rapid transitions, whilst larger values give smoother profiles.

The tanh function allows for the step changes to be smoothed whilst still providing an easily differentiable gradient.

Applying the tanh function twice enables the diffusion coefficient of the membrane to be modelled as seen in Figure 3.3

Repeatedly applying Equation (3.9) allows more complex layered structures to be modelled. This becomes important when considering the gold and glass layers, as all of these have properties which are considerably different to those of the intracellular or extracellular media.

The physical properties of these boundaries can also be handled using tanh functions.

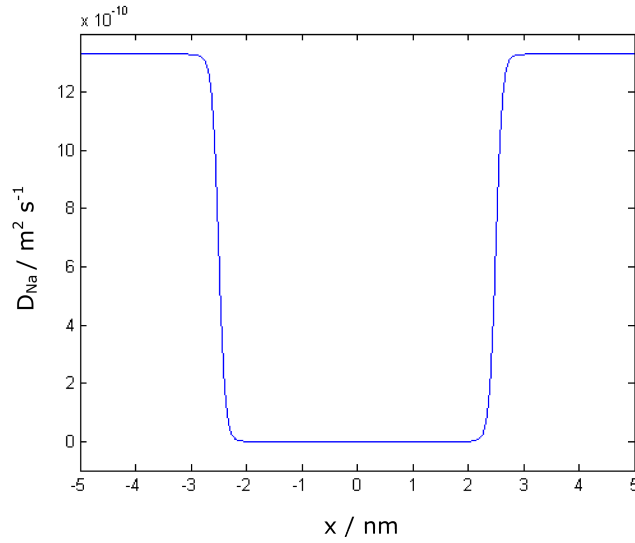


Figure 3.3: Example diffusion coefficient profile for sodium, calculated using tanh smoothing functions. The diffusion coefficient profile for the membrane is similar to a smoothed square well. The region of extremely low diffusion coefficient corresponds to the membrane.

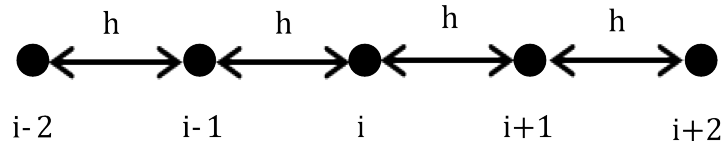


Figure 3.4: Stencil used in central difference approximations on a uniform grid. The points are all uniformly spaced a distance  $h$  apart. Each site is labelled with site index  $i$ .

### 3.4 Discretisation Schemes and the Non Uniform Grid

In order to self-consistently solve the equations (3.3) and (3.4) it is necessary to use a finite differencing scheme to approximate the derivatives [47; 48]. A computational stencil for a uniform grid is shown in Figure 3.4. With this stencil, three finite difference schemes are possible. These are the forward, backward and central differences. Of these, the most accurate is the central difference scheme as we shall show. The approximations to the first and second derivatives can be derived by expressing the values of some function  $U$  at points  $i-1$  and  $i+1$  as a Taylor expansion about  $i$  [49; 50]

$$U_{i-1} = U_i - h \frac{dU}{dx} + \frac{h^2}{2} \frac{d^2U}{dx^2} - \frac{h^3}{6} \frac{d^3U}{dx^3} + \frac{h^4}{24} \frac{d^4U}{dx^4} \quad (3.10)$$

and

$$U_{i+1} = U_i + h \frac{dU}{dx} + \frac{h^2}{2} \frac{d^2U}{dx^2} + \frac{h^3}{6} \frac{d^3U}{dx^3} + \frac{h^4}{24} \frac{d^4U}{dx^4} \quad (3.11)$$

where the higher order terms have been assumed negligible. The first derivative can be isolated by subtracting Equation (3.10) from Equation (3.11) and rearranging to obtain

$$\frac{dU}{dx} = \frac{U_{i+1} - U_{i-1}}{2h} - \frac{h^2}{6} \frac{d^3U}{dx^3}. \quad (3.12)$$

The second term in Equation (3.12) is the truncation error term, which for the central difference approximation is second order with respect to the grid separation  $h$ .

The forward difference is obtained by rearranging Equation (3.11) for the first derivative as follows

$$\frac{dU}{dx} = \frac{U_{i+1} - U_i}{h} - \frac{h}{2} \frac{d^2U}{dx^2} - \frac{h^2}{6} \frac{d^3U}{dx^3} - \frac{h^3}{24} \frac{d^4U}{dx^4} \quad (3.13)$$

where the leading error term is  $-\frac{h}{2} \frac{d^2U}{dx^2}$  and linear in  $h$ .

The backward difference can be obtained from equation (3.10) by rearranging as follows

$$\frac{dU}{dx} = \frac{U_i - U_{i-1}}{h} + \frac{h}{2} \frac{d^2U}{dx^2} + \frac{h^2}{6} \frac{d^3U}{dx^3} + \frac{h^3}{24} \frac{d^4U}{dx^4} \quad (3.14)$$

where the leading error term is  $\frac{h}{2} \frac{d^2U}{dx^2}$  and linear in  $h$ .

Since the error term is second order with respect to  $h$  for the central difference method it is clear that it gives the most accurate approximation to the first derivative. For this reason central differences will be used throughout [51].

To calculate the second derivative, Equation (3.10) is added to Equation (3.11) and rearranged to give

$$\frac{d^2U}{dx^2} = \frac{U_{i+1} + U_{i-1} - 2U_i}{h^2} - \frac{h^2}{24} \frac{d^4U}{dx^4}. \quad (3.15)$$

The truncation error for the second derivative is also second order in  $h$ .

Unfortunately many of the changes that occur during an action potential involve fluxes within a few nanometres of the membrane. This means that

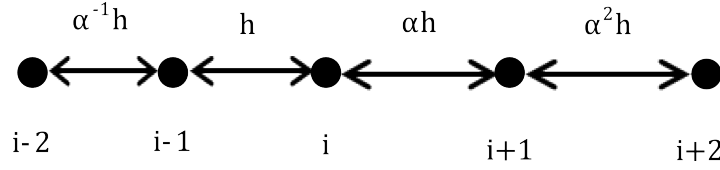


Figure 3.5: Stencil used in central difference approximations on a non uniform grid. The parameter  $\alpha$  determines the degree of non uniformity. The distance between adjacent points is non uniform.

a small grid spacing is required to enable the concentration profiles to be well resolved.

This is an issue because the size of the cell is  $2 \mu\text{m}$  and so a fine grid would involve a very large number of points. Further away from the membrane the changes in concentration profiles are relatively small and it is not necessary to have so many points. This means that a non uniform grid can be used.

When defining the non uniform grid it is important to think about the system being modelled. Regions in the model where one or more properties undergo a rapid change need to be modelled with a finer grid spacing.

The non uniform grid will be defined in a similar way to the one used in [52; 53]. Similar methods are also used in [54]. In its simplest form, a region of constantly spaced grid points with some minimal spacing  $\Delta x_{min}$  is used. This uniform region extends to some switching point  $X_s$ , beyond which the spacing between points increases as follows

$$x_i = x_{i-1} + \gamma x_{i-1}, \quad (3.16)$$

where  $\gamma$  is the grid expansion coefficient. For negative  $i$ , the grid points are defined by  $x_{-i} = -x_i$ .

The use of a non uniform grid means that it is necessary to recalculate the approximations for the derivatives to take into account the unequal spacing between points.

The computational stencil used for the non uniform regions is shown in Figure 3.5. It should be noted here that  $\alpha$  is equivalent to  $1 + \gamma$  or  $1 - \gamma$  depending on whether the grid spacing is increasing to the right or the left.

The central difference approximations are derived in a similar way to those used in the uniform case. First express the values of a function  $U$  at points  $i-1$  and  $i+1$  as a Taylor expansion about  $i$

$$U_{i-1} = U_i - h \frac{dU}{dx} + \frac{h^2}{2} \frac{d^2U}{dx^2} - \frac{h^3}{6} \frac{d^3U}{dx^3} + \frac{h^4}{24} \frac{d^4U}{dx^4} \quad (3.17)$$

and

$$U_{i+1} = U_i + \alpha h \frac{dU}{dx} + \alpha^2 \frac{h^2}{2} \frac{d^2U}{dx^2} + \alpha^3 \frac{h^3}{6} \frac{d^3U}{dx^3} + \alpha^4 \frac{h^4}{24} \frac{d^4U}{dx^4}. \quad (3.18)$$

Taking a weighted sum of Equation (3.17) and Equation (3.18) allows the necessary derivatives to be calculated [55].

$$\begin{aligned} U_{i-1} + AU_{i+1} = U_i(1+A) &+ (-1 + \alpha A)h \frac{dU}{dx} + (1 + \alpha^2 A) \frac{h^2}{2} \frac{d^2U}{dx^2} \\ &+ (-1 + \alpha^3 A) \frac{h^3}{6} \frac{d^3U}{dx^3} + (1 + \alpha^4 A) \frac{h^4}{24} \frac{d^4U}{dx^4}. \end{aligned} \quad (3.19)$$

To isolate the first derivative,  $A$  must be set such that the term proportional to  $\frac{d^2U}{dx^2}$  is eliminated. In this case  $A = -\frac{1}{\alpha^2}$ . Substituting this value for  $A$  into Equation (3.19) and rearranging for  $\frac{dU}{dx}$  gives

$$\begin{aligned} \frac{dU}{dx} = -\frac{\alpha}{h(\alpha-1)}U_{i-1} &+ \frac{1}{\alpha h(\alpha+1)}U_{i+1} + \frac{(\alpha^2-1)}{\alpha h(\alpha+1)}U_i \\ &- \frac{\alpha h^2}{6} \frac{d^3U}{dx^3} + \frac{\alpha h^3(1-\alpha^2)}{24(\alpha+1)} \frac{d^4U}{dx^4} \end{aligned} \quad (3.20)$$

where the fourth term in Equation (3.20) is the leading error term in the first derivative.

A similar procedure allows a finite difference approximation for the second derivative to be calculated. This time  $A$  must be set such that the term proportional to  $\frac{dU}{dx}$  is eliminated. Setting  $A$  to  $\frac{1}{\alpha}$  and rearranging for  $\frac{d^2U}{dx^2}$  gives

$$\begin{aligned} \frac{d^2U}{dx^2} = -\frac{2}{h^2(1+\alpha)}U_{i-1} &+ \frac{2}{\alpha h^2(\alpha+1)}U_{i+1} - \frac{2}{\alpha h^2}U_i \\ &+ \frac{h(1-\alpha^2)}{6(1+\alpha)} \frac{d^3U}{dx^3} - \frac{h^2(1+\alpha^3)}{24(1+\alpha)} \frac{d^4U}{dx^4}. \end{aligned} \quad (3.21)$$

The leading error term in Equation (3.21) is only first order in  $h$ . This is a consequence of the non uniform grid, causing imperfect cancellation of terms.

As expected, setting  $\alpha = 1$  in equations (3.20) and (3.21) yields the familiar results for the uniform grid, (3.12) and (3.15).

The exact nature of the grid depends on the system being modelled and will be discussed in more detail in the relevant research chapters.

#### 3.4.1 Numerical Errors and computational performance

The leading error terms, also known as the truncation error, associated with the finite difference approximations on a nonuniform grid are a key source of error. They are proportional to the minimum grid spacing  $h$ .

This implies that we can reduce the error by reducing the minimum grid spacing, which is of course correct up to a point. Beyond a certain point the round off errors caused by the precision of the numbers stored in the computer will become the limiting factor (and can actually lead to dramatic increases in the error with further reductions in  $h$ ).

A simple indication of this can be found by calculating the derivative of a model tanh function (similar to the ones used to set up the initial concentration profiles) both analytically and numerically. Doing this for a variety of grid sizes allows the relative error to be determined for various grids. The function used for these tests is defined as follows:

$$y = 5 + \tanh(ax) \tag{3.22}$$

for which the first derivative is

$$\frac{dy}{dx} = a(1 - \tanh^2(ax)) \tag{3.23}$$

The parameter  $a$  determines the steepness of the tanh function with larger  $a$  values giving rise to steeper functions. This means that large  $a$  values approximate the concentration profile during the early stages of the simulation, with smaller  $a$  values being representative of the later stages.

Figure 3.6 shows that for grid sizes below a certain point, the relative error starts to increase. This is due to the rounding error becoming significant and offsetting the reduction in the truncation error term.

These problems are most likely to occur where there are sharp changes in a quantity such as the tanh functions used to model the initial concentration profiles.

This could be reduced to an extent by using more digits in calculations, although this leads to a large increase in computational time. Ultimately it was found to be unnecessary to increase the numerical precision and suitably accurate results could be obtained using double precision in MATLAB.

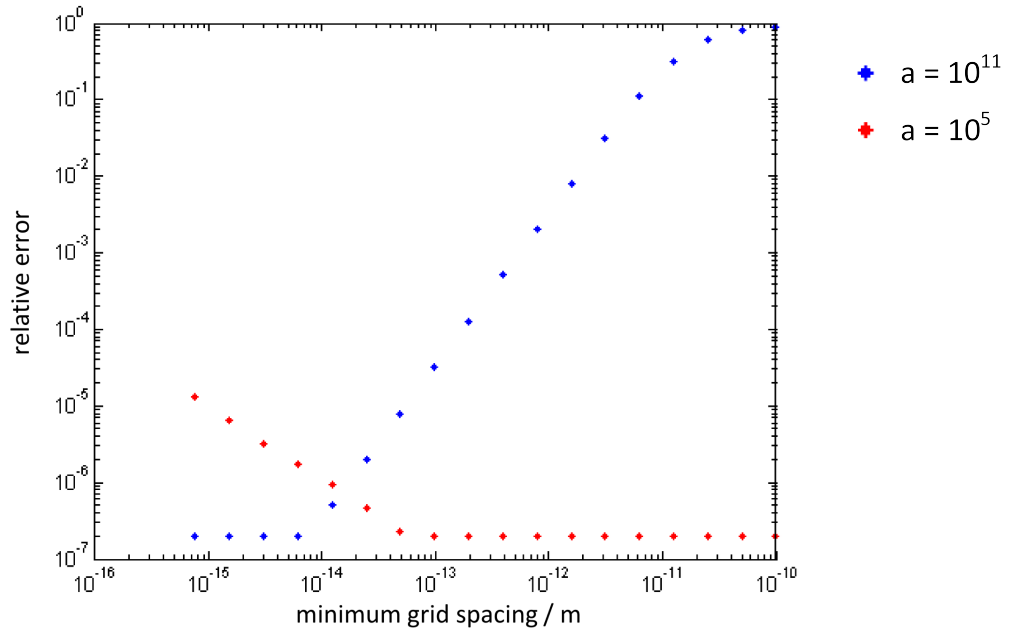


Figure 3.6: Relative error in the first derivative of the tanh function against minimum grid spacing. As expected the error reduces as the grid spacing is decreased, but eventually roundoff errors dominate.

There is always a balancing act with numerical simulations trying to get the best results as quickly as possible. One of the reasons for using the nonuniform grid was that it provided a good balance of accuracy and speed.

The code for dealing with a single membrane is the fastest as it has the simplest layered structure. It simulates an action potential (about 5ms of data) in 32 minutes. Without the nonuniform grid it is unlikely that it would run in any reasonable time.

### 3.5 The Newton Raphson Method

The coupled transport and Poisson equations to be solved are

$$\begin{aligned} \frac{\partial c_{Na}}{\partial t} = & \frac{\partial D_{Na}}{\partial x} \left( \frac{\partial c_{Na}}{\partial x} + \frac{z_{Na}F}{RT} c_{Na} \frac{\partial \theta}{\partial x} \right) \\ & + D_{Na} \left( \frac{\partial^2 c_{Na}}{\partial x^2} + \frac{z_{Na}F}{RT} \frac{\partial c_{Na}}{\partial x} \frac{\partial \theta}{\partial x} + \frac{z_{Na}F}{RT} c_{Na} \left( -\frac{\rho}{\epsilon \epsilon_0} - \frac{1}{\epsilon} \frac{\partial \epsilon}{\partial x} \frac{\partial \theta}{\partial x} \right) \right), \end{aligned} \quad (3.24)$$

$$\begin{aligned} \frac{\partial c_K}{\partial t} &= \frac{\partial D_K}{\partial x} \left( \frac{\partial c_K}{\partial x} + \frac{z_K F}{RT} c_K \frac{\partial \theta}{\partial x} \right) \\ &+ D_K \left( \frac{\partial^2 c_K}{\partial x^2} + \frac{z_K F}{RT} \frac{\partial c_K}{\partial x} \frac{\partial \theta}{\partial x} + \frac{z_K F}{RT} c_K \left( -\frac{\rho}{\epsilon \epsilon_0} - \frac{1}{\epsilon} \frac{\partial \epsilon}{\partial x} \frac{\partial \theta}{\partial x} \right) \right), \end{aligned} \quad (3.25)$$

$$\begin{aligned} \frac{\partial c_{Cl}}{\partial t} &= \frac{\partial D_{Cl}}{\partial x} \left( \frac{\partial c_{Cl}}{\partial x} + \frac{z_{Cl} F}{RT} c_{Cl} \frac{\partial \theta}{\partial x} \right) \\ &+ D_{Cl} \left( \frac{\partial^2 c_{Cl}}{\partial x^2} + \frac{z_{Cl} F}{RT} \frac{\partial c_{Cl}}{\partial x} \frac{\partial \theta}{\partial x} + \frac{z_{Cl} F}{RT} c_{Cl} \left( -\frac{\rho}{\epsilon \epsilon_0} - \frac{1}{\epsilon} \frac{\partial \epsilon}{\partial x} \frac{\partial \theta}{\partial x} \right) \right) \end{aligned} \quad (3.26)$$

and

$$\epsilon \frac{\partial^2 \theta}{\partial x^2} + \frac{\partial \epsilon}{\partial x} \frac{\partial \theta}{\partial x} + \sum_i z_i c_i = 0. \quad (3.27)$$

These equations must be solved at all grid points so if there are  $N$  grid points, there will be  $4N$  equations to solve. The finite difference formulae, equations (3.20) and (3.21) are used to approximate the values of any derivatives at all points on the grid.

Initially the Crank - Nicolson method was used, but this proved to have difficulties due to the wide range of distances between grid points. The Newton Raphson method has been used in similar electrochemistry work [52] and used to obtain results relating to ionic solutions separated by an infinitesimal membrane. It is an iterative method useful for solving systems of non-linear equations and is described below. First the equations are written in homogeneous form

$$f(x) = 0. \quad (3.28)$$

In the simple case with just one equation in one variable, the iterations are calculated using the Taylor series about some trial solution  $x_0$

$$f(x) \approx f(x_0) + (x - x_0) f'(x_0) = 0. \quad (3.29)$$

Rearranging equation (3.29) for  $x$  gives the formula for the iterations

$$x_1 = x_0 - \frac{f(x_0)}{f'(x_0)}. \quad (3.30)$$

For functions of multiple variables, equation (3.29) is modified as follows

$$f(\mathbf{x}) \approx f(\mathbf{x}_0) + \sum_n (x_n - x_{n,0}) \frac{\partial f(\mathbf{x}_0)}{\partial x_n} = 0 \quad (3.31)$$

$$\begin{bmatrix}
 0 & \dots & \frac{\partial f_4(i-1)+1}{\partial c_{Na,i-1}} & \frac{\partial f_4(i-1)+1}{\partial \theta_{i-1}} & \frac{\partial f_4(i-1)+1}{\partial c_{K,i-1}} & \frac{\partial f_4(i-1)+1}{\partial c_{Cl,i-1}} & \frac{\partial f_4(i-1)+1}{\partial c_{Na,i}} & \frac{\partial f_4(i-1)+1}{\partial \theta_i} & \frac{\partial f_4(i-1)+1}{\partial c_{K,i}} & \frac{\partial f_4(i-1)+1}{\partial c_{Cl,i}} & \frac{\partial f_4(i-1)+1}{\partial c_{Na,i+1}} & \frac{\partial f_4(i-1)+1}{\partial \theta_{i+1}} & \frac{\partial f_4(i-1)+1}{\partial c_{K,i+1}} & \frac{\partial f_4(i-1)+1}{\partial c_{Cl,i+1}} & \dots & 0 \\
 0 & \dots & \frac{\partial f_4(i-1)+2}{\partial c_{Na,i-1}} & \frac{\partial f_4(i-1)+2}{\partial \theta_{i-1}} & \frac{\partial f_4(i-1)+2}{\partial c_{K,i-1}} & \frac{\partial f_4(i-1)+2}{\partial c_{Cl,i-1}} & \frac{\partial f_4(i-1)+2}{\partial c_{Na,i}} & \frac{\partial f_4(i-1)+2}{\partial \theta_i} & \frac{\partial f_4(i-1)+2}{\partial c_{K,i}} & \frac{\partial f_4(i-1)+2}{\partial c_{Cl,i}} & \frac{\partial f_4(i-1)+2}{\partial c_{Na,i+1}} & \frac{\partial f_4(i-1)+2}{\partial \theta_{i+1}} & \frac{\partial f_4(i-1)+2}{\partial c_{K,i+1}} & \frac{\partial f_4(i-1)+2}{\partial c_{Cl,i+1}} & \dots & 0 \\
 0 & \dots & \frac{\partial f_4(i-1)+3}{\partial c_{Na,i-1}} & \frac{\partial f_4(i-1)+3}{\partial \theta_{i-1}} & \frac{\partial f_4(i-1)+3}{\partial c_{K,i-1}} & \frac{\partial f_4(i-1)+3}{\partial c_{Cl,i-1}} & \frac{\partial f_4(i-1)+3}{\partial c_{Na,i}} & \frac{\partial f_4(i-1)+3}{\partial \theta_i} & \frac{\partial f_4(i-1)+3}{\partial c_{K,i}} & \frac{\partial f_4(i-1)+3}{\partial c_{Cl,i}} & \frac{\partial f_4(i-1)+3}{\partial c_{Na,i+1}} & \frac{\partial f_4(i-1)+3}{\partial \theta_{i+1}} & \frac{\partial f_4(i-1)+3}{\partial c_{K,i+1}} & \frac{\partial f_4(i-1)+3}{\partial c_{Cl,i+1}} & \dots & 0 \\
 0 & \dots & \frac{\partial f_4(i-1)+4}{\partial c_{Na,i-1}} & \frac{\partial f_4(i-1)+4}{\partial \theta_{i-1}} & \frac{\partial f_4(i-1)+4}{\partial c_{K,i-1}} & \frac{\partial f_4(i-1)+4}{\partial c_{Cl,i-1}} & \frac{\partial f_4(i-1)+4}{\partial c_{Na,i}} & \frac{\partial f_4(i-1)+4}{\partial \theta_i} & \frac{\partial f_4(i-1)+4}{\partial c_{K,i}} & \frac{\partial f_4(i-1)+4}{\partial c_{Cl,i}} & \frac{\partial f_4(i-1)+4}{\partial c_{Na,i+1}} & \frac{\partial f_4(i-1)+4}{\partial \theta_{i+1}} & \frac{\partial f_4(i-1)+4}{\partial c_{K,i+1}} & \frac{\partial f_4(i-1)+4}{\partial c_{Cl,i+1}} & \dots & 0
 \end{bmatrix}$$

Figure 3.7: Four rows of the Jacobian matrix, showing the elements which are non zero. Each row corresponds to one of the 4 equations at a grid point  $i$  and is associated with one element in the column vector  $f$ .

and defining the difference between the trial solution and iteration result as  $u_n = (x_n - x_{n,0})$  allows equation (3.31) to be rewritten as

$$\sum_n u_n \frac{\partial f(\mathbf{x}_0)}{\partial x_n} = -f(\mathbf{x}_0). \quad (3.32)$$

Since there are  $n$  equations in  $n$  variables equation (3.32) becomes

$$\sum_n u_n \frac{\partial f_m(\mathbf{x}_0)}{\partial x_n} = -f(\mathbf{x}_0). \quad (3.33)$$

Defining a Jacobian matrix with elements given by

$$J_{mn} = \frac{\partial f_m}{\partial x_n} \quad (3.34)$$

allows equation (3.32) to be written in a matrix form

$$\mathbf{J}\mathbf{u} = -f(\mathbf{x}_0). \quad (3.35)$$

If the equations are ordered correctly, the matrix  $J$  in Equation (3.35) has only 12 non zero diagonals, which makes it somewhat easier to solve. If there are  $N$  grid points, there are  $4n$  equations to solve, three representing the evolution of the concentration profiles and one describing the evolution of the potential. Consequently there are 4 rows within the matrix equation for each point on the grid and the only non zero derivatives in the Jacobian matrix are those relating to the variables at the point under consideration and also the adjacent two points.

By arranging the equations as indicated in Figure 3.7 the non zero elements fall on a set of 12 diagonals.

At the end of each iteration the solution vector  $\mathbf{u}$  is added to the trial solution  $\mathbf{x}_0$ . This process is repeated until the desired tolerance is reached, at which point the final vector  $\mathbf{x}$  becomes the trial solution for the following

timestep. The potential across the membrane is calculated at the end of each time step, then used to recalculate the Hodgkin Huxley gating variables ready for the next time step using equations (2.5), (2.10), and (2.6).

### 3.6 Validation

Given that this is a numerical piece of work, it is important to consider whether the results are valid and meaningful. In order to do this, it was necessary to experiment with various grid spacings and time step sizes to check that the simulations were converging well. Another useful check was whether the system reproduced the known neural behaviours accurately. To be considered valid the model would be expected to fully explain the following behaviours: action potentials, resting potentials and sub threshold responses. The results obtained will be compared with known results from the Hodgkin Huxley model. If the model got stuck in a local minima it would be unlikely to reproduce the expected behaviours outlined above. A more detailed look at the validity of the results will be given in the discussion sections of chapters 4, 5 and 6.

# Chapter 4

## Single Membrane

In order to model the behaviour of the cell it is necessary to be able to implement Hodgkin Huxley type behaviour within the membrane. In this chapter, we describe the implementation in the case of a single membrane.

### 4.1 Outline of the Single Membrane Model

The system consists of semi infinite extra and intra cellular media separated by a membrane. The initial ionic composition of the two media is shown in Figure 4.1. There is a high concentration of sodium outside the cell and a high concentration of potassium inside the cell. The initial values chosen are based on those quoted in various sources [2; 41] but adjusted due to certain minor ions not being considered and to satisfy the need for electroneutrality.

Initially the concentration profiles are smoothly connected through the membrane using tanh functions as described in section 3.3. The membrane is a region of space approximately 5 nm thick. Ion movement through the membrane is controlled by voltage gated ion channels, the effects of which are modelled by a severely reduced diffusion coefficient within the membrane.

The Hodgkin Huxley model which describes the ion channels is discussed in section 2.2. The relation of the Hodgkin Huxley model to the diffusion coefficient is discussed in more detail in section 3.2. Relating the Hodgkin Huxley behaviour to the diffusion coefficient allows the drift-diffusion and Poisson equations to be applied in all three regions of the model. This is called the drift diffusion enhanced Hodgkin Huxley model.

## 4.1 Outline of the Single Membrane Model

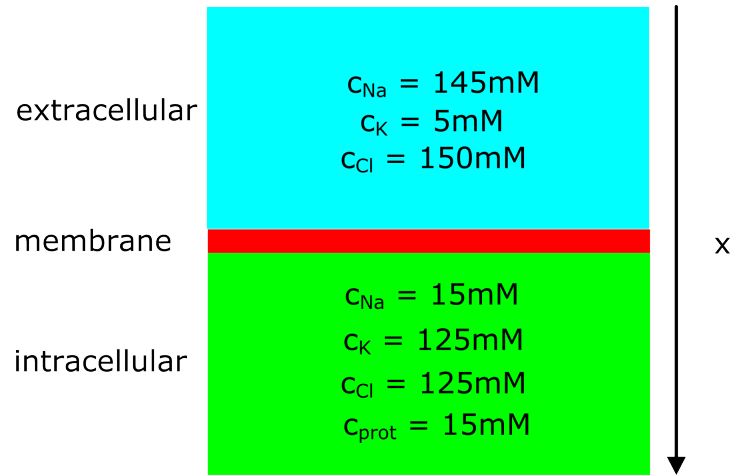


Figure 4.1: Schematic diagram of the layers used in the single membrane model. Within the membrane the concentration profiles smoothly transition from extracellular values to the intracellular values using tanh functions (see Figure 4.2).

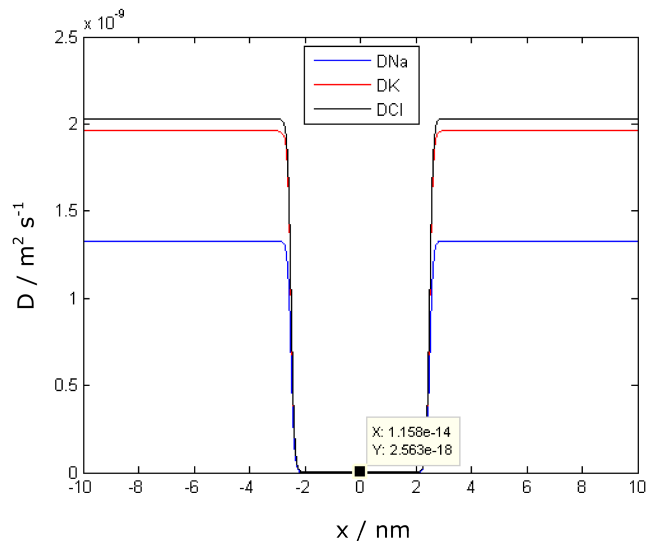


Figure 4.2: Diffusion coefficient profile showing how tanh curves are used to make a smoothly evolving diffusion coefficient profile through the membrane. Diffusion coefficients are shown for sodium (blue curve), potassium (red curve) and chloride (black curve) ions

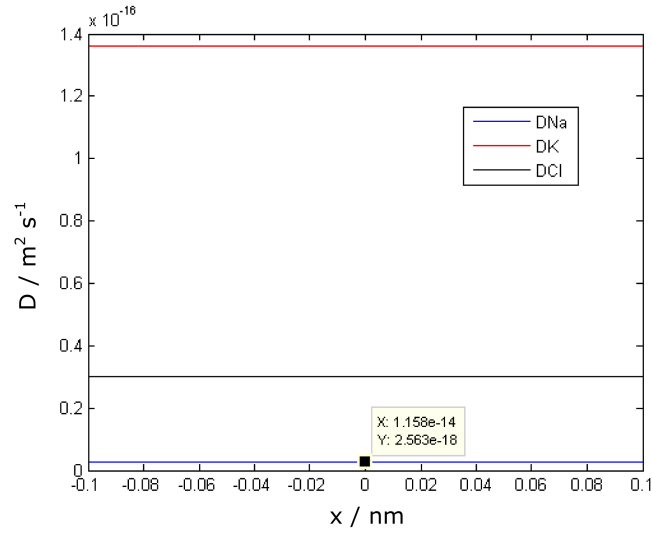


Figure 4.3: Close up of diffusion coefficient profile within the membrane region. At rest the sodium ion channels are mostly closed and so the diffusion coefficient is considerably lower than for the other ion species. The blue, red and black curves correspond to sodium, potassium and chloride ions respectively. It should also be noted that values for the diffusion coefficient are considerably smaller than those within the intra and extracellular media. This is because the membrane significantly reduces the ion flow between the intracellular and extracellular regions. The decrease in the diffusion coefficient within the membrane can clearly be seen by comparing with Figure 4.2.

Figure 4.2 shows the diffusion coefficient profile for the three different ion species. All ions have much smaller diffusion coefficients inside the membrane. As ion channels open, the diffusion coefficient within the membrane increases allowing more of a particular ion type through the membrane.

A close up of the diffusion coefficient profiles inside the membrane shows the difference in the ion channels initial states, as can be seen in Figure 4.3. At rest the sodium ion channels are almost completely closed and so the diffusion coefficient for sodium within the membrane is up to two orders of magnitude lower than that for potassium or chloride ions.

To solve the equations a non-uniform grid is used, as discussed in section 3.4. This is defined in such a way that there is a region of closely spaced points, corresponding to the membrane and its immediate surroundings. This is where the diffusion coefficient gradient and the concentration gradients are highest and also where most of the ion movement occurs in the

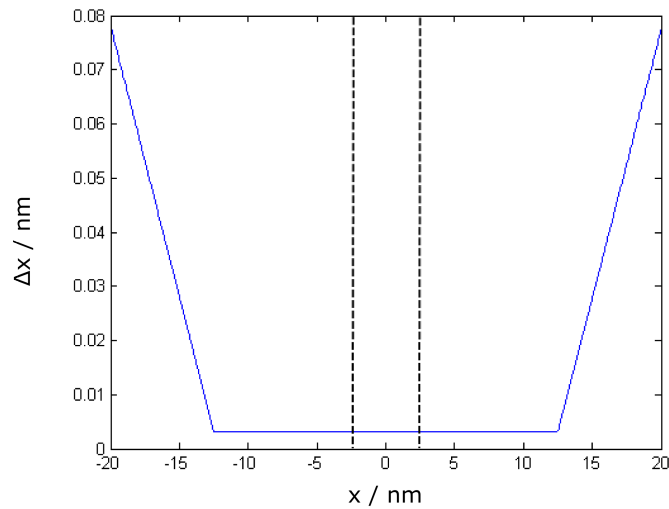


Figure 4.4: Plot showing how the grid spacing  $\Delta x$  varies with position. A small grid spacing is used for the membrane and its surroundings as this is where the gradients are high and most of the ion movement takes place. Further away from the membrane the spacing is allowed to increase. The membrane region is indicated by the dashed lines. The region of fine grid spacing extends beyond the membrane to allow the bulk of the diffusion that occurs close to the membrane to be modelled accurately. Axes are restricted to show a limited portion of space for clarity.

model.

Outside this region the spacing between points is allowed to increase as there is less ion movement far from the membrane.

Figure 4.4 shows how the grid spacing varies with position. The axes are restricted to show only the membrane and the region close to it. The membrane region is indicated by dashed lines, but the region of fine grid spacing extends beyond this to allow the diffusion close to the membrane to be modelled accurately. If the full domain was shown, the region of closely spaced points would not clearly be visible.

## 4.2 Single Membrane Results

An important test of the validity of the model is whether it exhibits the behaviours of real neurons. There is a range of behaviours which would be expected to be reproduced by the model and it is these characteristics which will be the focus of this section.

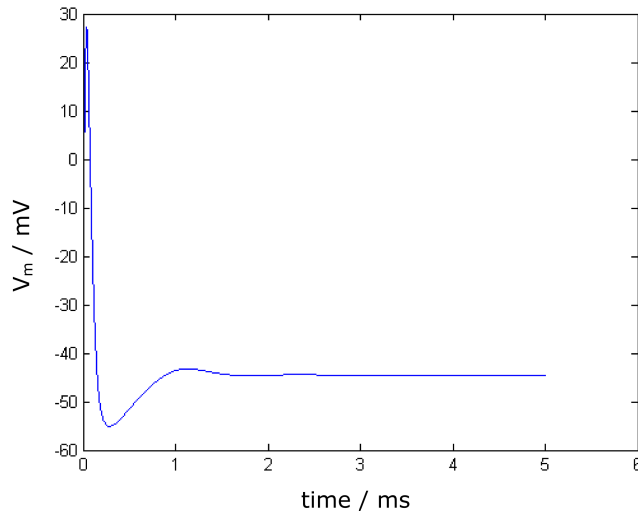


Figure 4.5: The system evolves to a resting potential. This resting state is determined by a weighted average of the Nernst potentials for all the ions with the ability to cross the membrane. The weightings are determined by the resting conductances for the ions. The initial spike is due to the initial conditions being an unstable point.

Firstly the case of no stimulation is considered. If there is no stimulation, the system evolves to a resting potential and remains in that state until stimulated. The spike in potential within the first 1 ms, shown in Figure 4.5, is the result of the evolution from the initial state. The system is initialised in a charge neutral state, so the potential difference across the membrane is zero. This is an unstable point in the Hodgkin Huxley model as a zero membrane potential is far from the resting state (discussed in more detail in section 2.2). This means that the gating equations (Equations (2.5), (2.6) and (2.10)) cause the ion channels to open and the system evolves through an action potential. The later part of the graph shows how the system then evolves to a resting state in which the membrane potential is constant.

The resting state is determined by a weighted average of the Nernst potentials for each ionic species, as discussed in section 2.2.2. The resting conductances are used to give the relative weights. If only one ion type was present, the resting potential would be equal to its Nernst potential.

The timescale is determined by the gating variables and the rate functions associated with the gating equations. These rate functions exhibit a temperature dependence. The form of these functions was experimentally determined by Hodgkin and Huxley, as discussed in section 2.2.2.

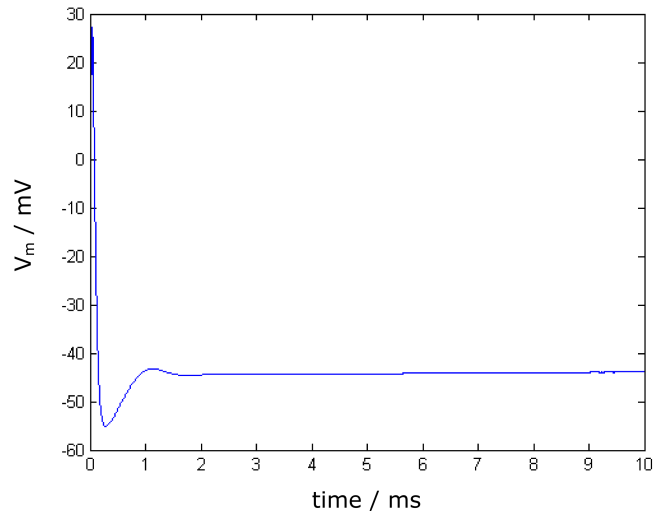


Figure 4.6: Evolution of the system’s membrane potential,  $V_m$ , to its resting potential at  $T = 310\text{K}$ . After 1.5 ms the system is at rest and undergoes no further significant change.

The capacitance of the membrane also affects the timescale of the membrane dynamics, this is itself dependent on the permittivity and thickness of the membrane.

The effect of temperature on the membrane dynamics can be seen clearly by comparing Figure 4.6, which shows the dynamic return to rest from a zero membrane potential state at  $T = 310\text{K}$ , with Figure 4.7, which shows the same but for  $T = 279\text{K}$ . The membrane returns to its resting state much slower at the lower temperature. This is because the chemical rate constants in the Hodgkin Huxley model take on different values with different temperatures. This causes the change in the gating variables (and hence the opening and closing of ion channels) to occur at a different rate depending on the temperature. The fast rate corresponds with the human body temperature.

The resting potential is an important feature of neurons and so it is of great significance that this behaviour is observed in the model. It is, however, the active behaviour of neurons which is of particular interest. To study this it is necessary to provide a stimulus to the model.

Stimuli that raise the membrane potential are known as depolarising stimuli. If a sufficient stimulus is applied, the membrane is sufficiently depolarised that a positive feedback effect occurs, giving rise to an action

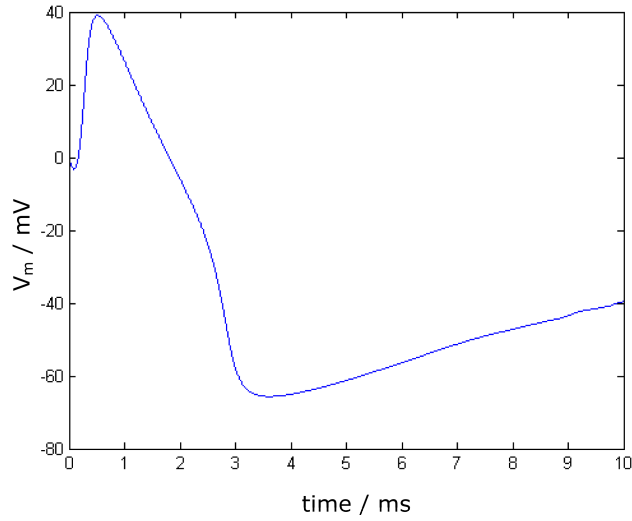


Figure 4.7: Evolution to resting potential at  $T = 279\text{K}$ . This is much slower as the system has not reached rest even after 10ms.

potential. This is because the raised membrane potential triggers the opening of sodium ion channels once a threshold is reached. This causes a rapid rise in membrane potential as sodium enters the cell. The potassium channels then open allowing potassium to leave the cell, which has the effect of reducing the membrane potential. It is noticeable that there is a period of time during which the membrane potential is more negative than the resting potential. This is known as hyperpolarisation and is due to the fact that the potassium channels are slower to close and so more potassium ions can leave the cell.

It is useful to compare the results of the Drift Diffusion Hodgkin Huxley model with those of the classic Hodgkin Huxley model, as they would be expected to be in good general agreement.

Figure 4.9 shows a comparison between the Hodgkin Huxley (HH) model and the drift diffusion enhanced Hodgkin Huxley (DDHH) model during the evolution towards the resting potential. It can be seen that the two models are in good qualitative agreement, but there are some small quantitative differences. These are likely due to the fact that the Hodgkin Huxley model does not have smoothly evolving concentration profiles through the membrane.

The tanh curves controlling the diffusion coefficient profiles within the membrane may result in a smaller effective thickness of the membrane as

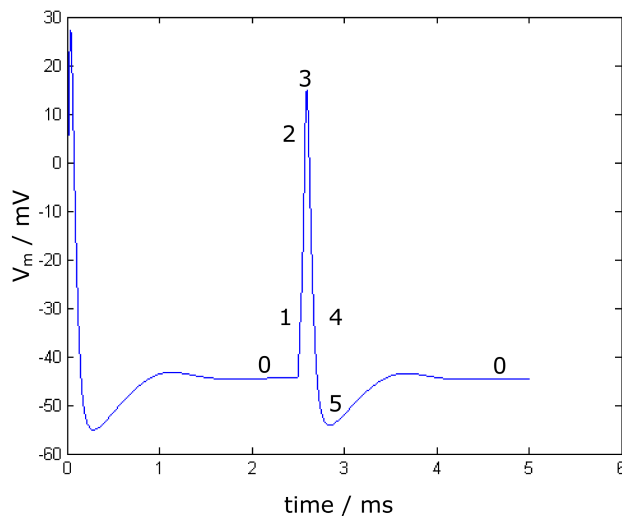


Figure 4.8: An action potential, showing the rapid rise and fall in membrane potential,  $V_m$ , caused by the opening of ion channels. Numbers indicate key features of the action potential. The resting phase is indicated by 0 both before and after the action potential. The initial depolarisation is indicated by position 1. This takes the membrane potential above and beyond the threshold. Point 2 is known as the overshoot, which is where the potential becomes positive. Position 3 is the peak, the maximum potential reached. The repolarisation phase is indicated by position 4, where the potential starts to drop back towards the resting value. The region marked by point 5 is the hyperpolarising afterpotential. This is a period for which the membrane potential is more negative than its resting state. The action potential is discussed in more detail in section 2.2

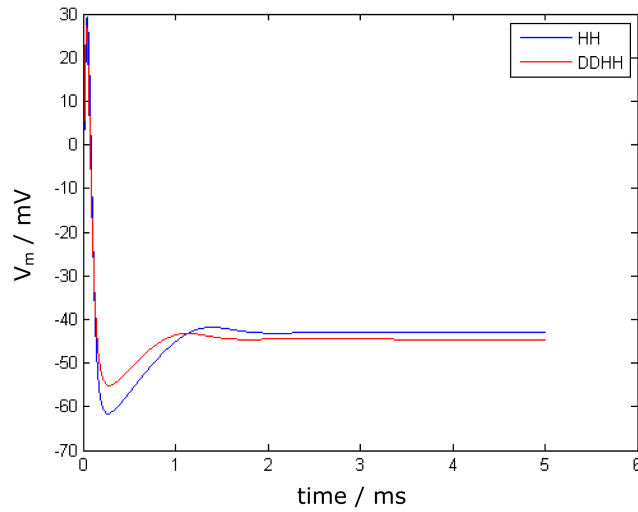


Figure 4.9: The Drift Diffusion Hodgkin Huxley model (red curve) is in good agreement with the Hodgkin Huxley model. There are some quantitative differences with the dynamics, but these are most likely due to the smoothing of the tanh functions, which alters the effective width of the membrane.

indicated in some of the following figures.

Similar quantitative differences are observed when a stimulation is applied resulting in an action potential, as can be seen in Figure 4.10. The difference between the Hodgkin Huxley and the Drift Diffusion Hodgkin Huxley model results appears to be, at least in part, due to the use of the tanh curves to set up the diffusion coefficient profile of the membrane. By reducing the value of the parameter  $d$  in Equation (3.9), it is seen that the results more closely approach the Hodgkin Huxley model. This makes sense, as the reduction in  $d$  results in a sharper more rapid transition from the large diffusion coefficient within the media, to the small heavily restrictive diffusion coefficient within the membrane.

To gain a better understanding of what is going on during an action potential, it is useful to examine the behaviour of the ion channels.

This can be illustrated by plotting the gating variables and the conductances. The gating variables are unitless parameters ranging from 0 to 1, with 0 representing fully closed states and 1 representing fully open states. Since within any patch of membrane there are a large number of ion channels, the gating parameters should be viewed as the probability of the associated gates being open. Figure 4.11 shows how the gating variables

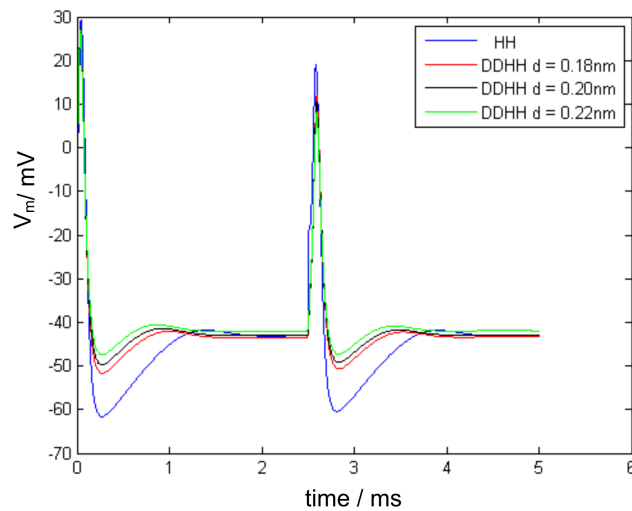


Figure 4.10: The Drift Diffusion Hodgkin Huxley model is in good agreement with the Hodgkin Huxley model. There are some differences with the dynamics, but these are most likely due to the smoothing of the tanh functions. By changing the value of the parameter  $d$  in Equation (3.9) which defines the tanh curves, the results start to more closely agree with the Hodgkin Huxley model. Here the response to a stimulus at time  $t = 2.5$  ms is shown. The first initial spike after  $t = 0$  ms is due to evolution from the unstable point used as the initial conditions. The blue curve shows the results from the Hodgkin Huxley model, the red, black and green curves show the results of the drift diffusion Hodgkin Huxley model using tanh curves with different values for the parameter  $d$ .

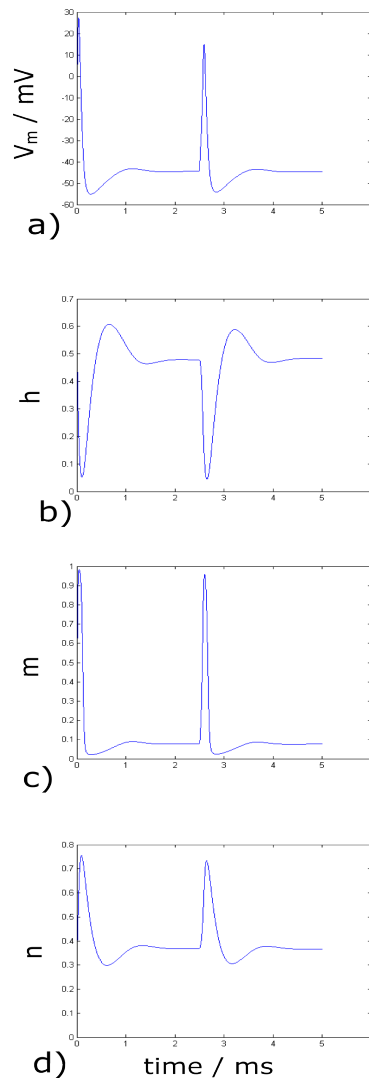


Figure 4.11: a) An action potential for reference. b) The  $h$  gate. This is known as the inactivation gate for sodium. It is different to the other two gates as it is open at rest and closed during periods of depolarisation.  $h$  appears as a linear term in the equation for the sodium conductance. c) The  $m$  gate. This is the sodium activation gate. It opens during depolarisation and is closed at rest.  $m$  appears as a cubic term in the equation for the sodium conductance. d) The  $n$  gate. This is the potassium activation gate. It is only partially closed at rest, but opens more during periods of depolarisation.  $n$  appears to the fourth power in the equation for potassium conductance. There is no inactivation gate for potassium.

behave during an action potential and the subsequent evolution to rest. The  $h$  gate, shown in Figure 4.11b is the sodium inactivation gate and is open during the resting phase and closed during depolarisation. Since  $h$  is quite slow to open after the action potential, there is a period during which subsequent stimulations will not trigger an action potential. This is called the refractory period. The  $m$  gate is the sodium activation gate shown in Figure 4.11c. This is closed when the membrane is at rest but opens when depolarised. The potassium activation gate  $n$  behaves similarly, except that it is partially open during rest as shown in Figure 4.11d.

Although there is a clear picture of the behaviour of the gating variables, the power law relationships which determine the conductances mean it is not immediately apparent how these variables affect the membrane conductance for the various ions.

Figure 4.12b shows the variation of the sodium conductance during an action potential. Comparing this with the reference action potential (Figure 4.12a) shows the positive feedback effect in action. The initial stimulus raises the membrane potential, this then causes an increase in the sodium conductance, which further increases the potential. Looking at the potassium conductance shown in Figure 4.12c, it is clear that the dynamics for potassium are slower. This means that potassium is able to leave the cell after the sodium channels have closed, resulting in hyperpolarisation, where the membrane potential becomes more negative than the resting potential state.

The chloride conductance is just a constant value which is considerably smaller than the sodium and potassium conductances and is shown in Figure 4.12d for completeness.

The model is able to respond to further stimuli as can be seen by applying repeated stimuli. If after an action potential (and subsequent refractory period) a further stimulus is applied it is possible to "fire" the neuron multiple times. This can be seen in Figure 4.13a. The stimuli are applied in the form of a temporary increase in the membrane diffusion coefficient for sodium as shown in Figure 4.13b. This behaviour is observed within real neurons, so is an important test of the model's validity.

It is also necessary that the model has a threshold, so that stimuli below the threshold do not trigger an action potential. To test this, the strength of the stimulus was varied. This was achieved by changing the amount

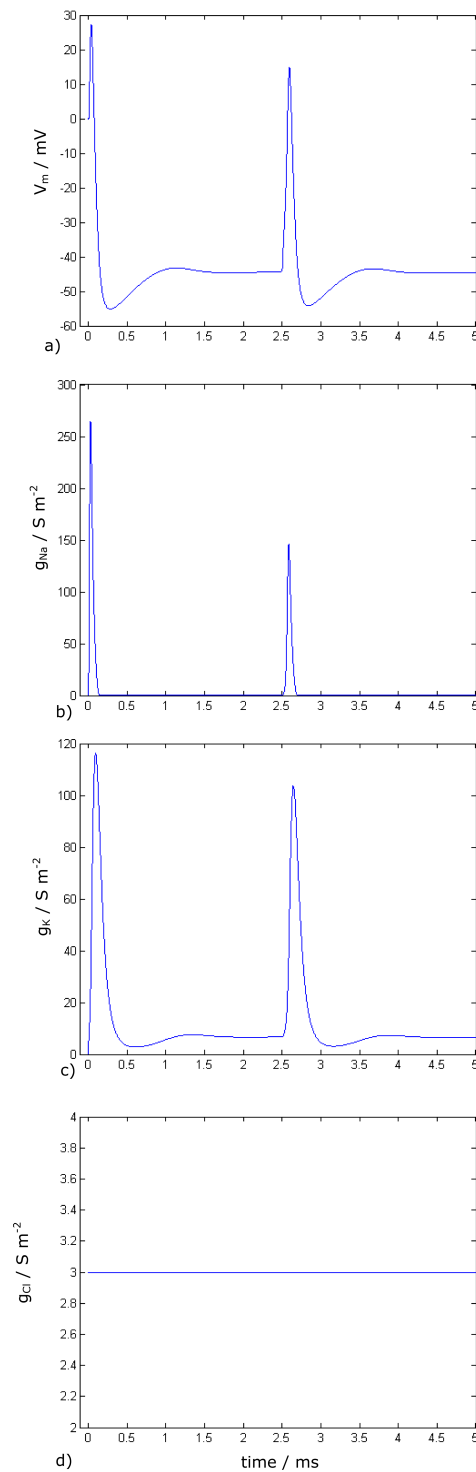


Figure 4.12: a) An action potential shown versus time for reference. b) Sodium conductance. The sharp rise allows an influx of sodium into the cell causing depolarisation of the membrane. c) Potassium conductance. d) Chloride conductance.

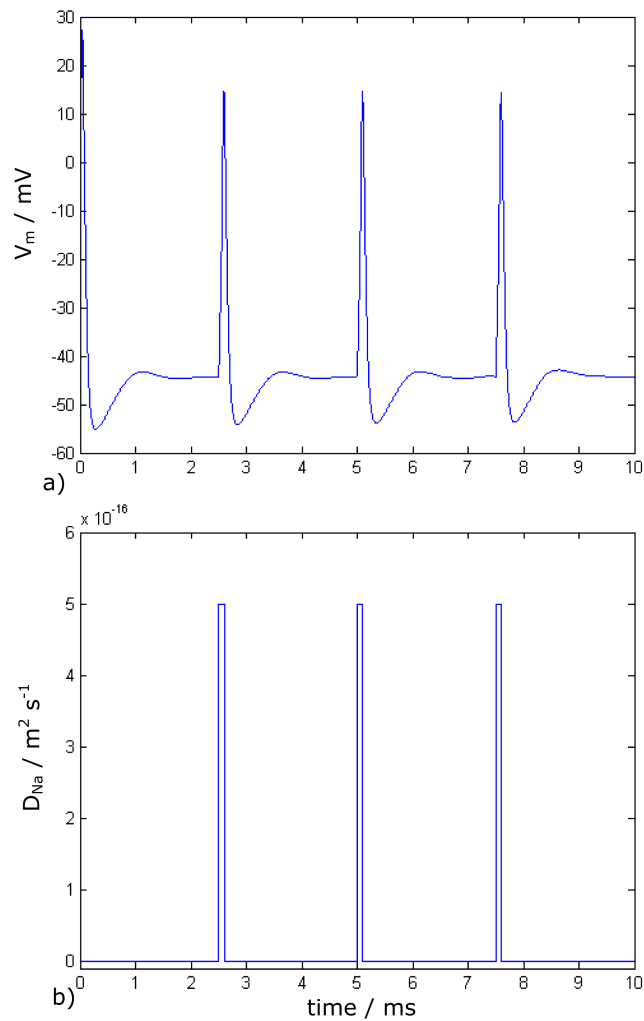


Figure 4.13: a) Multiple action potentials caused by repeated stimuli. It is important that the model is able to cope with multiple stimulations, since real neurons are able to be repeatedly stimulated, provided the following stimulus is after the refractory period. b) Diffusion coefficient stimuli used to initiate the action potentials.

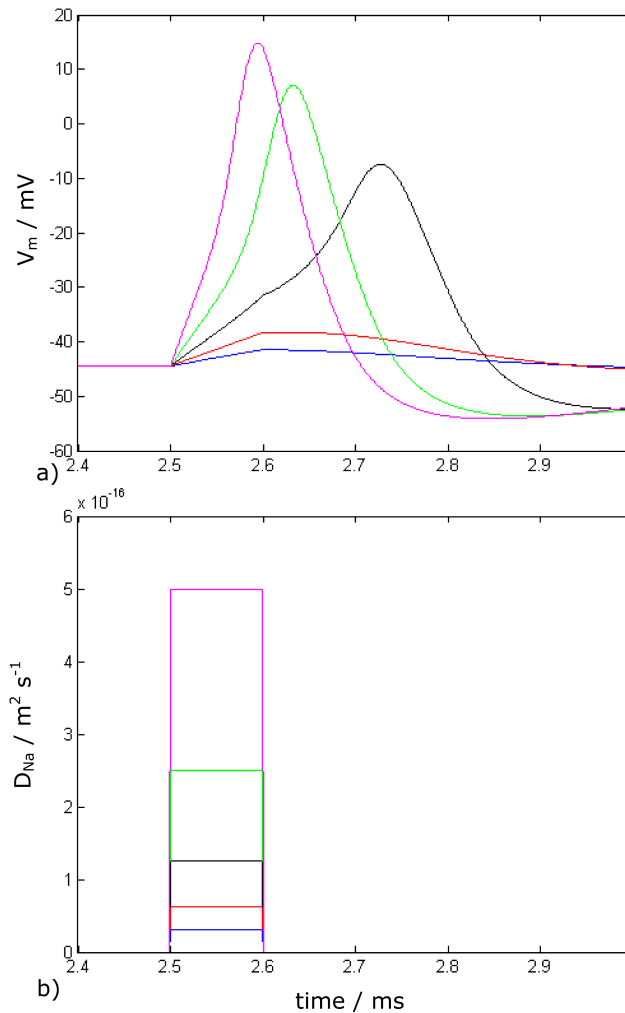


Figure 4.14: a) Responses to the different strength stimuli colour-coded and shown in b). The weakest two stimuli are below threshold and do not trigger action potential. There is still a small deviation from the resting state which is gradually restored. The stronger stimuli do lead to the positive feedback effect that causes an action potential. It is noticeable that the stronger stimuli reach the threshold quicker, so the action potential arrives slightly earlier for the larger stimuli. Stimuli shown in b). The nature of the stimuli is a step increase in the diffusion coefficient of sodium within the membrane. The step decrease has minimal effect as by this time the Hodgkin Huxley gating variables have increased the sodium diffusion coefficient to such a degree that the initial applied step is negligible.

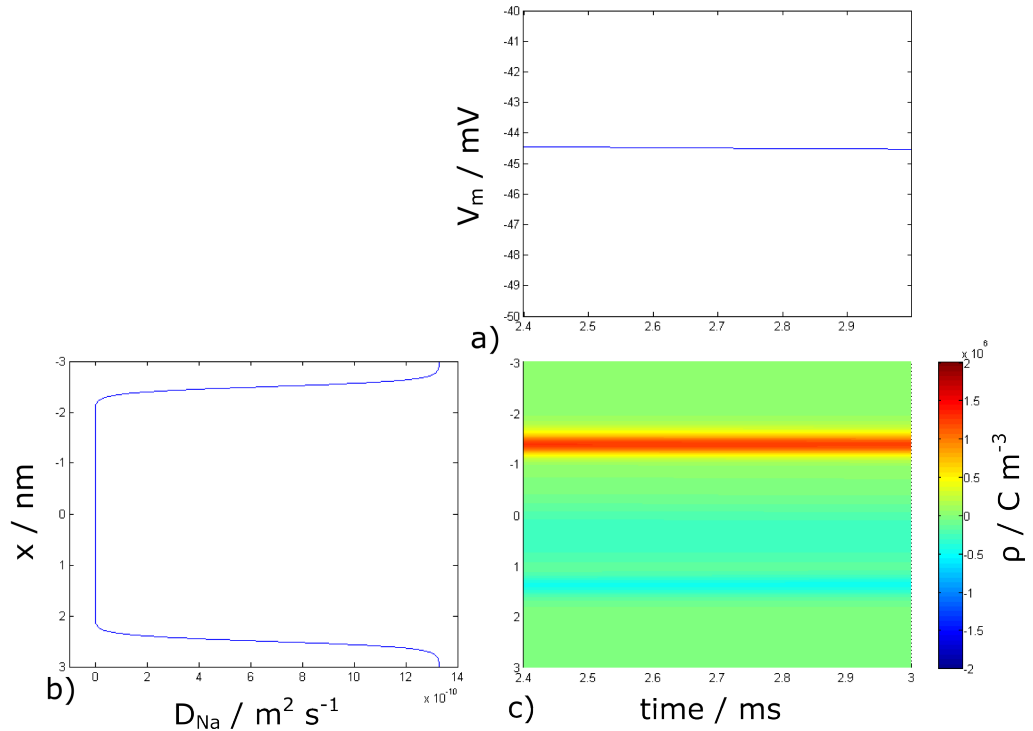


Figure 4.15: a) The resting potential state. b) Diffusion coefficient profile for sodium, indicates the position of the membrane. Due to the extreme variation of the diffusion coefficient, the effective thickness of the membrane is slightly smaller than expected c) Charge density profile when no stimulation is provided. There is some charge build up at the membrane due to the uneven distribution of different ion types. It is this charge build up that gives rise to the non zero resting state.

by which the diffusion coefficient within the membrane for sodium was increased during the stimulation period as shown in 4.14b.

Figure 4.14a shows the results of different strength stimuli. The weakest two of these fail to trigger the positive feedback effect that leads to an action potential and are therefore sub threshold stimuli. The three larger pulses do lead to action potentials as they cause sufficient membrane depolarisation to trigger the positive feedback effect.

The simulations also allow a spatio temporal profile to be calculated for many of the variables of interest. This is a useful feature of the drift diffusion Hodgkin Huxley model. Two of these are the charge density and the electric field.

This information is best displayed in a colour map form, as in Figure 4.15c.

In the resting state, the charge density profile is constant in time, as it is a relatively stable state with minimal redistribution of charge. It appears that the charge layers are built up inside the membrane as indicated by the plot of the sodium diffusion coefficient in Figure 4.15b. However, due to the extreme variation of the diffusion coefficient it is not apparent that there are still some areas of larger diffusion coefficient within the membrane region.

This can be clearly seen by plotting the logarithm of the diffusion coefficient. This is shown in Figure 4.16b where the logarithm of the diffusion coefficient is plotted alongside the charge density profile. This means the effective thickness of the membrane is smaller due to the use of the tanh functions to model the diffusion coefficient. The effective thickness of the membrane coincides with the region indicated by the dashed lines in Figure 4.16b. Examples of work undertaken with an altered tanh function giving a thicker membrane are shown in chapter 6. We then see that the charge build up is on the outside of this effective thickness in Figure 4.16c. Figure 4.16a shows the potential profile with time. Since in this case the resting potential has been established, there are no changes in the membrane potential over the time period shown, this makes sense as there are no noticeable changes in the charge density in Figure 4.16c during this time period.

The electric field is non zero within the membrane, as seen in Figure 4.17c. This is to be expected as there is a potential difference across the membrane. This field is constant with time during the resting state as it is a steady state. Comparison with Figure 4.17b shows that the non zero field region is largely contained within the effective thickness of the membrane. This makes sense since the potential change is across the membrane.

Similar colour map plots for the stimulated case are shown in Figures 4.18 and 4.19. The axes are restricted so that the changes that occur during an action potential are clearly visible as this is the most interesting behaviour. The redistribution of charge during an action potential can clearly be seen in Figure 4.18c. It is clear, from comparison with Figure 4.18a, that changes in the charge density occur during the action potential, it is these charge redistributions that give rise to the action potential. Prior to the stimulation, there is a build up of positive charge outside the cell, and a similar build up of negative charge on the inside. This is the same

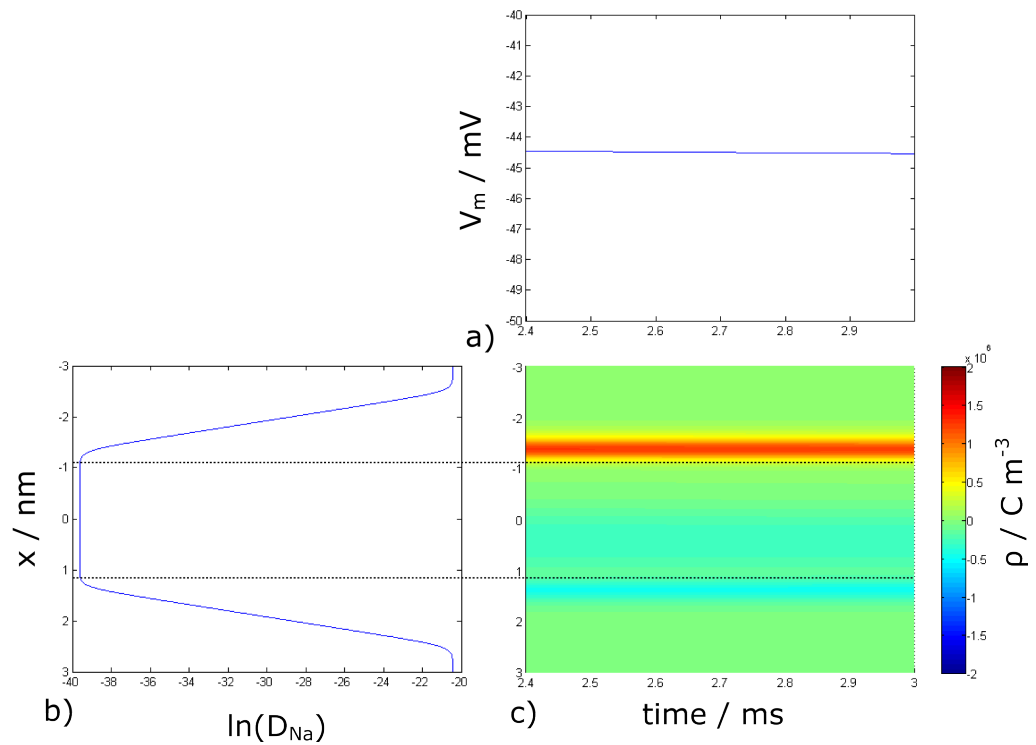


Figure 4.16: a) The resting potential state shown during the period 2.4 ms to 3.0 ms. This is just a flat horizontal line because by this stage the resting state has been well established. Compare with Figure 4.18a which shows an action potential. b) Logarithm of the diffusion coefficient profile for sodium. The dashed lines indicate the effective position of the membrane i.e. the region where the diffusion coefficient takes its smallest value. c) Charge density profile when no stimulation is provided. There is some charge build up at the membrane due to the uneven distribution of different ion types. It is this charge build up that gives rise to the non zero resting state. Dashed lines indicate effective position of the membrane.

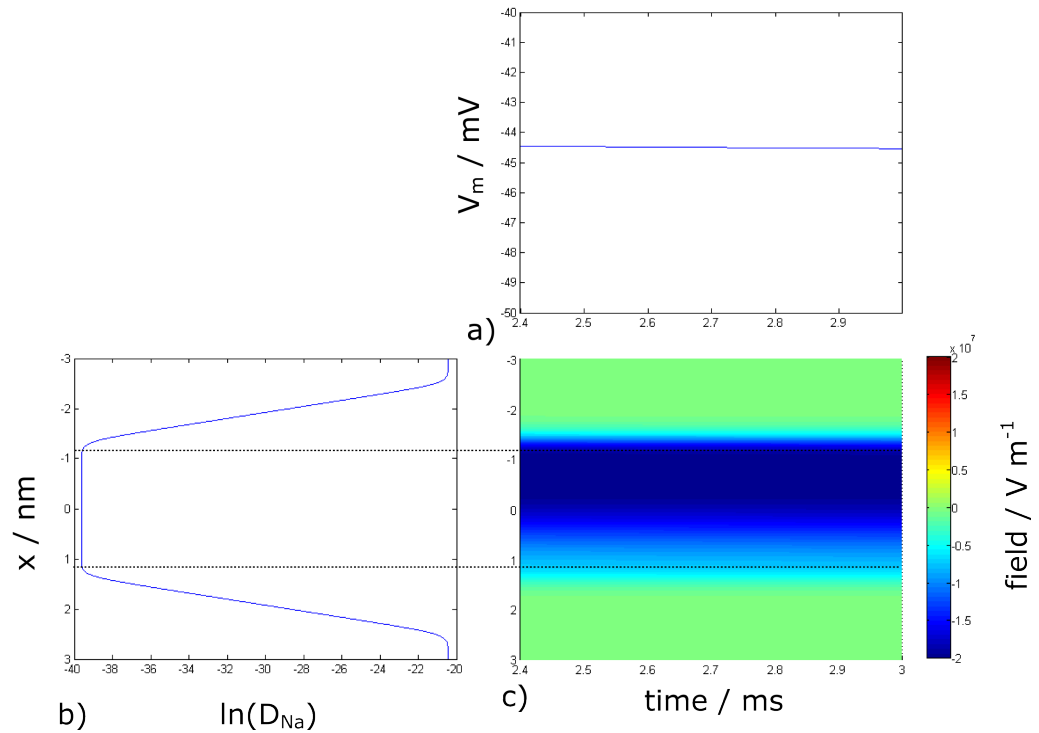


Figure 4.17: a) The resting potential state shown during the period 2.4 ms to 3.0 ms. This is just a flat horizontal line because by this stage the resting state has been well established. Compare with Figure 4.18a which shows an action potential. b) Logarithm of the diffusion coefficient profile for sodium. The dashed lines indicate the effective position of the membrane i.e. the region where the diffusion coefficient takes its smallest value. c) Electric field profile when no stimulation is provided. Due to the charge build up and non zero potential difference across the membrane there is an electric field within the membrane. In the resting state this field does not change with time. Dashed lines indicate effective position of the membrane.

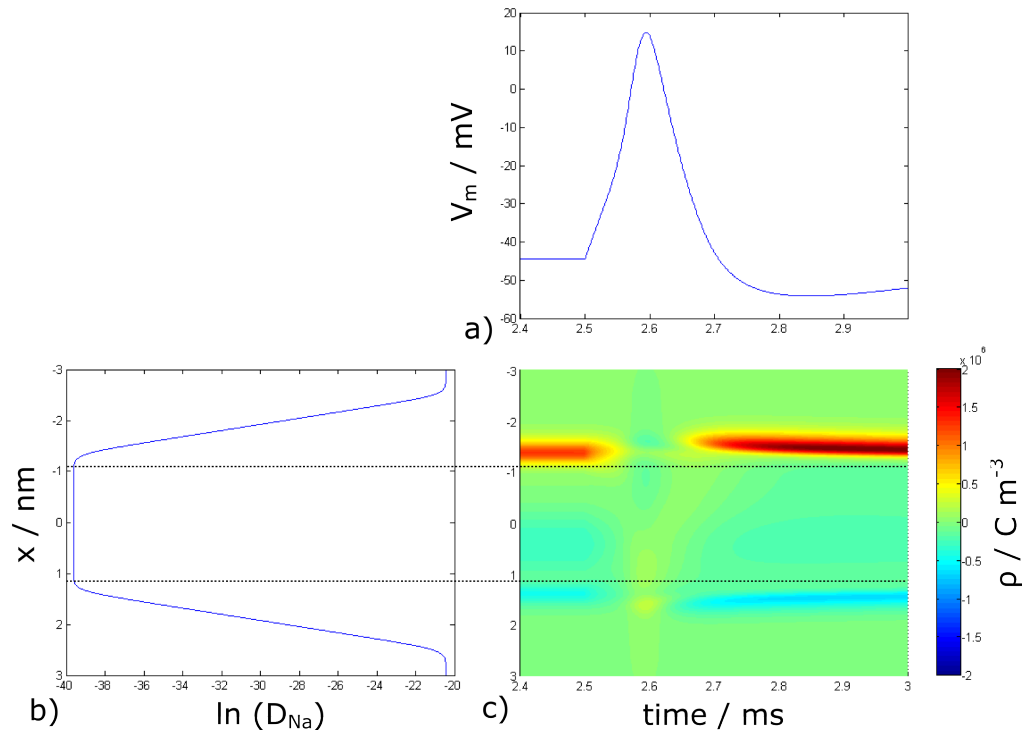


Figure 4.18: a) Close up of an action potential caused by a stimulus at  $t = 2.5$  ms. Used as a reference to correlate change in the charge density profile in c) with the membrane potential. b) Logarithm of the diffusion coefficient profile for sodium, indicates the effective position of the membrane. c) Charge density profile during an action potential. The charge density build up changes sign during the action potential. This is due to the redistribution of ions and is what causes the change in membrane potential. Dashed lines indicate effective position of the membrane, i.e. where the gradient in the diffusion coefficient is so low as to be effectively zero.

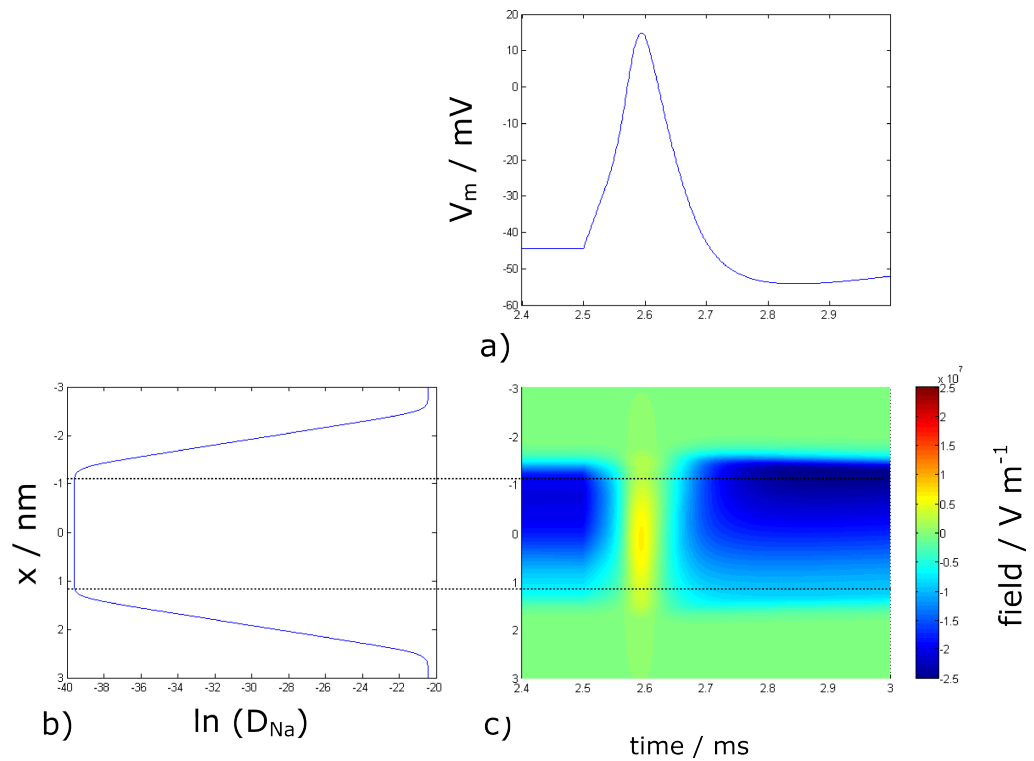


Figure 4.19: a) Close up of an action potential caused by a stimulus at  $t = 2.5$  ms. Used as a reference to correlate change in the electric field profile in c) with the membrane potential. b) Logarithm of the diffusion coefficient profile for sodium, indicates the effective position of the membrane. c) Electric field profile during an action potential. The electric field also changes sign during an action potential. This is to be expected as the membrane potential changes sign. The electric field changes occur mostly within the effective region of the membrane. Dashed lines indicate effective position of the membrane.

situation as seen during the resting state. Prior to the stimulation at 2.5 ms Figures 4.16c and 4.18c are clearly in agreement. Once stimulated the action potential occurs and this situation reverses, as a large influx of positive sodium ions leads to a positive charge inside the cell, causing the outside to have a negative charge. After the action potential, the system returns to its original state. This differences are clearly seen when comparing Figure 4.16c with 4.18c following the stimulation at 2.5 ms.

The behaviour of the electric field during an action potential is clearly shown in Figure 4.19c. As the potential rises, the field within the membrane increases from its original negative value to a positive one. After the action potential it then returns back to its resting state. This behaviour is largely confined to the effective membrane region.

The changes in the charge density and electric field profiles which occur during an action potential are consistent with the Hodgkin Huxley model. The membrane acts in a similar manner to a parallel plate capacitor, with charge either side of the membrane. During the action potential this charge changes sign as the currents flow through the membrane and a new charge distribution is reached at the peak of the action potential. This is then reversed as the system returns to rest.

It is also possible to generate similar colour map plots for the different ion species involved. This demonstrates one of the key benefits of the DDHH model, being able to keep track of the ion movements and concentration profiles. This feature could be of use when modelling systems with more restricted spatial extent.

Figure 4.20c shows the change, from the initial conditions, in sodium concentration during an action potential. Using 4.20a as a comparison, it is clear to see that significant changes occur following the stimulation at 2.5 ms. There is some noticeable change even prior to the action potential, this is because the ion channels are not completely shut and so sodium is free to move a little even during the resting phase. During the action potential, this shift of sodium into the cell becomes more pronounced. An accompanying decrease in the sodium concentration immediately outside the cell is also observed. It is also clear to see that there is a delay before noticeable sodium currents are seen following the stimulation. This is due to the time taken for the sodium channels to start opening in response to the stimulation and so is to be expected.

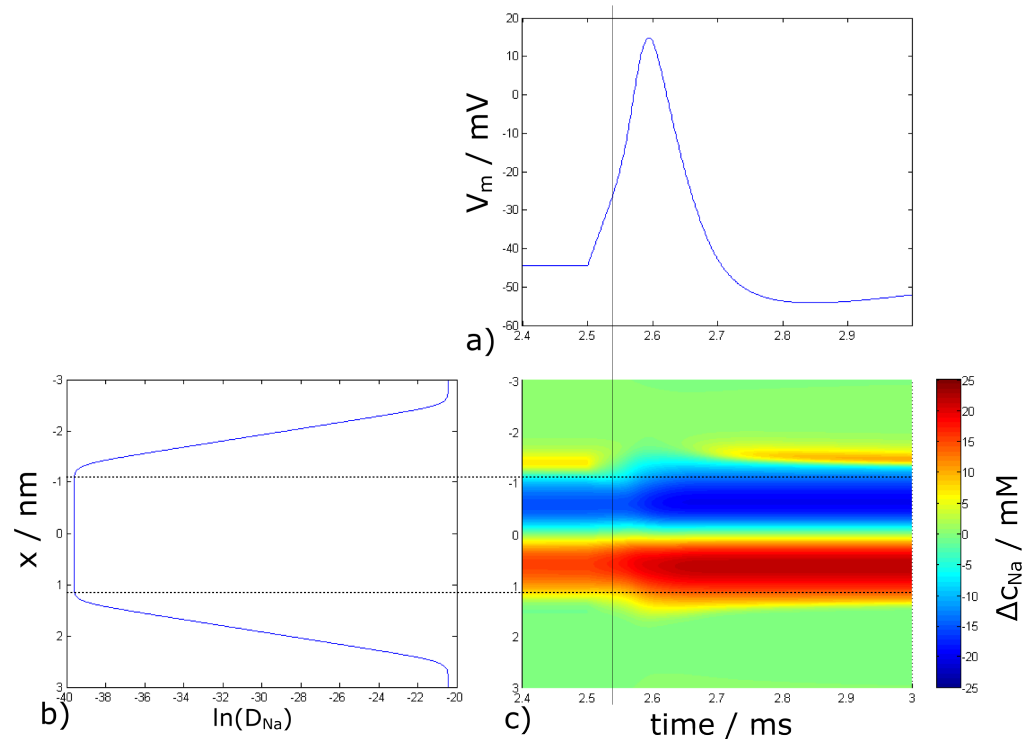


Figure 4.20: a) Close up of an action potential caused by a stimulus at  $t = 2.5$  ms. Used as a reference to correlate change in the sodium concentration profile in c) with the membrane potential. b) Logarithm of the diffusion coefficient profile for sodium, indicates the effective position of the membrane. c) Plot showing the change in sodium concentration relative to the initial conditions. There is a significant increase in the concentration of sodium on the intracellular side during an action potential. The positive  $y$  direction (downwards in the Figure) is the intracellular space. Black line from Figure a) to Figure c) indicates onset of the significant sodium current caused by the opening of the ion channels. Dashed horizontal lines from Figure b) to Figure c) indicate effective position of the membrane.

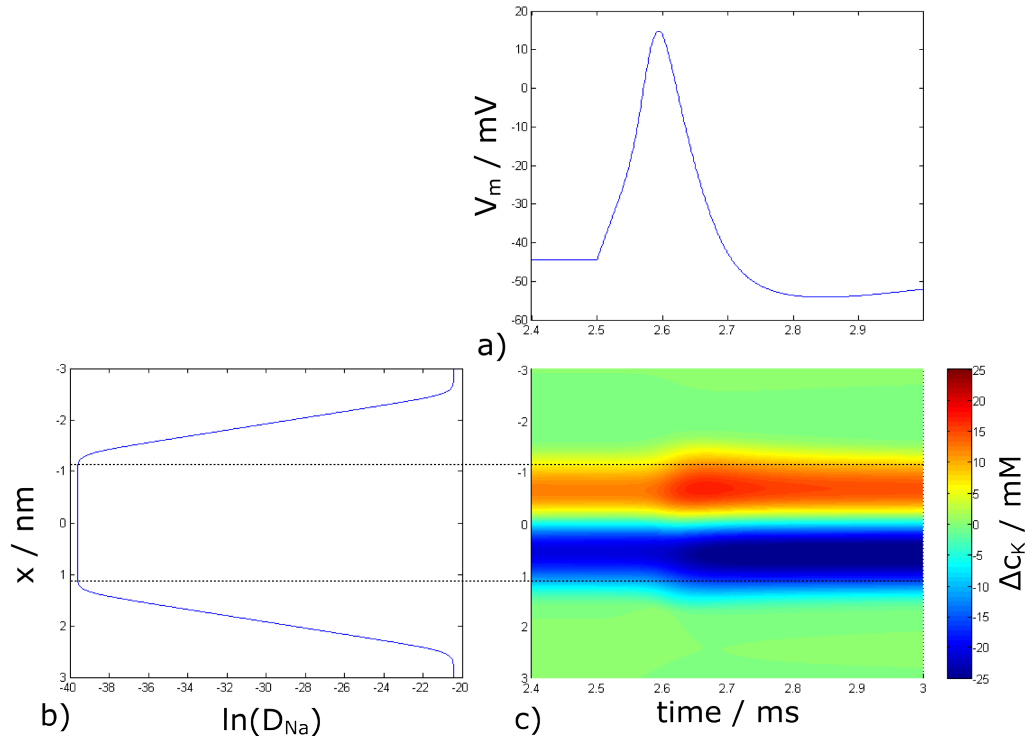


Figure 4.21: a) Close up of an action potential. b) Logarithm of the diffusion coefficient profile for sodium, indicates the effective position of the membrane. c) Plot showing the change in potassium concentration relative to the initial conditions. There is a significant increase in the concentration of potassium on the extracellular side during an action potential. The positive  $y$  direction (downwards in the Figure) is the intracellular space. Black line indicates the onset of the significant potassium current caused by the opening of the ion channels. Note this is later than the sodium current. Dashed lines indicate effective position of the membrane.

The initial concentration profiles are smoothly evolving through the membrane, from the extracellular values to the intracellular values. Due to the fact that the activation and inactivation gates for sodium are never fully closed, there is always some ability for sodium to move through the membrane. This results in a change in the concentration of sodium within the membrane, as sodium moves into the cell. During an action potential, the gates open and this flow increases significantly.

Similar behaviour is observed for potassium, as shown in Figure 4.21c. Figure 4.21a is useful to correlate changes in the potassium concentration with changes in the membrane potential. In the case of potassium ions

the situation is reversed, potassium shifts from inside the cell to outside the cell (upwards in Figure 4.21c) , with a noticeable increase during the action potential. This is not reversed after the action potential because the change in ionic concentration that occurs during the pulse is not sufficient to reverse the concentration gradient. It is noticeable that the potassium concentration undergoes its major change at a later phase of the action potential than the corresponding change for sodium. This is to be expected because the potassium gates are slower and don't start to open until the membrane potential starts to become more positive (a consequence of the opening of the sodium channels).

Chloride ions display markedly different behaviour, as seen in Figure 4.22c. Firstly it is noticeable that prior to the action potential the changes from the initial conditions are much smaller than those seen for sodium and potassium. This is because the chloride concentration difference between the intra and extracellular regions is much less than for the other ions. Also the conductance for chloride ions is considerably smaller.

Even though the chloride conductance is constant with time, there is some noticeable change in chloride concentration during the action potential. This is because the reversal of the electric field affects the drift term in the drift diffusion equations, thereby changing the flux of the chloride ions.

### 4.3 Validation of Single Membrane Results

One process that was used to help validate the results was convergence tests. The simulation was run for a variety of grid spacings to see if the results converged at small enough grid point separation. The results in Figure 4.23 show that as the grid spacing is reduced, the results converge. The quoted  $\Delta x$  values refer to the minimum grid spacing for a given simulation. Given that the grids used are non uniform, the actual grid spacing will vary across the computational domain, as indicated by 4.4 for example. It was also necessary to do a similar check with the time step, as this could also have a significant impact on the results. Figure 4.24 shows that changing the time step has a minimal effect on the results.

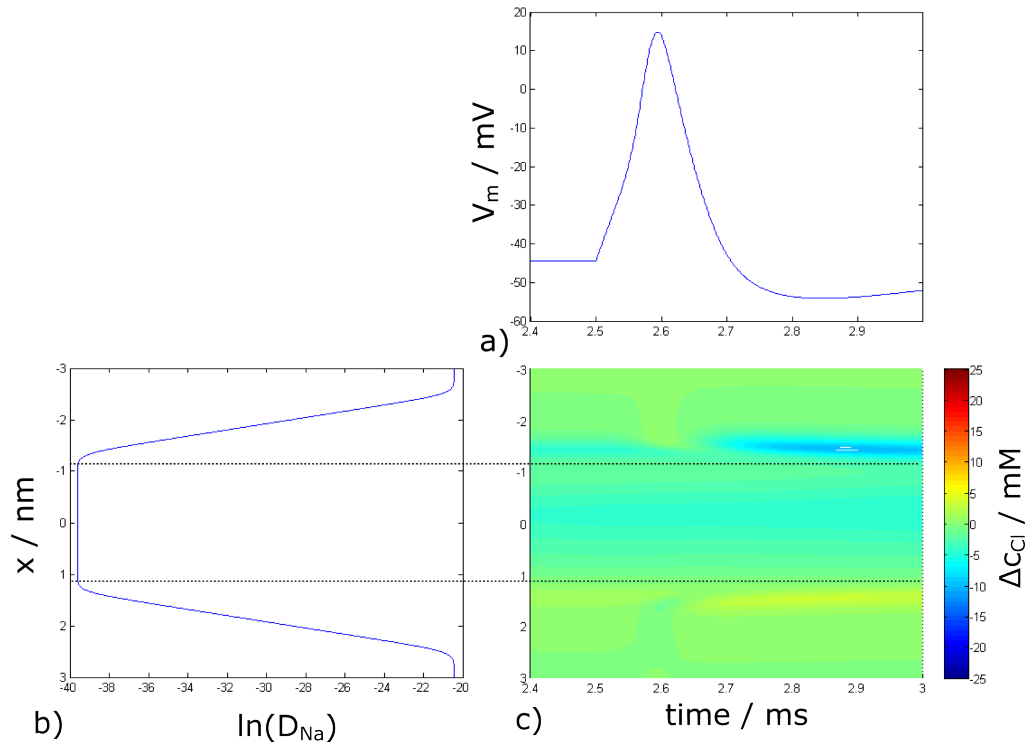


Figure 4.22: a) Close up of an action potential. b) Logarithm of diffusion coefficient profile for sodium, indicates the effective position of the membrane. c) Plot showing the change in chloride concentration relative to the initial conditions. It is noticeable that the change in chloride concentration is much lower than for the other ionic species. This is because the conductance for chloride ions is a constant small value. There is still some noticeable change in the profile of the chloride ions during the action potential. This is due to the change in the electric field, which alters the drift term in the drift-diffusion equation. Dashed lines indicate effective position of the membrane.

### 4.3 Validation of Single Membrane Results

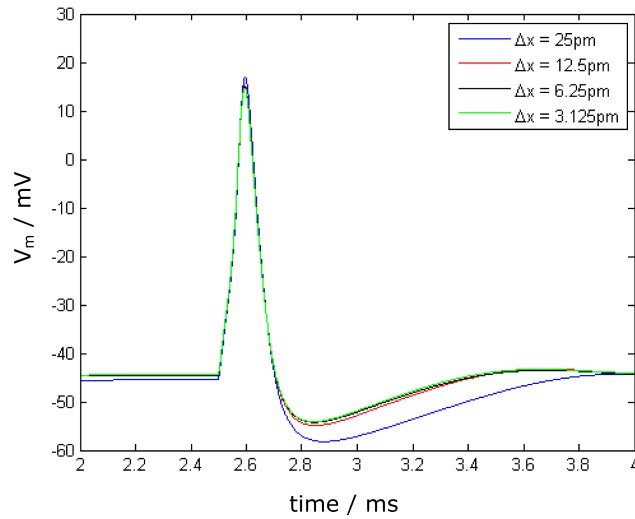


Figure 4.23: Testing convergence by varying the grid spacing

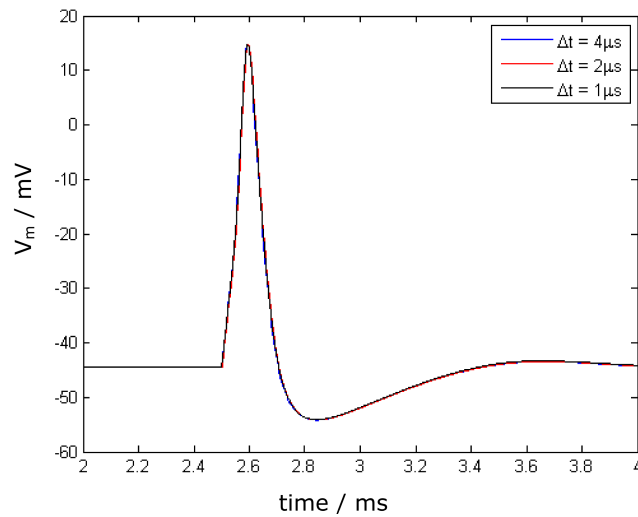


Figure 4.24: Testing convergence by varying the time step

### 4.4 Single Membrane Conclusions

The single membrane model is important, in that it allows Hodgkin Huxley dynamics to be incorporated into a semi-permeable membrane model, similar to that discussed in [52]. It is the simplest system to be simulated using the drift diffusion enhanced Hodgkin Huxley model. Important neuronal behaviours, such as action potentials, resting potential and sub-threshold responses are exhibited by the model.

In reality of course, taking a slice through a cell means that two membrane layers are required and the internal dimensions of the cell are not semi infinite. Also when applying the model to deal with detectors, it will be necessary to have the detector reasonably close, 50-100nm, to the cell. This will mean the extra cellular space will also be restricted and so the model must be adapted to reflect that. These adaptations are discussed in the next chapter.

# Chapter 5

## Double Membrane

The single membrane results described in the previous chapter show that it is possible to incorporate the Hodgkin Huxley behaviour into a drift diffusion model. Unfortunately the idea of semi-infinite intra and extracellular space separated by a membrane is not close to reality for a neuron in vitro or in vivo.

This means it is necessary to extend the model to allow the restriction of the extracellular space and also account for the fact that the intracellular space is enclosed by the membrane. This means that in a 1D slice through the cell there will be two membrane layers.

The ionic diffusion coefficients are of order  $1 \times 10^{-9} \text{ m}^2 \text{ s}^{-1}$  and the maximum simulation time period is  $t_{max} = 5 \text{ ms}$ . The root mean square diffusion thickness layer is given by

$$X_{rms} = \sqrt{2Dt_{max}} \approx 3 \mu\text{m}. \quad (5.1)$$

Since the cell width is  $2 \mu\text{m}$  it was necessary to include the second membrane.

However due to the very low flow of ions through the membrane no noticeable interaction effects were expected to be observed.

### 5.1 Outline

The system modelled is shown schematically in Figure 5.1. The model consists of an intracellular region separated from two extracellular regions by membrane layers. The bottom layer is a glass sheet which represents the coverslip on which the cell is grown in experiments and provides a

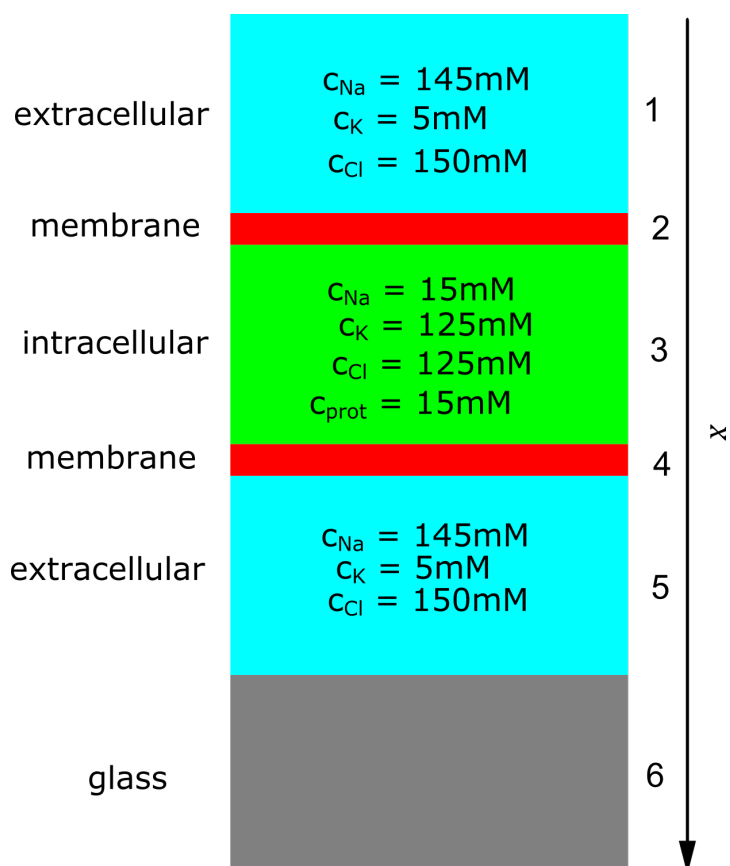


Figure 5.1: Schematic showing the layers involved in the double layer model. At the top is a semi infinite extracellular layer. Beneath this lies the first membrane layer. This is followed by the intracellular region. The fourth layer is another membrane layer, which leads to a restricted region of extracellular space, followed by a layer of glass.

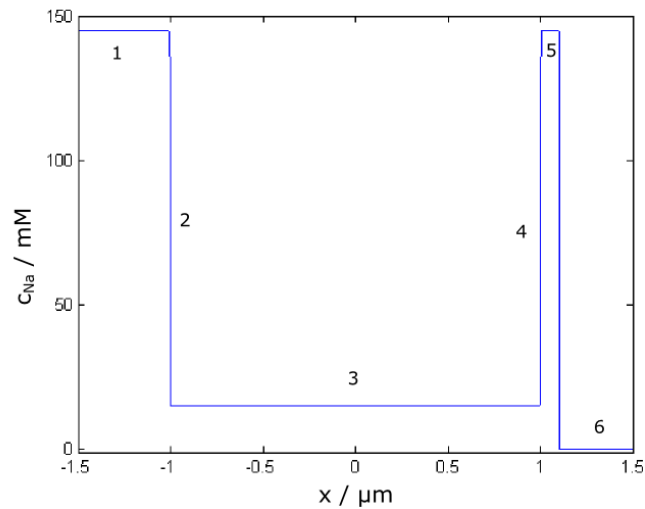


Figure 5.2: Initial sodium concentration profile. Key positions indicated by numbered points. 1 is the semi infinite extracellular region. The area indicated by 2 is the first membrane layer. 3 is the intracellular region. The second membrane region is marked as 4. The restricted intracellular space is indicated by position 5. The glass layer is at region 6, where the concentration of all ions is zero. The transition regions are described by tanh functions.

realistic restriction to the extracellular space. The distance between the cell membrane and the glass is approximately 100 nm.

Both membranes incorporate ion channels and are affected by the Hodgkin Huxley gating variables. As with the single membrane results it is important that the membrane dynamics are capable of reproducing the range of neuronal behaviours, action potentials, resting potentials and sub threshold responses.

The initial concentration profiles are more complex than in the single membrane case, as they have to incorporate two membrane regions and the glass region. The profiles are set up in a similar way to the single membrane case, with the various ion types having bulk concentrations in the intracellular and extracellular media. To manage the transitions within the membrane regions, tanh functions are used as discussed in Chapters 3 and 4. A further tanh function is used to bring all ion concentrations rapidly to zero at the glass interface. This is necessary to enable a physically realistic initial condition.

Figures 5.2, 5.3 and 5.4 show the initial concentration profiles used in the

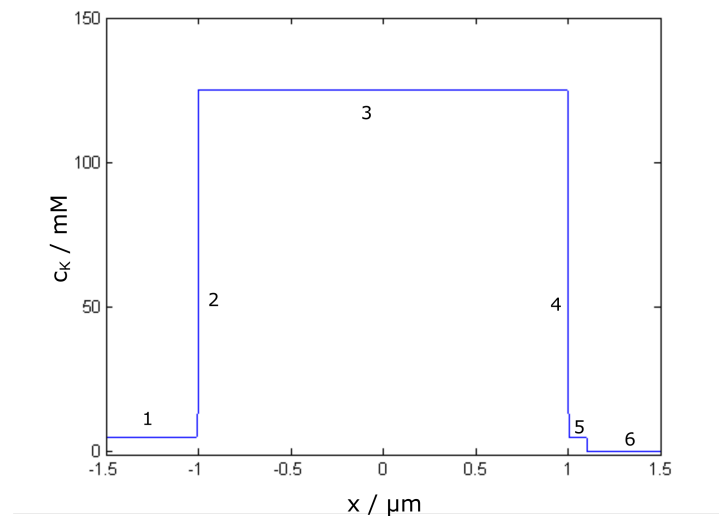


Figure 5.3: Initial potassium concentration profile. Key positions indicated by numbered points. 1 is the semi infinite extracellular region. The area indicated by 2 is the first membrane layer. 3 is the intracellular region. The second membrane region is marked as 4. The restricted intracellular space is indicated by position 5. The glass layer is at region 6, where the concentration of all ions is zero. The transition regions are described by tanh functions.

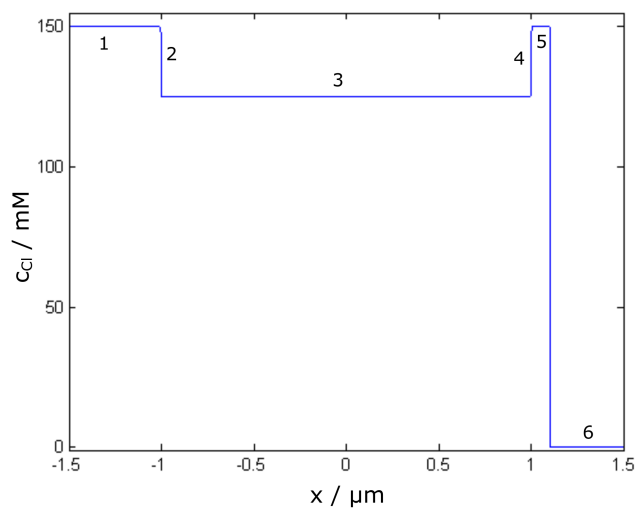


Figure 5.4: Initial chloride concentration profile. Key positions indicated by numbered points. 1 is the semi infinite extracellular region. The area indicated by 2 is the first membrane layer. 3 is the intracellular region. The second membrane region is marked as 4. The restricted intracellular space is indicated by position 5. The glass layer is at region 6, where the concentration of all ions is zero. The transition regions are described by tanh functions.

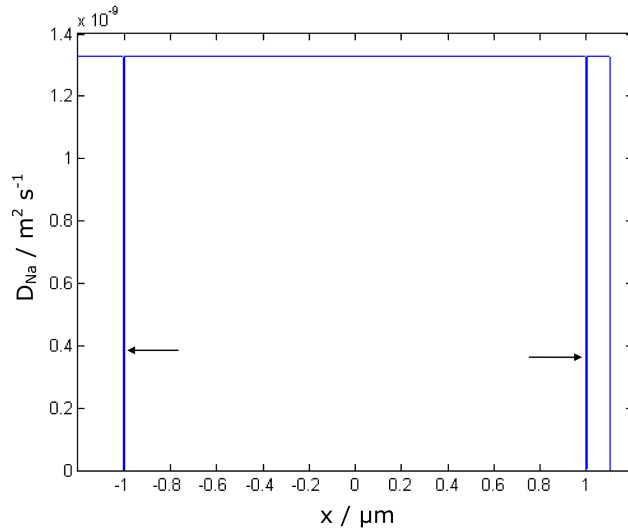


Figure 5.5: Sodium diffusion coefficient profile. There are two membrane regions as indicated by the arrows on the plot.

simulations. The intracellular region in these figures is between  $x = -1\mu\text{m}$  and  $x = 1\mu\text{m}$ . The restriction of the extracellular medium between the cell and the glass layer is also clearly seen.

Figure 5.5 shows the diffusion coefficient profile for sodium. As with the single membrane case, the membranes are represented by regions of extremely low, but non-zero, diffusion coefficient. Since physically the ions would not diffuse into the glass region, it is appropriate to set the diffusion coefficients of all ions to zero within the glass. This transition is also handled using a tanh function. The profiles for the other ions are similar to that of sodium and so are not reproduced here.

## 5.2 Results

As with the single membrane simulations, the initial state of the system is electroneutral everywhere. This means that the system will run through an unstimulated action potential initially. This occurs for the same reason as in the single membrane case, a zero difference in potential across the membrane is not a stable state in the Hodgkin Huxley model. This will then settle to a resting potential unless otherwise stimulated, usually within 2ms.

Stimulating the cell using a diffusion coefficient step at time  $t = 2.5$  ms gives rise to an action potential as shown in Figure 5.6. This shows that

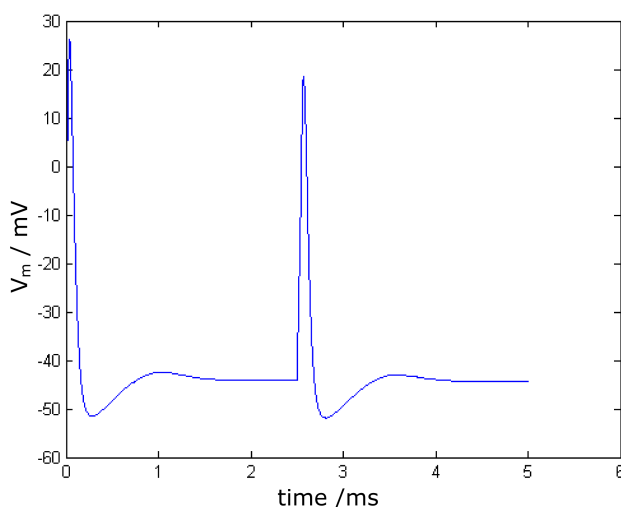


Figure 5.6: The double membrane model produces action potentials just like the single membrane model, for comparison see Figure 4.8. The first spike is due to the system being set up in an unstable initial state. The second is an action potential triggered by a stimulus applied at 2.5ms. As with the single membrane case, a stimulus is provided in the form of an artificially elevated sodium diffusion coefficient within the membrane.

the introduction of a second membrane and the restriction of extracellular space do not diminish the ability to trigger action potentials within the model. The first spike in Figure 5.6 is due to the initial condition of zero potential difference across the membrane, which is not a stable point of the Hodgkin Huxley model. The resting potential of this particular model is approximately  $-43.6\text{mV}$ . This means that in a resting state the interior of the cell is negatively charged relative to the exterior.

Using the double membrane schematic allows the full width of the cell to be simulated. Figure 5.7b shows how the potential varies with space and time. A stimulation is provided at 2.5ms using an increased sodium diffusion coefficient within the membrane, this results in an action potential as shown in Figure 5.7a. It is clear that the potential within the cell changes rapidly as can be seen by the change in colour within the cell from blue to orange, see Figure 5.7b. The sharp change in potential at  $x = -1\mu\text{m}$  and  $x = 1\mu\text{m}$  suggest a large electric field within the membrane. It is also seen that the action potential spreads across the cell extremely rapidly, such that sufficiently far from the membrane the potential remains spatially constant within the cell.

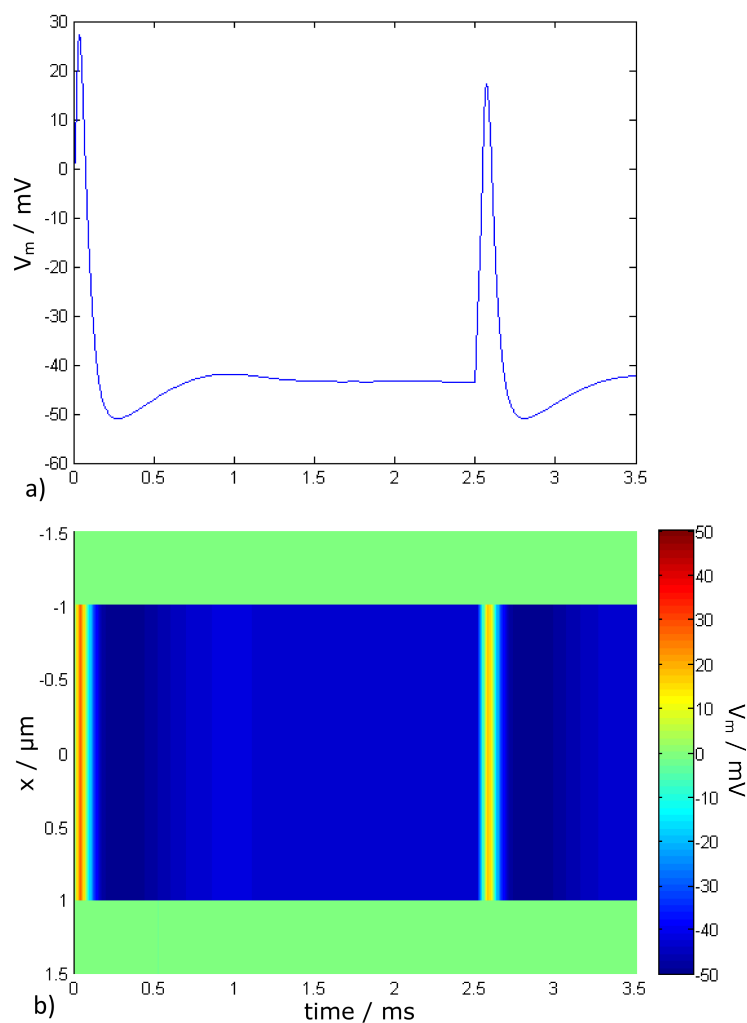


Figure 5.7: a) An action potential versus time for reference. b) The potential profile. The membranes separating the intra and extracellular regions are too narrow to be visible on the scale of this plot. It can be seen that the potential inside the cell is almost uniform throughout the width of the cell. Action potential pulse is clearly seen just after stimulation at 2.5 ms.

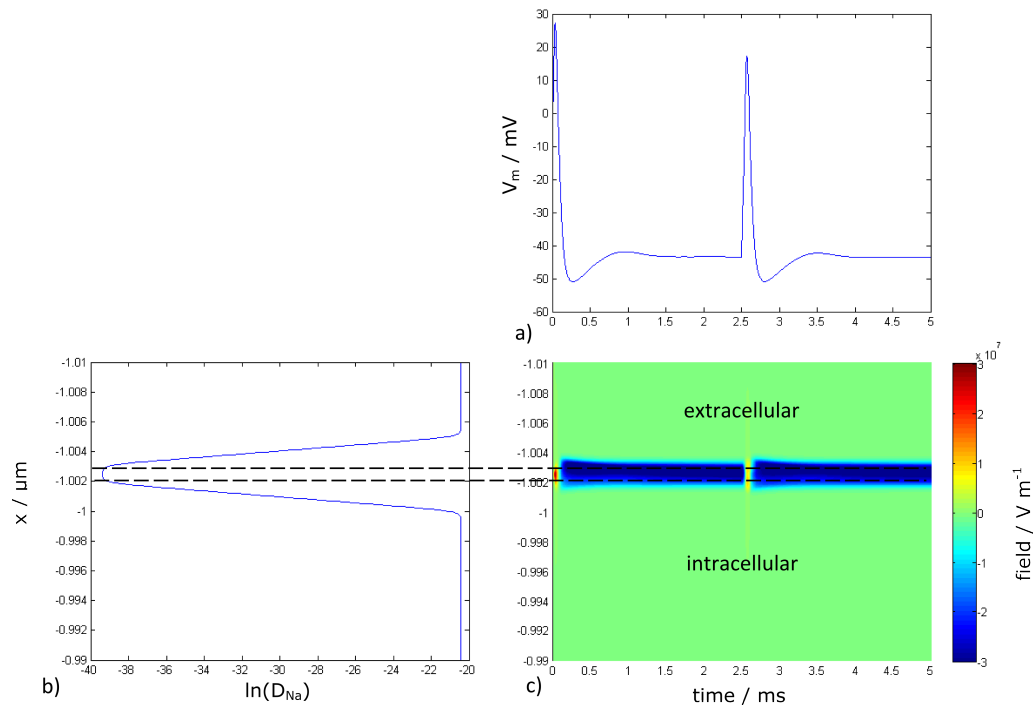


Figure 5.8: a) An action potential versus time for reference. b) Logarithm of the diffusion coefficient for sodium. This is used to indicate the effective region of the membrane in which the diffusion coefficient will have values dictated by the Hodgkin Huxley model. c) Electric field close to the top membrane. There is a large electric field within the membrane due to the change in the potential across it. Dashed lines indicate the effective membrane region. The cell is stimulated at 2.5ms causing an action potential. This changes the sign of the electric field due to the change in the potential difference across the membrane. This can be seen as a colour switch from blue to yellow during the action potential.

The fact that most of the spatial variation in potential occurs within/close to the membrane is supported by the field profile.

Figures 5.8c and 5.9c show the electric field in the region of the top and bottom membranes. The field is of a large magnitude within the membrane but rapidly weakens away from it. This is seen as a colour change from blue to green in the case of the top membrane, Figure 5.8c, and a colour change from red to green in the bottom membrane, Figure 5.8c. As expected the field at each membrane is equal and opposite. Both figures 5.8b and 5.9b show the logarithm of the diffusion coefficient of Sodium and are used as a guide to indicate the position of the membrane. Figures 5.8a and 5.9a show

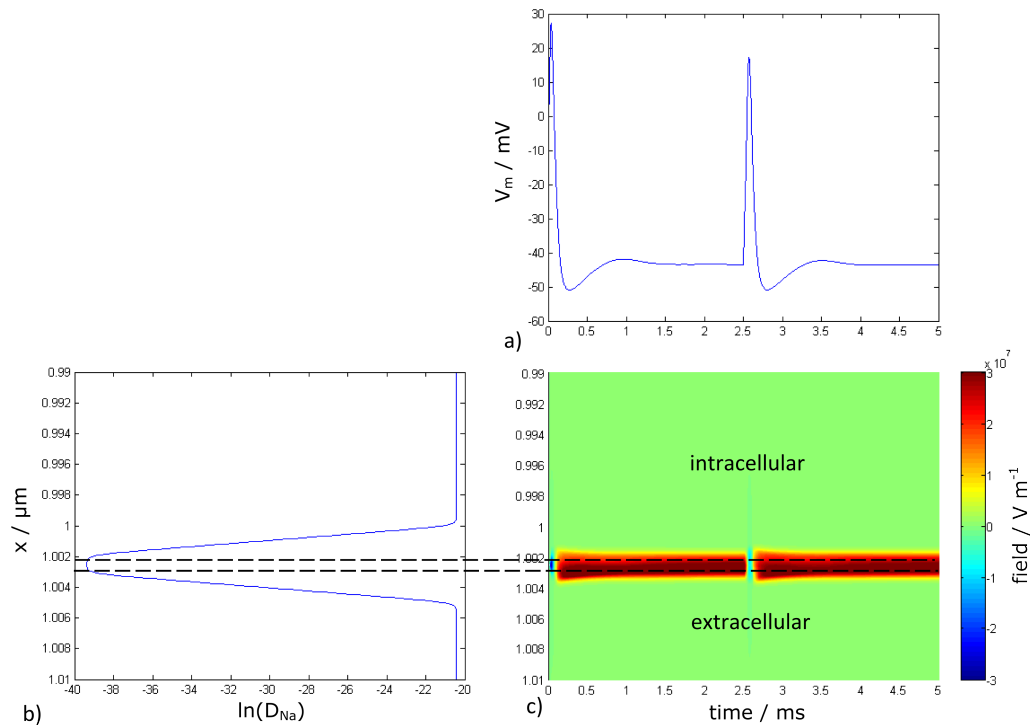


Figure 5.9: a) An action potential versus time for reference. b) Logarithm of the diffusion coefficient for sodium. This is used to indicate the effective region of the membrane in which the diffusion coefficient will have values dictated by the Hodgkin Huxley model. c) Electric field close to the bottom membrane. As with the top membrane shown in Figure 5.8c the electric field is large within the membrane and features a change in sign during the action potential. This is indicated by a change in the colour from red to pale blue during the action potential. The field within the bottom membrane is opposite that found within the top membrane. Dashed lines indicate the effective membrane region.

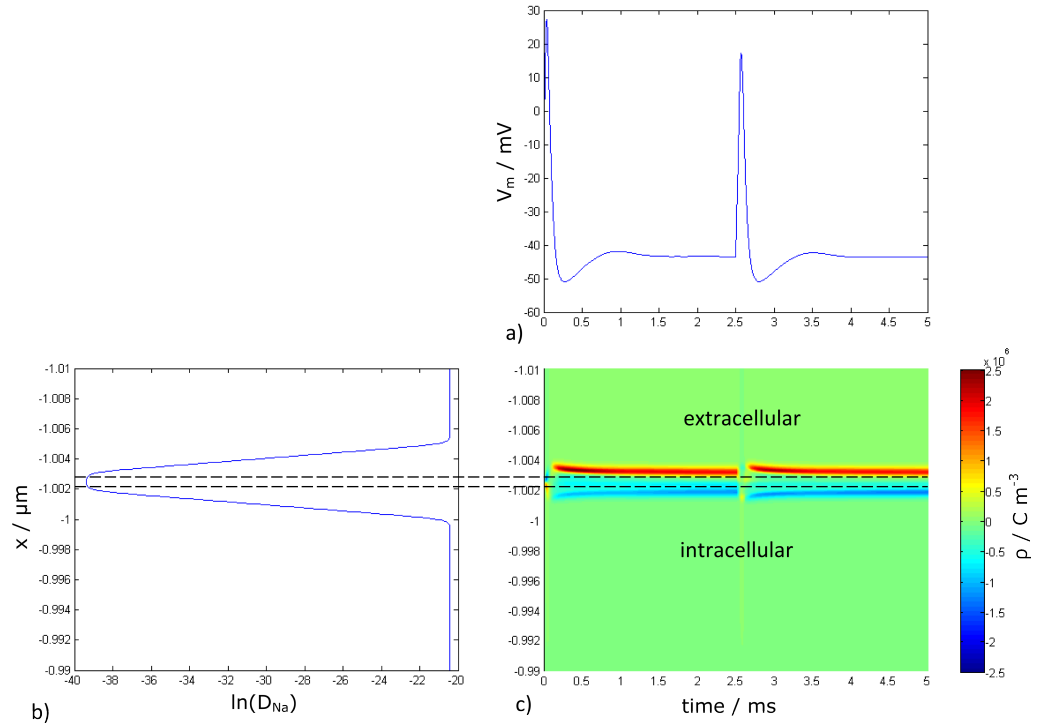


Figure 5.10: a) An action potential versus time for reference. b) Logarithm of the diffusion coefficient for sodium. This is used to indicate the effective region of the membrane in which the diffusion coefficient will have values dictated by the Hodgkin Huxley model. c) Charge density close to the top membrane, indicated by dashed lines. The charge builds up on the faces of the membrane, indicated by the red and blue bands along the membrane boundaries. This distribution undergoes a change of sign during an action potential, indicated by the change in colour during the action potential. The stimulus is provided at 2.5ms.

the membrane potential profile with time during the course of an action potential.

During an action potential, the sign of the field briefly reverses as the charge is redistributed and the membrane potential swaps sign. This occurs for both membranes and is observed as a brief colour switch during the action potential in Figures 5.8c and 5.9c. The effective membrane region is indicated by dashed lines.

Figures 5.10c and 5.11c show the charge density profiles in the region of the top and bottom membranes. The positions of the membrane are indicated by the diffusion coefficient profile shown in figures 5.10b and 5.11b,

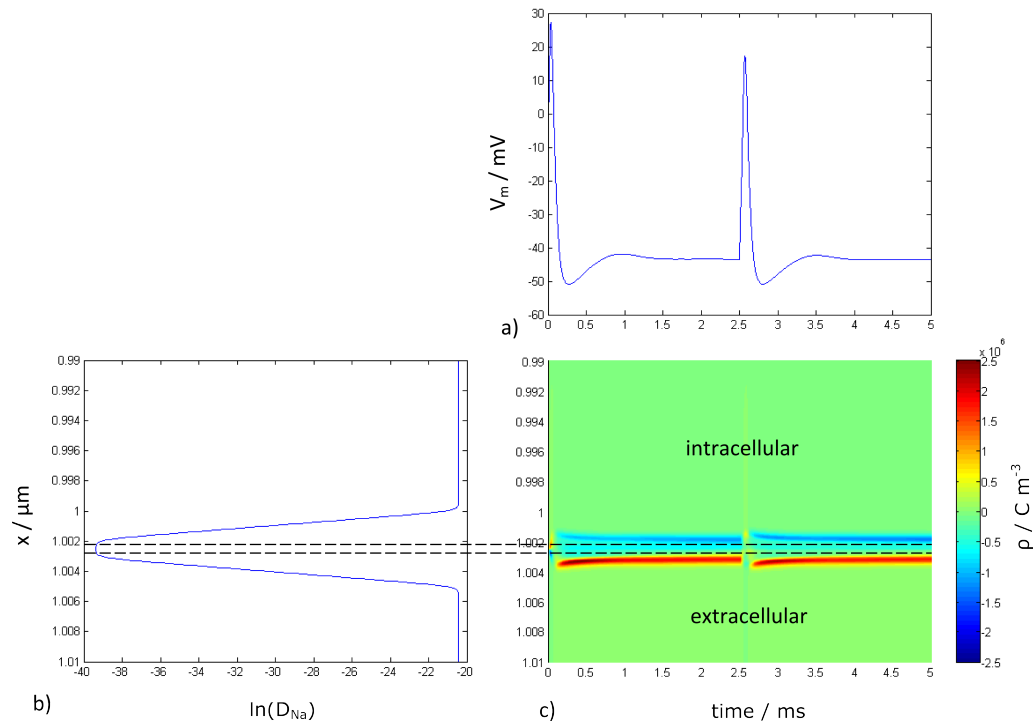


Figure 5.11: a) An action potential versus time for reference. b) Logarithm of the diffusion coefficient for sodium. This is used to indicate the effective region of the membrane in which the diffusion coefficient will have values dictated by the Hodgkin Huxley model. c) Charge density close to the bottom membrane, indicated by dashed lines. The charge builds up on the faces of the membrane and can be seen as blue and red bands along the dashed lines. This distribution undergoes a change of sign during an action potential. This is observed as a change in colour in the colour plot. The stimulus is provided at 2.5ms. Note that during the resting phases the charge on the inner faces of the membrane is negative, which is consistent with the negative membrane potential. There is a brief change of sign during the action potential.

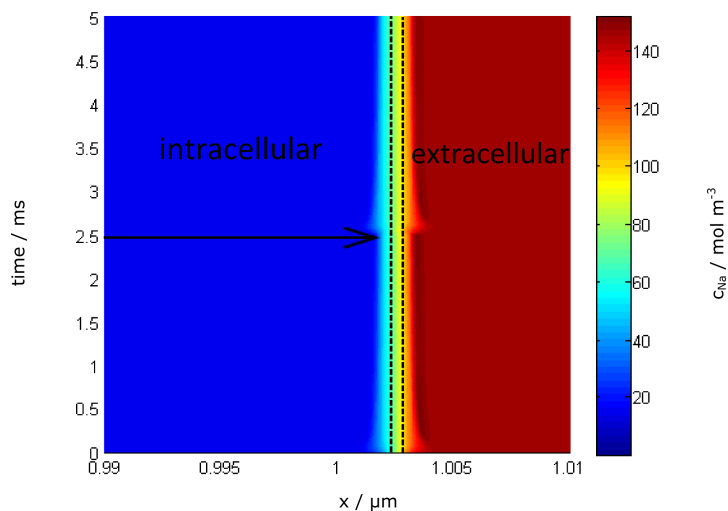


Figure 5.12: Sodium concentration profile close to the bottom membrane (indicated by dashed lines). A stimulation is provided at 2.5 ms as indicated by the arrow. Shortly after this point a bulge can be seen indicating the flow of sodium ions into the cell (from right to left on the figure). This is seen as a shift to a paler red on the right hand side of the membrane, along with a corresponding shift to a paler blue on the left side of the membrane in the figure. It is this flow of ions that causes the increase in membrane potential towards positive values.

whilst the potential profile is shown by figures 5.10a and 5.11a. The only significant charge build-ups occur within the regions close to the membranes, with red and blue bands on the top membrane in Figure 5.10c and blue and red bands on the bottom membrane as in Figure 5.11c. Whilst the neuron is at rest, the charge on the inner faces of the membrane is negative (blue in the figure), whilst the outer faces are positive (red in the figure). This is to be expected as the resting potential of the cell is negative. During the action potential there is a brief period in which the interior faces of the membrane carry a positive charge indicated by a colour change from blue to yellow. This is what gives rise to the spike in the potential.

Whilst the charge density plots give a good picture of the overall situation during an action potential, it is also useful to consider the various different ion species. Figure 5.12c shows the spatio temporal evolution of the sodium concentration. It is clear that there is only limited movement during the resting phases, but once the ion channels open, a bulge is seen, at 2.5ms, which indicates that sodium is entering the cell. This is indicated

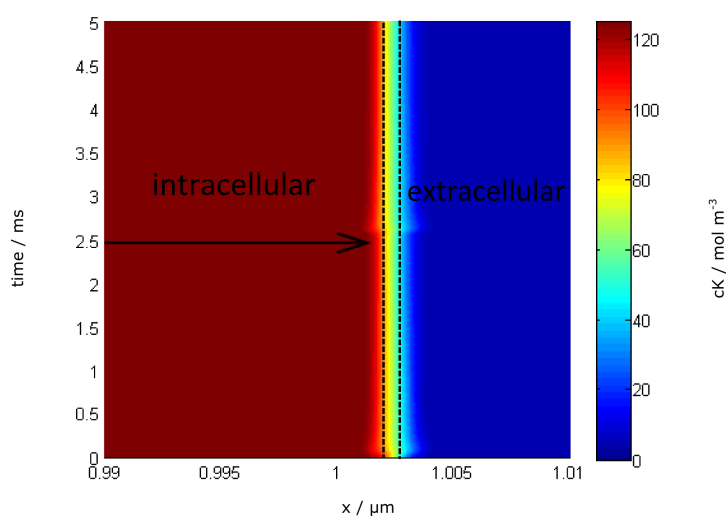


Figure 5.13: Potassium concentration profile close to the bottom membrane (indicated by dashed lines). A stimulation is provided at 2.5 ms as indicated by the arrow. Shortly after this point a bulge can be seen indicating the flow of potassium ions out of the cell (from left to right on the figure). This is seen as a shift to paler red on the left side of the membrane and a corresponding shift to a paler blue on the right of the membrane in the figure. This flow of positively charged potassium ions out of the cell leads to the membrane potential being restored to its resting state.

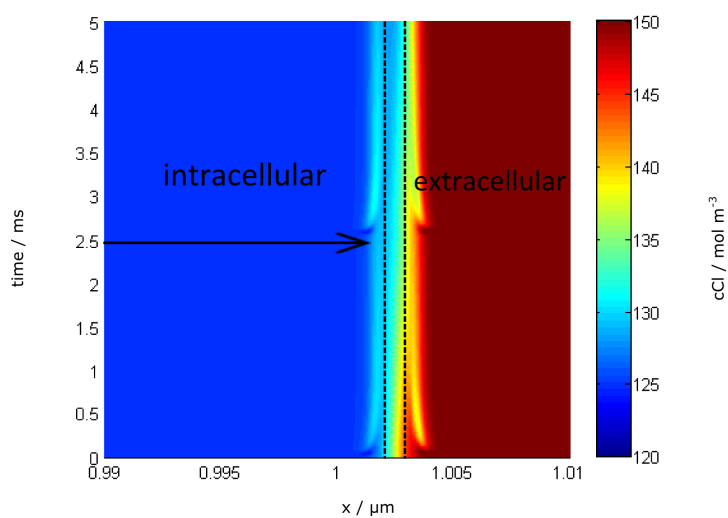


Figure 5.14: Chloride concentration profile close to the bottom membrane (indicated by dashed lines). The chloride ions do exhibit some interesting behaviour after a stimulus even though they are not one of the main ions involved with the triggering of the action potential. There is a noticeable change in the concentration of chloride ions following the stimulus at 2.5 ms (indicated by arrow). Even though the conductance of chloride ions is small, the change in the electric field within the membrane during an action potential causes a subtle shift in the concentration of chloride ions.

as a shift to a paler red on the right of the membrane and a corresponding shift to a paler blue on the left of the membrane in Figure 5.12c. From this it is clear that the ion channels have the most significant impact on the movement of sodium. It is this rush of sodium ions into the cell that leads to the rising phase of the action potential.

Figure 5.13 is similar, but shows the situation for potassium. Once again the profile is relatively stable during resting phases, but shows changes during an action potential. Here a bulge is seen just after 2.5 ms which indicates the potassium leaving the cell. Ion flow is observed as a shift to a paler blue on the right of the membrane and a corresponding shift to a paler red on the left of the membrane in Figure 5.13. This is another example of the voltage gated ion channels in action. The flow of potassium out of the cell causes the membrane potential to return towards its resting value.

The situation for chloride however is somewhat different as can be seen in Figure 5.14. For chloride ions the membrane conductance is a fixed value. There are no voltage gated channels as in the case of sodium or potassium. This means the main variables controlling the movement of chloride ions are the chloride concentration gradient and the electric field. There are still some interesting features in the chloride concentration profile. Shortly after 2.5 ms there is some indication of a change in the profile. Since the concentration gradient of the chloride ions across the membrane is relatively constant in time, the change in concentration profiles must be due to the electric field altering sign during the action potential.

The glass layer is present to provide this restriction in a realistic manner. The ability to simulate a neuron in a region of restricted extracellular space is a necessary step towards modelling the detector technologies which will provide a way to detect action potentials. These are discussed in the next chapter.

# Chapter 6

## Detectors

The double membrane model can be further adapted to include additional layers which act as electrodes that can be used to detect action potentials. Cells can be grown on a thin gold film, which allows the possibility of using surface plasmon resonance to detect action potentials.

The model layer structure is shown in Figure 6.1 and incorporates a thin gold film of 50nm thickness. In the gold film, the conduction electrons will move in response to changes in the electric field at the electrode surface. This means the concentration of electrons will have to be modelled using drift diffusion equations. These will take the same form as for the other ionic species in the previous chapters, but with extra terms to account for the concentration of electrons. Of course it should be noted that the electrons will only have a non-zero concentration within the gold layer.

### 6.1 Gold

In order to model the gold it is necessary to calculate the initial concentration of conduction electrons and their diffusion coefficient. This will allow the drift diffusion model to be applied to the gold layer in a similar manner to the other layers in which ions move.

Gold has a density  $\rho = 19300 \text{ kg m}^{-3}$  and an atomic weight of 197 g/mol. If each gold atom contributes 1 conduction electron that means the number density,  $n$ , of conduction electrons is the same as the number density of atoms [56], i.e.

$$n = \frac{19300}{0.197} A_v = 5.9 \times 10^{28} \text{ m}^{-3}. \quad (6.1)$$

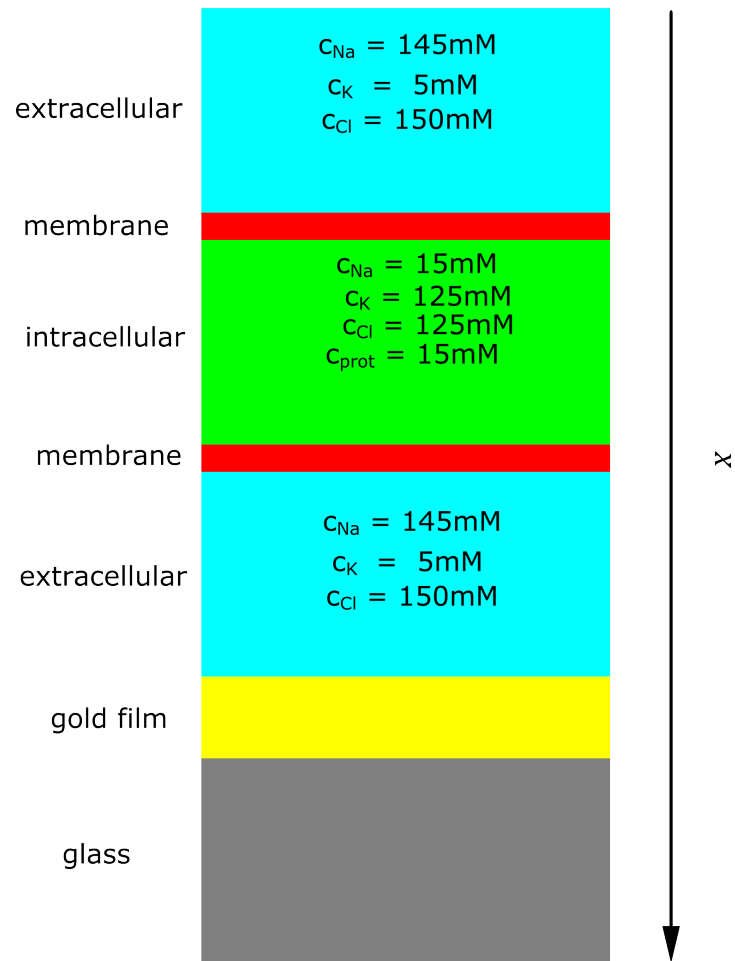


Figure 6.1: Schematic diagram showing the layer structure for detection of action potentials. This is the same as the layer structure for the double membrane but with an extra layer of gold film, (yellow) between the extracellular media and the glass (grey). The cells are grown on the gold, but there is a small gap (right hand blue region) in which the extracellular media is present.

The number density of electrons can be used to calculate the plasmon frequency of the gold using Equation (1.2) with  $\epsilon_\infty = 1.53$ .

$$\omega_p = \sqrt{\frac{ne^2}{m\epsilon_0\epsilon_\infty}} = 1.107 \times 10^{16} \text{ rad s}^{-1}. \quad (6.2)$$

In order to be compatible with the other data, this must be converted into a molar concentration.

$$c_{elec} = \frac{5.9 \times 10^{28}}{A_v} = 9.8 \times 10^{-4} \text{ mol m}^{-3}. \quad (6.3)$$

To calculate the diffusion coefficient it is necessary to first find the mobility and then use the Einstein relation relating mobility to the diffusion coefficient.

The electron mobility  $\mu$  is given by  $\mu = e\tau/m$  where  $\tau$  is the relaxation time and  $m$  is the electron mass.

$$\tau = \frac{m}{ne^2\rho_{el}} = 2.75 \times 10^{-14} \text{ s}. \quad (6.4)$$

Using  $\tau$  to calculate mobility gives  $\mu = 4.84 \times 10^{-3} \text{ m}^2 \text{ V}^{-1} \text{ s}^{-1}$ .

Using the Einstein relation gives

$$D_{elec} = \frac{\mu k_b T}{q} = 1.25 \times 10^{-4} \text{ m}^2 \text{ s}^{-1}. \quad (6.5)$$

This means that the diffusion coefficient for electrons is five orders of magnitude larger than for the other ionic species. Physically this is because of the small mass of the electrons. It also means that the electrons can respond very quickly to changes in the electric field.

The initial concentration profiles and diffusion coefficients are set up using tanh curves as in the case of the other models. These curves are set up so that the diffusion coefficient for the ions goes to zero at the gold surface. This prevents unphysical effects such as ions diffusing into the gold film or electrons diffusing out of the film and into the extracellular media.

Figure 6.2 shows the initial electron concentration confined to the region incorporating the gold film. Since the diffusion coefficient of the electrons outside the gold film is zero, there is no way for them to move into the solution. The transition to zero shown in Figure 6.2 is an example of the application of the tanh function being used to provide a continuous diffusion coefficient profile.

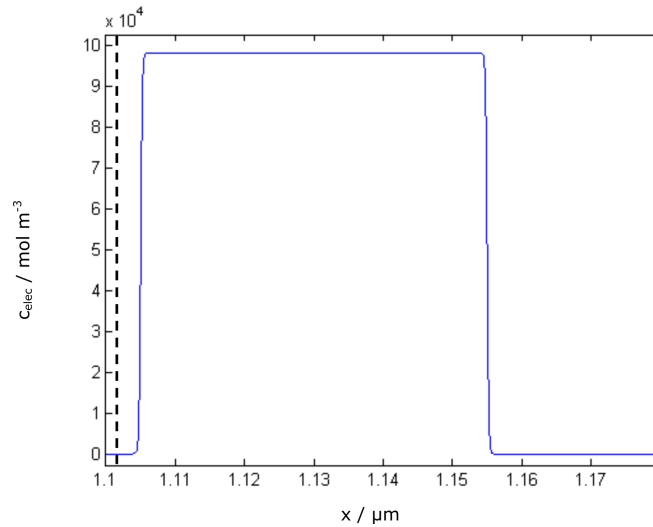


Figure 6.2: Initial concentration of the electrons plotted against spatial position. Conduction electrons are confined to the gold film layer in the model. The dashed line indicates the position of the boundary between the extracellular media and the gold film.

## 6.2 Results

The first results of the model are those which check whether the gold film affects the neuron function in any way. For gold to be a viable detector, it must not inhibit or alter in any significant way, the behaviour of the neurons. This means the full range of behaviours must be exhibited including, action potentials, resting potentials, refractory periods and sub threshold responses.

The other major area of interest with this model, is what happens within the gold film and at the interface between the extracellular media and the gold.

The resting and stimulated behaviour are observed as expected. Unstimulated, the system evolves from its initial electroneutral state to the equilibrium resting state. A spike is triggered due to the initial zero membrane potential being an unstable point in the Hodgkin Huxley model. Once at rest the system maintains a constant potential difference across the membrane. This can be seen in Figure 6.3. When a stimulation is applied, again by raising the diffusion coefficient for sodium within the membrane, an action potential occurs. This can be seen in Figure 6.4. This also gives good agreement with the single and double membrane cases shown in Figures

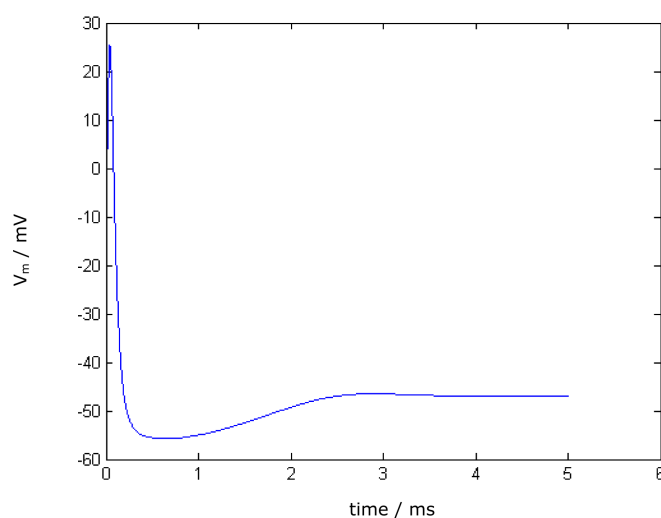


Figure 6.3: Plot of the membrane potential against time. When unstimulated, the nerve relaxes to a resting potential. Since the system is initialised in a globally electroneutral state, the potential difference across the membrane is initially zero. Since this zero potential difference is a non-equilibrium state within the Hodgkin Huxley model the system evolves through a spike (as if stimulated) before relaxing to rest, with a build up of charge on either side of the membrane.

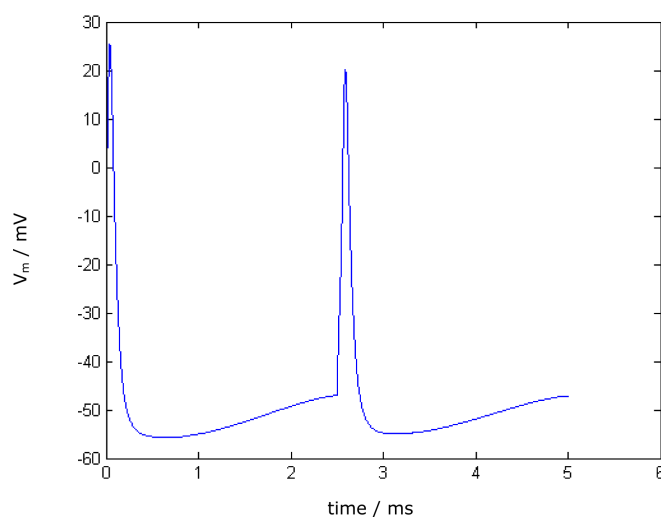


Figure 6.4: Plot of the membrane potential against time. A stimulus applied at  $t = 2.5$  ms causes an action potential to occur, as with the single and double membrane case. The presence of the gold layer does not prevent action potentials. For comparison with the single and double membrane cases consult Figures 4.8 and 5.6

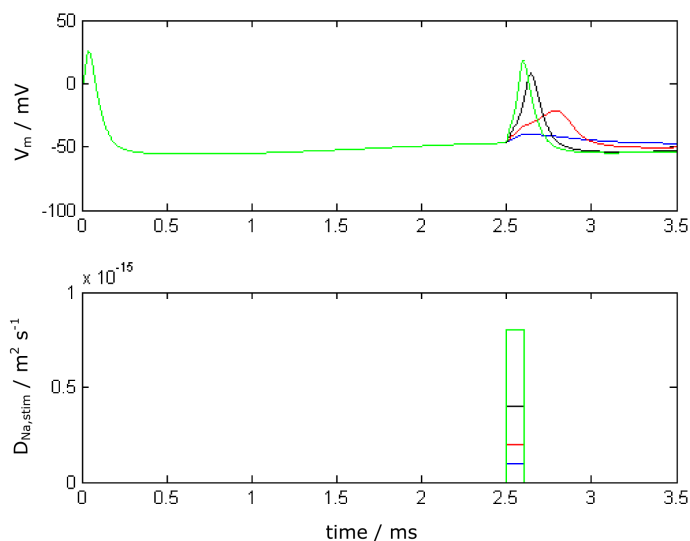


Figure 6.5: Top Panel: The effect of different magnitude stimuli on the membrane potential,  $V_m$ . Smaller stimuli are not sufficient to trigger an action potential, these are then referred to as subthreshold stimuli (blue and red curves). Larger stimuli do produce an action potential (black and green curves). Bottom Panel: Stimuli provided are shown. These take the form of an increase in the diffusion coefficient for sodium within the membrane.

4.8 and 5.6. By applying a range of stimuli, the transition from sub to suprathreshold can be observed. The two smaller stimuli represented by the blue and red curves in Figure 6.5 are not sufficient to cause an action potential and therefore exhibit a sub threshold response. The two larger stimuli, indicated by the black and green curves are capable of triggering an action potential.

It is again useful to look at the charge and electric field profiles close to the membrane. Figures 6.6a and 6.7a show that the behaviour of the charge density and electric field is similar to that in the double membrane situation, for comparison see Figures 5.11c and 5.9c. Charge density and Electric field undergo a rapid brief change during the action potential (at and around 2.5ms) and then return to resting values, this is shown by a colour change from red to blue at the time of the action potential in Figures 6.6a and 6.7a. This is as a result of the ion flow that occurs during an action potential, with the interior of the cell becoming more positively charged during the rising phase of the spike. Following the action potential a return

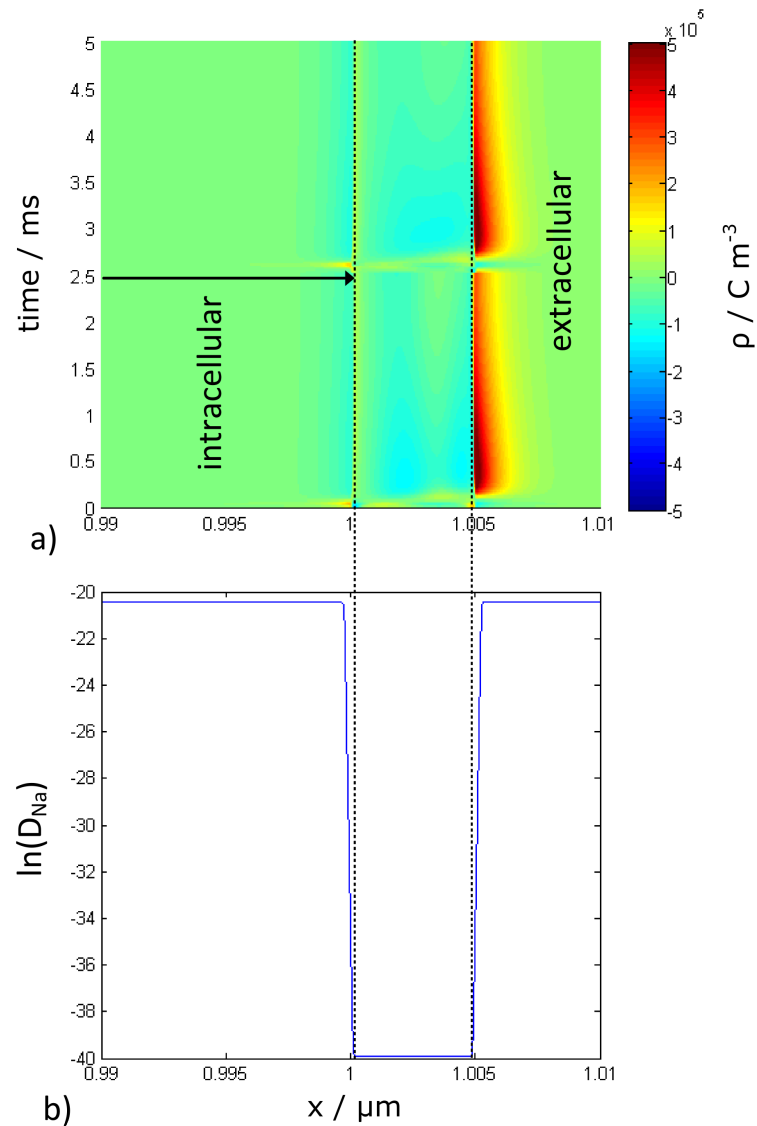


Figure 6.6: a) Charge density within the vicinity of the bottom membrane. The membrane walls are indicated by dashed lines. The application of the stimulus occurs after 2.5ms as indicated by the arrow. The charge build up swaps sign during the course of the action potential, shortly after the application of the stimulus. b) Logarithm of the diffusion coefficient for sodium plotted against  $x$ , shows the effective position of the membrane.

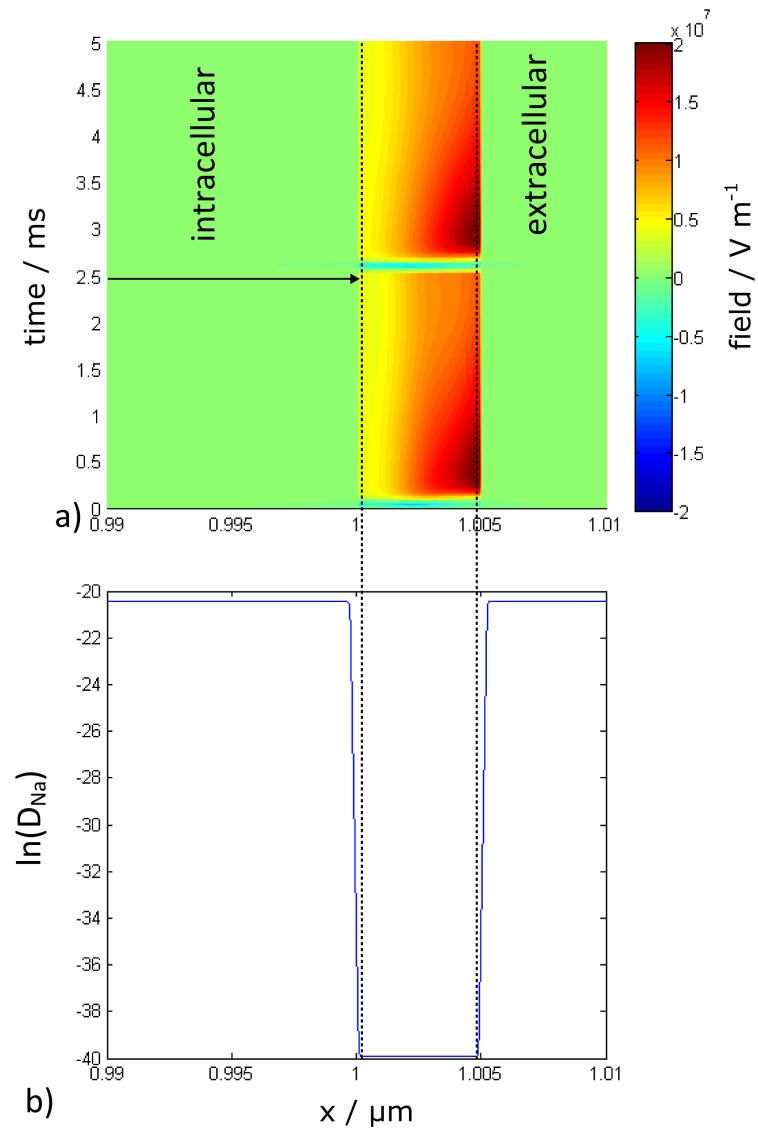


Figure 6.7: Electric field close to the bottom membrane. The membrane walls are indicated as dashed lines. The point of application of the stimulus is indicated by the arrow. The sign of the electric field is changed during the action potential as seen shortly after application of the stimulus. b) Logarithm of the diffusion coefficient for sodium plotted against  $x$ , shows the effective position of the membrane..

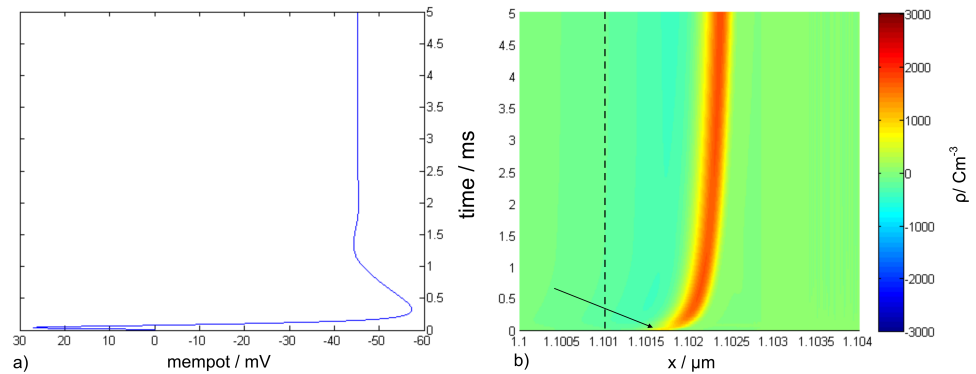


Figure 6.8: a) Potential profile showing initial spike and relaxation to rest. This is used to correlate with changes in charge density profile in b. b) Charge density near gold surface with no stimulation. There is some charge build up near the gold surface which occurs due to the firing of an initial spike before the resting state is reached. A yellow/orange band develops, showing the region of positive charge which is indicated by an arrow. The dashed line indicates gold surface boundary.

to a stable state is observed.

Of greater importance is whether there is any noticeable signature of action potentials at the gold / extracellular interface, as it is the gold layer that would be used in surface plasmon resonance experiments. For this reason it is of particular interest whether there is a charge build up and associated electric field at the gold surface. Figure 6.8b shows the charge density close to the gold surface when no stimulation is applied. The potential profile accompanying this is shown in Figure 6.8a. There is some small accumulation of approximately  $1000 \text{ Cm}^{-3}$  close to the gold surface, triggered by the initial stabilisation. (The system is initially in an unstable non-resting state). This accumulation is visible as band of yellow/orange within the colour plot. The charge accumulations are much lower than those found close to the membrane, as seen in Figure 6.6. The gap between the cell membrane and the gold surface is only 100 nm, so small amounts of charge could build up leading to larger charge densities outside the cell compared with in the semi infinite model. Figure 6.9b shows the effect of a stimulation on the charge build up at the gold surface. The stimulation applied at 2.5 ms triggers an action potential, as can be seen in Figure 6.9b. This can be seen to cause an increase in the magnitude of the charge buildup to approximately  $2000 \text{ Cm}^{-3}$ . An increase in the spatial extent is also observed

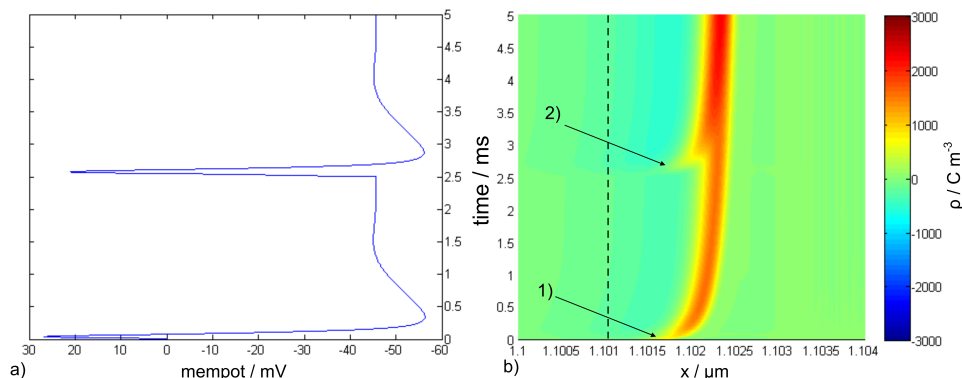


Figure 6.9: a) Potential profile showing an action potential caused by stimulation at 2.5 ms. This is used as a reference to correlate with changes in the charge density profile in b. b) Charge density near gold surface with a single stimulation applied at 2.5 ms. The action potential results in a second additional charge build up, following that triggered by the initial spike. Arrow 1 indicates the relaxation spike, arrow 2 shows the response to the stimulus. The thickness of the yellow/orange band increases after the initial relaxation spike and after the stimulation. The dashed line indicates gold surface boundary.

as an increase in the thickness of the yellow/orange bands and a transition to darker orange colours. Similar repeated charge build ups occur when a series of stimulations are applied. The application of multiple stimuli is shown in Figure 6.10a, with the clearly linked charge density profiles shown in Figure 6.10b.

The presence of a charge build up at the gold surface also gives rise to an electric field. When no stimulation is provided, a small field of approximately  $300 \text{ Vm}^{-1}$  builds up at the boundary due to the system returning to rest from an unstable state. This is indicated in Figure 6.11b as a yellow band in the colour plot, with corresponding membrane potential profiles shown in 6.11a. Action potentials triggered by the stimulations can be seen to cause an increase in the magnitude and extent of the field at the gold surface. The field response to a single stimulus is shown in Figure 6.12b, with the stimulus indicated in 6.12b whilst a series of three stimulations are shown in Figure 6.13b. Each successive stimulus causes an increase in the extent and strength of the field, indicated by a transition to oranges and reds and a general widening of the yellow bands.

It is worthwhile considering what effects the charge build up has on the

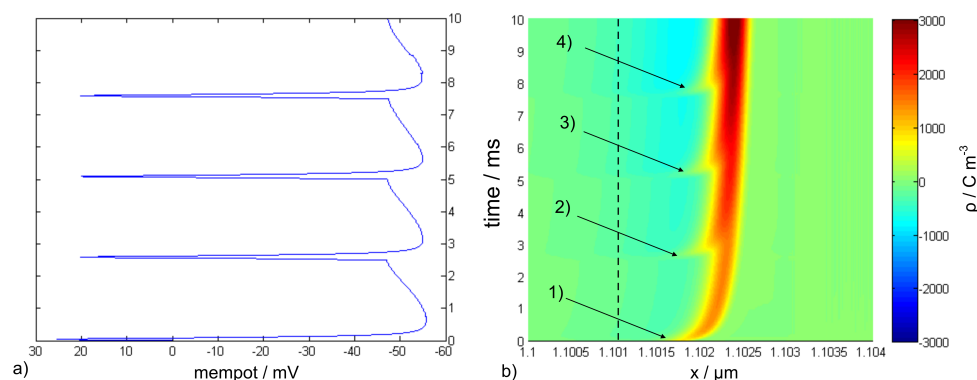


Figure 6.10: a) Potential profile showing three action potentials caused by stimulation at 2.5 ms, 5.0 ms and 7.5 ms. This is used as a reference to correlate with changes in the charge density profile in b. b) Charge density near gold surface with three stimulations at 2.5, 5.0 and 7.5ms. Each action potential increases the charge build up on the surface as indicated by the arrows. Arrow 1 indicates the position of the relaxation spike, whilst arrows 2, 3 and 4 show the responses to the stimuli. The overall magnitude of the charge buildup is still considerably smaller than that found on the membranes. With each successive stimulation the charge build up is seen as an increase in the thickness of the yellow/orange band and a transition towards darker orange. The dashed line indicates gold surface boundary.

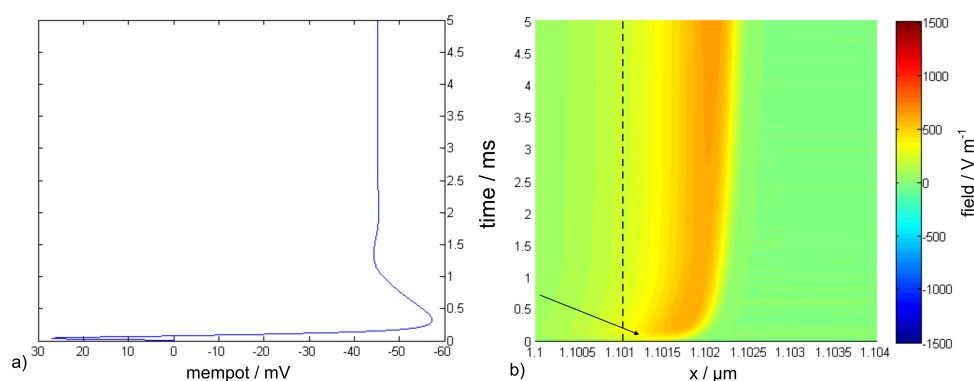


Figure 6.11: a) Potential profile showing initial spike and relaxation to rest. This is used to correlate with changes in the field profile in b. b) Field near gold surface with no stimulation. The electric field also shows signs of responding to changes occurring at the membrane. The initial relaxation spike triggers a non zero field at the gold surface, shown as a band of yellow in the colour plot.

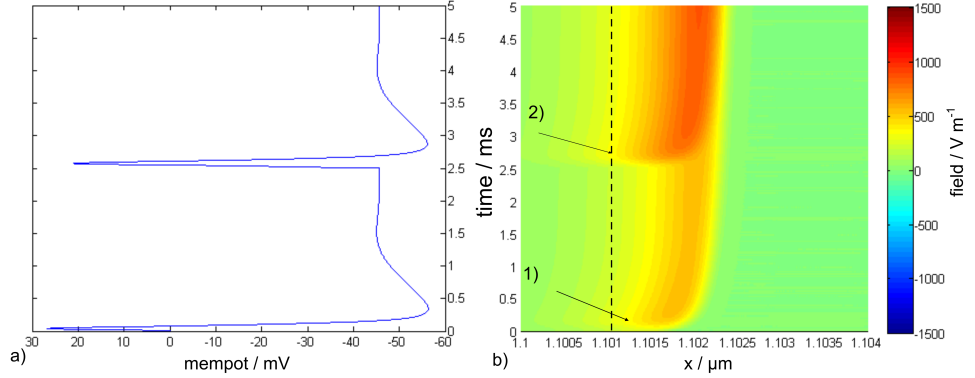


Figure 6.12: a) Potential profile showing an action potential caused by stimulation at 2.5 ms. This is used as a reference to correlate with changes in the field profile in b. b) Field near gold surface with single stimulation. The field magnitude and extent increases after an action potential caused by a stimulus applied at 2.5 ms. Arrow 1 indicates the relaxation spike, arrow 2 shows the response to the stimulus. Both the initial relaxation spike and the response to the stimulus result in an increase in the strength and spatial extent of the electric field. This is seen as a thick yellow/orange band in the colour plot.

plasmon frequency. If it is assumed that the charge density represents a change in the local number density of electrons, then Equation (6.2) can be used to calculate the new plasmon frequency.

From Figure 6.10 it can be seen that the maximum charge density is of the order  $\Delta\rho \approx 3000 \text{ Cm}^{-3}$ , this corresponds to a change in the electron number density,  $\Delta n$  of

$$\Delta n = \frac{\Delta\rho}{e} \approx 2 \times 10^{22} \text{ m}^{-3}. \quad (6.6)$$

This is only a  $10^{-6}$  fractional change in the number density of electrons.

Substituting  $n - \Delta n$  into Equation (6.2) and using the original value of the gold plasmon frequency, we see a small change in the plasmon frequency  $\Delta\omega_p \approx 2 \times 10^{-9} \text{ rad s}^{-1}$ . This is unlikely to be easily detectable, however future work could consider modelling whether there are any significant changes of refractive index within the gold, as this is a commonly used parameter in surface plasmon resonance experiments.

Running the unstimulated scenario to 10 ms allows the longer term resting behaviour at the gold boundary to be analysed. It seems that without

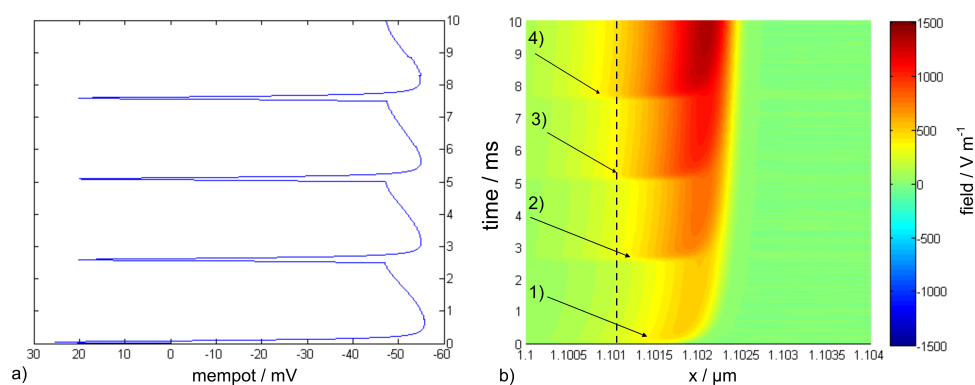


Figure 6.13: a) Potential profile showing three action potentials caused by stimulation at 2.5 ms, 5.0 ms and 7.5 ms. This is used as a reference to correlate with changes in the field profile in b. b) Field near gold surface with three stimulations. The extent and magnitude of the field increases with each action potential after stimuli applied at 2.5, 5.0 and 7.5 ms. Arrow 1 indicates the position of the relaxation spike, whilst arrows 2, 3 and 4 show the responses to the stimuli. Each successive stimulus causes the strength and the spatial extent of the field to increase. This is seen as a widening of the yellow/orange bands and also some areas of red appearing on the colour plot.

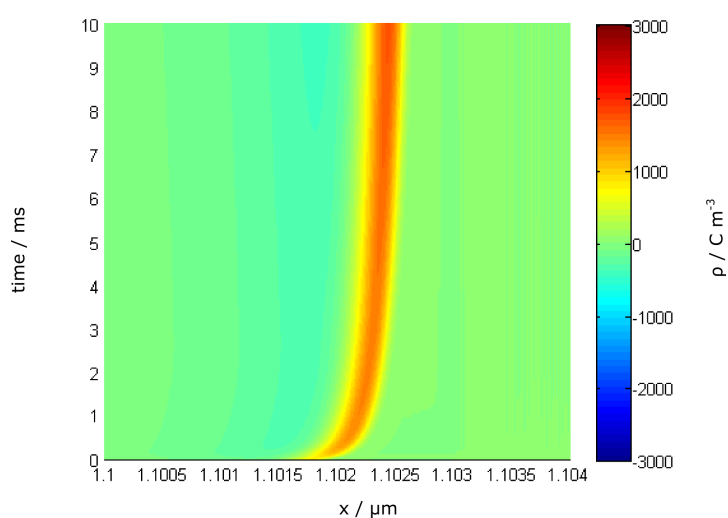


Figure 6.14: Charge density near gold surface with no stimulation. Run to 10ms we see there is no change compared with the 5ms scenario.

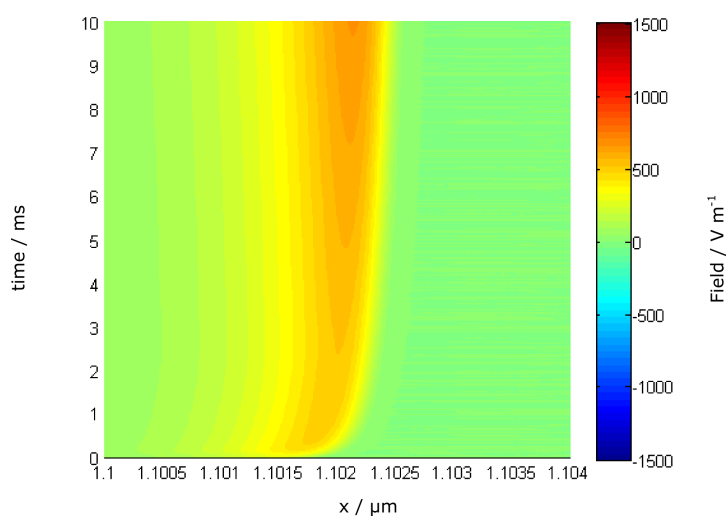


Figure 6.15: Field near gold surface with no stimulation. Run to 10ms we see there is no change compared with the 5ms scenario.

further stimulation there is still some level of charge build up. This could be due to the continued low level flux of ions through the membrane and is noticeably less than in the stimulated cases.

This model enables us to determine the field build up associated with action potentials at the gold surface. As a result of this, the model should enable further work to be carried out to model whether any surface plasmon resonance response should be expected in experimental work. This would entail adding plasmon physics to the Drift Diffusion enhanced Hodgkin Huxley model.

# Chapter 7

## Conclusions

The Hodgkin Huxley model can be combined with a set of drift diffusion equations to produce a series of models enabling a neuron to be simulated. Adding the drift diffusion equations to the model is useful as it allows the movement of ions through the ion channels within the Hodgkin Huxley model to be modelled as diffusion. The state of the ion channels, open or closed is linked to the diffusion coefficient within the membrane.

It is also a useful addition to the Hodgkin Huxley model, in that it enables the concentrations of ions to be modelled both intracellularly and extracellularly. This then allows fields and charge buildups to be calculated. The layered nature of the models should enable new users to add layers in to the model in order to simulate various experimental designs and parameters.

The first and most simple of these (outlined in Chapter 4) is the single membrane model. This simulates two semi infinite regions, one of intracellular space, the other of extracellular space. These two regions have different ionic concentrations to approximate those found in real situations. Some ions which are normally present in small amounts have not been included so as to simplify the model where possible. It would be relatively straightforward to add other ion species, but each species added would increase the number of equations to be solved, thereby increasing computation time. The two regions are separated by a thin membrane.

The behaviour of the intra and extracellular regions is governed by the drift diffusion and Poisson equations. The drift diffusion equations describe the motion of the ionic species in the presence of an electric field. These are coupled to the Poisson equation which calculates the potential from a given charge distribution.

---

In order to solve these equations they are discretised using a non uniform grid to allow a high density of points at the membrane, which is where most of the detail is required. This prevents there being too many grid points in the simulation for it to run within a reasonable time. Once discretised the iterative Newton Raphson method was used to solve the matrix equations within MATLAB.

The behaviour of the membrane is modelled partially using the drift diffusion and Poisson equations, but also incorporates the Hodgkin Huxley model. This simulates the opening and closing of ion channels, which regulate the flow of ions across the membrane.

This is done within the drift diffusion framework by adopting a greatly lowered diffusion coefficient within the membrane. Although this doesn't account for the microscopic level behaviour of individual ion channels opening and closing, it is a good approximation for the probabilistic opening of the gates as described by the gating variables in the Hodgkin Huxley model. The membrane diffusion coefficient then changes according to these gating variables defined within Hodgkin Huxley model. As ion channels open, the diffusion coefficient becomes larger, to represent the easing of restrictions on the flow. During each time step the potential difference across the membrane is calculated.

The system, when unstimulated, steadily evolves to a resting state known as the resting potential. This is important as it is one of the key features of neurons, which indicates that the model is valid. This is further shown by the response to the stimulations. If a stimulus is not of sufficient size, there will be a small move away from the resting potential which is gradually restored. This is the sub threshold behaviour.

Given a sufficient stimulus, a positive feedback effect occurs which triggers the opening of ion channels. This results in a sudden sharp rise in the potential difference across the membrane known as an action potential. This is a threshold based effect in that there is a significant change in behaviour once the threshold is reached, but further increases in the stimulus result in only small changes in output (slightly quicker onset of the action potential). The changes in the electric field and charge density close to the membrane were also considered and shown to be in line with what should be expected.

---

Although it is reassuring that the model behaves well and as expected, a semi infinite single membrane model does not represent a realistic physical situation. For this reason a more complex model was created which models a 1D slice through a cell.

This model also includes a region to represent the glass substrate upon which cells are often grown. This allows the model to be tested within the framework of a restricted extracellular space. As was the case with the single membrane model, the expected neuron behaviours were observed. Resting potentials, sub threshold responses and action potentials are all possible within the model and triggered in the same ways.

The field and charge build ups were also checked on both the membrane layers involved in the model. Again the behaviour expected was observed, with charge accumulations on either side of the membranes and significant electric fields within the membrane layers. As expected from the Hodgkin huxley model, these charge accumulations and fields change signs during an action potential.

The third model was a development of the double membrane model and includes a layer to simulate a gold film on the surface of the glass substrate. This is because cells can and have been grown on a gold surface, it also demonstrates the ability to introduce different substrate layers within the model.

The addition of the gold film adds some complications to the model as there is then another species (the conduction electrons) to include in the drift diffusion equations. This means the gold model requires more computational time as the number of elements in the matrices is larger.

The behaviour of the neuron was not affected by the presence of the gold layer and the usual behaviours (resting potentials, action potentials and sub threshold responses) were observed. However there were indications of a field and charge build up at the surface of the gold after action potentials. Repeat stimulations resulted in an increase in the extent and magnitude of the charge build up observed but it should be noted that the magnitudes involved are much smaller than the effects at the membrane.

The fractional change in the plasmon frequency,  $\omega_p$ , is of the order  $10^{-7}$  which is unlikely to be detectable. However it may be possible to extend the model to look at changes in the refractive index of the gold film.

Another possible benefit to including a gold substrate layer is that it can in the future be extended to model some Surface Plasmon Resonance (or SPR) experiments. If the charge and field build ups affect the plasmon behaviour, then surface plasmon resonance experiments will be able to detect neural activity.

The numerical methods developed to solve the model allow for different layers to be put into the model and their properties to be matched using tanh curves. This enables smoothly changing concentration and diffusion coefficient profiles, avoiding the sharp gradient discontinuities that occur with a step change in parameters. The non-uniform grid used is a key feature of the model allowing points to be more closely spaced where there are large parameter changes, but eliminates the need for this close spacing to be extended to all points in the computational domain.. This is particularly important for the membrane regions and also transitions between different media, such as the gold or glass. By restricting the range over which the parameters change, no unphysical effects are introduced. This is very important for the interfaces between the media solutions and membrane layers, but even more so for the gold/media interface.

The key features of this work is that it is a working model that can be interfaced with other models that require knowledge of electric fields within the vicinity of a neuron. The model is demonstrated to reproduce the key features of neurons such as action potentials, resting potentials and subthreshold behaviour. This means that the model could be used to test the feasibility of novel detection methods.

## 7.1 Suggestions for further work

The models developed show a promising way forward in the search for a more effective detector of neural activity. One way to do this would be to enhance the gold layer model so that the effects of neural activity on Surface Plasmons in the gold film can be determined.

Changes in the surface plasmons behaviour can be detected as a change in the refractive index of the gold film. This would require the surface plasmon physics to be incorporated into the gold film, so that the response of the plasmons to the neural activity could be modelled[26]. Different types of gold nanoparticles can be considered for biosensing applications[57].

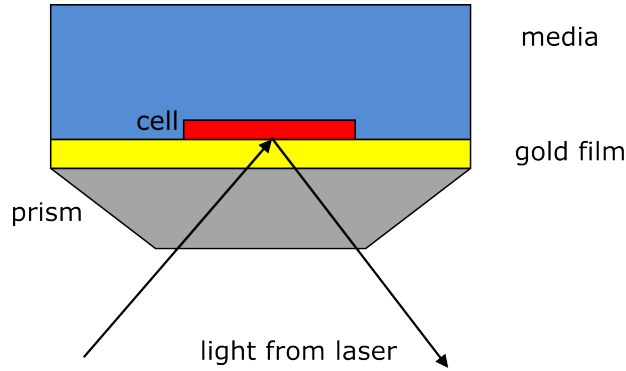


Figure 7.1: Schematic of the setup used for SPR experiments. Cells are grown on a gold film above a prism. The cells are immersed in media and the gold film is illuminated using a laser light source.

A schematic indicating the basics of the SPR experiment is shown in Figure 7.1. The cells are grown on a gold film on top of a prism. They are then immersed in the nutrient rich media and lasers are used to illuminate the gold film through the prism.

Since there was a clear field and charge build up at the gold boundary, it would be interesting to see the plasmon behavior modelled in more detail.

A second extension of the model would be to use the cable equation to allow the modelling of the propagation of pulses in 2D [41; 58; 59]. The cable equation is often used in neuron models that deal with propagating pulses and is defined as follows.

$$c_m \frac{\partial V_m}{\partial t} = -j_m + \frac{1}{2\pi a r_i} \frac{\partial^2 V_m}{\partial x^2} \quad (7.1)$$

where  $r_i$  is the resistance per unit length inside the axon,  $j_m$  is the current density,  $c_m$  is the membrane capacitance per unit area and  $a$  is the axon radius.

Incorporating this into the scheme adopted in this work would require solving the drift diffusion equations in 2D. This is a much more difficult computational problem and so a great deal more computing power would likely be required. This would also enable the concentration changes outside the cell to be calculated in 2D allowing a realistic picture of the current flows associated with the action potentials. A 2D model of the current flows would be sufficient as most of the time cells are grown on a flat surface and so form networks similar to interconnected wires. A 2D model would be sufficient to

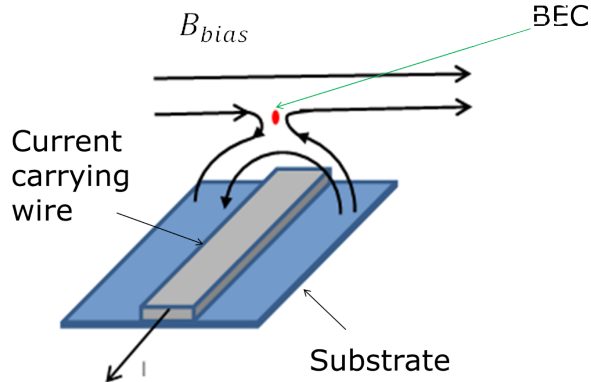


Figure 7.2: A BEC in a magnetic trap ready to image a current source. The condensate forms in the minimum of the trap. Changes in the magnetic field disturb the density profile of the cloud. This can be imaged using optical methods and used to build up a picture of the current source.

deal with those, though of course it would eventually be desirable to extend this to 3D to model more complex neural structures.

From this, a simple application of the Biot-Savart law would enable the calculation of the magnetic fields from the current data. Of particular interest then would be the changes in the magnetic field profiles during an action potential.

If there was to be a sufficiently strong shift in the magnetic field, then one of a range of magnetic field sensors could be used.

An example of a magnetic field sensor with high spatial and temporal resolution is the Bose Einstein Condensate microscope [21]. This is a relatively recent technology which has been used to measure the current flow in wires or thin films. It involves using a cloud of cold atoms in the Bose condensed state positioned in a magnetic trap above the current source. The trap setup is shown in Figure 7.2 and is often referred to as an atom chip. These use a homogeneous bias field and a current carrying wire to trap the atom cloud in a potential minima. For a bias field,  $B_{bias}$  and a wire current  $I$  the total magnetic field is given as follows

$$\mathbf{B} = \begin{pmatrix} B_{bias} \\ 0 \\ 0 \end{pmatrix} + \frac{I\mu_0}{2\pi(x^2 + y^2)} \begin{pmatrix} -y \\ x \\ 0 \end{pmatrix} \quad (7.2)$$

The trap forms in the minimum of this field. The x and y coordinates of

this position are as follows

$$x_{trap} = 0 \quad (7.3)$$

$$y_{trap} = \frac{I\mu_0}{2\pi B_{bias}} \quad (7.4)$$

The position of the trap can therefore be changed by adjusting the current in the wire and the bias field. Variations in the magnetic field, such as those caused by the currents associated with an action potential result in a change of the density profile of the cold atom cloud. The structure of the condensate can be imaged with a camera using optical absorption methods. By scanning the position of the BEC it is possible to build up a detailed picture of the currents.

One thing that makes the BEC microscope an interesting proposition for imaging biological systems is the combination of high sensitivity of approximately 100 pT and good spatial resolution  $\mu\text{m}$ .

Whilst these are not the best values which can be achieved, SQUIDs have a higher sensitivity and magnetic force microscopy has a better resolution, they are nevertheless a useful compromise between the two.

The technique has been used to image the current flows within copper wire and thin metal films [60].

A very rough estimate of the magnetic field,  $B_{neuron}$  can be obtained from the current density within the Hodgkin Huxley model. From Figure 2.7, we can infer a current density,  $j \approx 5 \text{ Am}^{-2}$ . For larger mammalian axons with radius,  $r = 10\mu\text{m}$  the Biot Savart law gives

$$B_{neuron} = \frac{\mu_0 j \pi r^2}{2\pi R} \approx 300 \text{ pT} \quad (7.5)$$

where  $R = 1\mu\text{m}$  is the distance from the condensate to the cell. Since this is larger than the 100 pT sensitivity of the BEC there should be a good possibility of detecting neural activity. It would of course be beneficial to model the full 2D pulse propagation to get a better picture of the magnetic fields involved.

Unfortunately, there are also some practical considerations to overcome when considering the use of BECs with living cells. Principally that Bose Einstein condensates can only be formed in an ultra high vacuum. This is unfortunately not a suitable environment for the survival of cells. It could be possible to build a chamber which can withstand the forces of the ultra high vacuum and have the cells on one side and the BEC on the other.

This would need a very thin window, of approximately one micron, in order for the BEC to still be close enough to detect any magnetic field changes. Having a thin window would require a very careful choice of materials as the forces due to the change in pressure would be very large.

Other potential magnetic field sensors include SQUIDs and diamond N-V centres. These are novel quantum devices which provide high resolution magnetic field sensing.

SQUIDs are extremely sensitive magnetometers which have found a variety of uses, some of which are biological. An array of SQUIDs can be used in magnetoencephalography to detect neural activity in the brain. Diamond N-V centres are formed when a nitrogen atom and vacancy substitutes for a carbon atom in the diamond structure. This is an optical defect which fluoresces under illumination. This fluorescence can be used to determine the magnetic sub level and so each unit acts as a magnetometer [22; 61; 62]. Another benefit of diamond N-V centres is that neurons can be grown on diamond.

If a new detector is developed it could also be tested against artificial neurons made using p-n nanowires, which behave in a more controlled way than real neurons, but display similar types of behaviours [63; 64].

The suggestions for further work discussed in this section are all areas where it is believed that this model could be used to shed some light on the viability and uses of more novel detection systems. This could be achieved by combining this work with other models of the systems involved, such as the Projected Gross-Pitaevskii Equation (PGPE) code used to model the responses of Bose Einstein Condensates to magnetic fields [65].

If a working 2D cable equation type model could be developed from this it would be possible to move towards modelling neural networks, although this is a much more demanding problem.

# References

- [1] edited by E. R. Kandel. *Principles of neural science*. McGraw Hill Medical, New York, 2013.
- [2] P. Nelson and M. Radosavljevic. *Biological physics: energy, information, life*. W. H. Freeman, New York, 2008.
- [3] D. J. Aidley. *The physiology of excitable cells*. Cambridge, Cambridge, 1998.
- [4] N. Herzog, M. Shien-Idelson, and Y. Hanein. Optical validation of in vitro extra-cellular neuronal recordings. *J. Neural Eng.*, 8:056008, 2011.
- [5] P. Dayan and L. F. Abbott. *Theoretical neuroscience: computational and mathematical modelling of neural systems*. MIT Press, Cambridge, Mass, 2001.
- [6] F. C. Hoppensteadt and C. S. Peskin. *Modelling and simulation in medicine and the life sciences*. Springer, New York, 2010.
- [7] N. T. Carnevale. *The NEURON book*. Cambridge University Press, Cambridge, 2005.
- [8] M. C. Avery, N. Dutt, and J. L. Krichmar. A large-scale neural network model of the influence of neuromodulatory levels on working memory and behaviour. *Frontiers in computational neuroscience.*, 7:133, 2013.
- [9] E. Neher and B. Sakmann. Single-channel currents recorded from membrane of denervated frog muscle fibres. *Nature*, 260:799–802, 1976.
- [10] B. Sakmann and E. Neher. Patch clamp techniques for studying ionic channels in excitable membranes. *Ann. Rev. Physiol.*, 46:455–472, 1984.

- 
- [11] M. E. Spira. Multi-electrode array technologies for neuroscience and cardiology. *Nature Nanotechnology*, 8:83–94, 2013.
- [12] D. Braken et al. Open-cell recording of action potentials using active electrode arrays. *Lab Chip*, 12:4397–4402, 2012.
- [13] R. Stepnoski et al. Noninvasive detection of changes in membrane potential in cultured neurons by light scattering. *Proc. Natl. Acad. Sci. USA*, 88:9382–9386, 1991.
- [14] S. Chemla and F. Chavane. Voltage-sensitive dye imaging: Technique review and models. *Journal of Physiology - Paris*, 104(1-2):40–50, 2010.
- [15] C. Grienberger and A. Konnerth. Imaging calcium in neurons. *Neuron*, 73(5):862–885, 2012.
- [16] T. Nagai et al. Expanded dynamic range of fluorescent indicators for  $ca^{(2+)}$  circularly permuted yellow fluorescent proteins. *Proc. Natl. Acad. Sci. USA*, 101:10554–10559, 2004.
- [17] E. A. Jares-Erijmann and T. M. Jovin. FRET imaging. *Nat. Biotechnol.*, 21:1387–1395, 2003.
- [18] J. W. Wang. Two-photon calcium imaging reveals an odor-evoked map of activity in the fly brain. *Cell*, 112:271–282, 2003.
- [19] J. Nakai, M. Ohkura, and K. Imoto. A high signal to noise  $ca^{(2+)}$  probe composed of a single green fluorescent protein. *Nat. Biotechnol.*, 19:137–141, 2001.
- [20] T. Dittgen et al. Lentivirus-based genetic manipulations of cortical neurons and their optical and electrophysiological monitoring in vivo. *Proc. Natl. Acad. Sci. USA*, 101:18206–18211, 2004.
- [21] S. Wildermuth. Microscopic magnetic field imaging. *Nature*, 435:440, 2005.
- [22] L. T. Hall. Monitoring ion-channel function in real time through quantum decoherence. *PNAS*, 107(44):18777–18782, 2010.
- [23] K. F. Giebel et al. Imaging of cell/substrate contacts of living cells with surface plasmon resonance microscopy. *Biophysical Journal*, 76:509–516, 1999.

- 
- [24] S. A. Kim et al. In vivo optical neural recording using fiber-based surface plasmon resonance. *Optics Letters*, 37:614–616, 2012.
- [25] E. Kretschmann and H. Raether. Radiative decay of non radiative surface plasmons excited by light. *Zeitschrift fur Naturforschung A*, 23:2135–2136, 1968.
- [26] S. A. Maier. *Plasmonics: Fundamentals and Applications*. Springer, Berlin, 2007.
- [27] P. Johnson and R. Christy. Optical constants of the noble metals. *Physical Review B*, 6(12):4370–4379, 1972.
- [28] P. Drude. Zur lektionentheorie der metalle. *Annalen der Physik*, 306(3):566–613, 1900.
- [29] E. C. Le Ru and P. G. Etchegoin. *Principles of Surface-Enhanced Raman Spectroscopy*. Elsevier, Amsterdam, 2009.
- [30] S. A. Kim et al. Optical measurement of neural activity using surface plasmon resonance. *Optics Letters*, 33 (9):914 – 916, 2006.
- [31] H. Baac et al. Extracellular optical recording configuration for neuronal action potential detection by using surface plasmon resonance: preliminary experiment. *Proceedings of the 2nd international IEEE EMBS conference on neural engineering.*, pages 332–335, 2005.
- [32] M. H. Henderson et al. Observation of bose-einstein condensation in a dilute atomic vapour. *Science*, 269:198–201, 1995.
- [33] K. B. Davis et al. Bose-einstein condensation in a gas of sodium atoms. *Physical Review Letters*, 75(22):3969–3974, 2011.
- [34] S. Wildermuth et al. Sensing electric and magnetic fields with bose-einstein condensates. *Appl. Phys. Lett.*, 88:264103, 2006.
- [35] A. L. Hodgkin and A. F. Huxley. A quantitative description of membrane current and its application to conduction and excitation in nerve. *J. Physiol.*, 117:500–544, 1952.
- [36] A. L. Hodgkin, A. F. Huxley, and B. Katz. The effect of temperature on the electrical activity of the giant axon of the squid. *J. Physiol.*, 109:240–249, 1949.

- 
- [37] A. L. Hodgkin and A. F. Huxley. Currents carried by sodium and potassium ions through the membrane of the giant axon of *Loligo*. *J. Physiol.*, 116:449–472, 1952.
- [38] A. L. Hodgkin and A. F. Huxley. The components of membrane conductance in the giant axon of *Loligo*. *J. Physiol.*, 116:473–496, 1952.
- [39] A. L. Hodgkin and A. F. Huxley. The dual effect of membrane potential on sodium conductance in the giant axon of *Loligo*. *J. Physiol.*, 116:497–506, 1952.
- [40] W. A. Catterall et al. The hodgkin-huxley heritage: From channels to circuits. *Journal of Neuroscience.*, 32:14064–14073, 2012.
- [41] R. K. Hobbie and B. J. Roth. *Intermediate Physics for Medicine and Biology*. Springer, Heidelberg, 2007.
- [42] B. P. Bean. The action potential in mammalian central neurons. *Nature Reviews Neuroscience*, 8:451–465, 2007.
- [43] W. Gerstner and W. Kistler. *Spiking Neuron Models: Single Neurons, Populations, Plasticity*. Cambridge University Press, Cambridge, 2002.
- [44] R. FitzHugh. Impulses and physiological states in theoretical models of nerve membrane. *Biophys. Journal*, 1(6):445–466, 1961.
- [45] H. Bruus. *Theoretical Microfluidics*. Oxford, Oxford, 2007.
- [46] G. L. Pollack and D. R. Stump. *Electromagnetism*. Addison Wesley, San Francisco, 2002.
- [47] R. L. Burden, J. D. Faires, and A. M. Burden. *Numerical Methods*. Cengage Learning, Boston, Mass, 2011.
- [48] W. F. Ames. *Numerical Methods for partial differential equations*. Academic Press, London, 1992.
- [49] K. F. Riley, M. P. Hobson, and S. J. Bence. *Mathematical Methods for Physics and Engineering*. Cambridge University Press, Cambridge, 2006.
- [50] W. H. Press et al. *Numerical Recipes in C++: The art of Scientific Computing 2nd Edition*. Cambridge University Press, Cambridge, 2002.

- 
- [51] P. J. Oliver. *Introduction to Partial Differential Equations*. Springer, New York, 2014.
- [52] K. R. Ward, E. J. F. Dickinson, and R. G. Compton. Dynamic theory of membrane potentials. *J. Phys. Chem. B*, 114:10763–10773, 2010.
- [53] K. R. Ward, E. J. F. Dickinson, and R. G. Compton. How far do membrane potentials extend in space beyond the membrane itself? *Int. J. Electrochem. Sci.*, 5:1527–1534, 2010.
- [54] T. Sokalski, P. Lingenfelter, and A. Lewenstam. Numerical solution of the coupled nernst-planck and poisson equations for liquid junction and ion selective membrane potentials. *J. Phys. Chem. B*, 107:2443–2452, 2003.
- [55] D. R. Lynch. *Numerical Partial Differential Equations for Environmental Scientists and Engineers: A First Practical Course*. Springer US, Heidelberg, 2005.
- [56] S. M. Sze and K. K. Ng. *Physics of Semiconductor Devices 3rd edition*. Wiley, Hobokon, 2007.
- [57] S. Zeng et al. A review on functionalized gold nanoparticles for biosensing applications. *Plasmonics*, 6:491–506, 2011.
- [58] H. C. Tuckwell. *Introduction to theoretical neurobiology*. Cambridge, Cambridge, 1988.
- [59] R. M. Gulrajani. *Bioelectricity and biomagnetism*. Wiley, New York, 1998.
- [60] S. Eiger et al. Long-range order in electronic transport through disordered metal films. *Science*, 319:1226, 2008.
- [61] L. T. Hall et al. High spatial and temporal resolution wide-field imaging of neuron activity using quantum nv-diamond. *Scientific Reports*, 2:401, 2012.
- [62] C. L. Degen. Scanning magnetic field microscope with a diamond single-spin sensor. *Applied Physics Letters*, 92:243111, 2008.

- [63] A. Samardak et al. An analogue sum and threshold neuron based on the quantum tunnelling amplification of electrical impulses. *New Journal of Physics*, 10:083010, 2008.
- [64] A. Nogaret. Artificial ion channels and spike computation in modulation-doped semiconductors. *Europhys. Lett.*, 68 (6):874–880, 2004.
- [65] N. Welch. *Non-equilibrium dynamics of Bose-Einstein condensates*. PhD Thesis, University of Nottingham, 2015.